Atomistic study of structural and electronic transport properties of silicon quantum dots for optoelectronic applications

Núria García Castelló

FACULTAT DE FÍSICA
Departament d'Electrònica

MEMÒRIA DE TESI DOCTORAL PRESENTADA PER OPTAR AL
TÍTOL DE DOCTORA EN NANOCIÈNCIES
PER LA UNIVERSITAT DE BARCELONA

Atomistic study of structural and electronic transport properties of silicon quantum dots for optoelectronic applications

Núria García Castelló

Directors: Dr. Albert Cirera Hernández
Dr. Juan Daniel Prades García

Tutor: Dr. Albert Cirera Hernández

Barcelona, Març de 2014

Programa de Doctorat en Nanociències

Atomistic study of structural and electronic transport properties of silicon quantum dots for optoelectronic applications

Tesi que presenta Núria García Castelló

per optar al títol de Doctora per la Universitat de Barcelona

Directors de Tesi:
Dr. Albert Cirera Hernández Dr. Juan Daniel Prades García

Departament d'Electrònica
Grup de Micro-Nanotecnologies i Nanoscòpies per Dispositius Electrònics i Fotònics (MIND)
Institut de Nanociència i Nanotecnologia (IN^{2}UB)

Acknowledgement

I would like to acknowledge my supervisors, Albert and Dani, for their patience and guidance,

Sergio and Roberto for the important work that they have done,

Stefano and the Modena group, specially Feffe and Ivan, for their hospitality,

the colleagues of the office and mindundis (Giovanni, Oriol, Luis, Xavi, Bea, Jordi, Aïda, Olga, Sergi, Elena, Llorenç, Radouane, Roman, Julià, Oriol, Alberto, JM and JM, Yonder, els Lluisos) for the coffee breaks and Friday out-lunch time and evening games (and beers and wine and ... well ... other drinks hidden in *that place*),

my group of theorists (Blai and Blai, Adriana, Ivan, Marina, Carmen, Genís, Miquel, Markus, Renau, Luis, Dani, Axel, Blanca, and also Gerard and Louis) for lunch time, and coffee time, and piti time, and *whatever* time,

my friends in Modena (Miquel and Oliver and the others of the *hispanic* community in the faculty, Dáire and Erik and the other Ferrari guys, Sara and the Couchsurfing family) for all the good times together and specially for their capacity to do something any time I was bored,

my friends of all times (Carla, Joan, Arnau, Lau, Pau, Uri, Adrià, Nesi, Eli, Marina, Jaume, Clara, Irene, Jordi, Mercè, Uri) for the weekly bar time,

and my family for their unconditional support.

And a special thanks to my life comrade during these years, Màxim. Also to jazz music and my friends, Juanan and Lucas, that tried to play with me when my head was thinking in all this stuff.

This work would have not been possible without the financial support of the FPU program of the Spanish Government.

Contents

1 Preface **1**
1.1 Transport in nanoelectronics . . . 3
1.2 Brief overview . . . 6
1.3 Aim of this PhD Thesis . . . 9
1.4 Outline . . . 9

2 Theoretical framework **13**
2.1 Density Functional Theory . . . 13
2.1.1 Some words about Hartree-Fock, correlation and exchange . . . 14
2.1.2 About Density Functional Theory . . . 16
2.1.3 Approximations in present DFT computations and notes about the code . . . 22
2.2 Non-Equilibrium Green Functions Formalism . . . 27
2.2.1 Description of nanodevices inside NEGFF . . . 27
2.2.2 Expressions used in TranSIESTA code . . . 29
2.2.3 Exemple of the use of NEGFF in a transport calculation 34
2.3 Transfer Hamiltonian formalism . . . 36
2.3.1 Transfer Hamiltonian formalism: transport in quantum devices . . . 36
2.3.2 WKB approximation: expressions for transmission coefficients . . . 38
2.3.3 Brief overview about SIMQdot, the code used in transport calculations . . . 39

3 Transport of bulk Si in the main crystallographic growth directions of Si nanowires **43**
3.1 Computational details . . . 46
3.2 Thermodynamic model for the stability of polymorphs in Si NWs . . . 47
3.3 Electronic transport in bulk Si . . . 53
3.3.1 Atomistic models of the main growth directions of Si NWs . . . 53
3.3.2 Si bulk transport properties . . . 55
3.3.3 Transport properties of a planar defect . . . 59

3.4 Conclusions . . . 61
3.4.1 Thermodynamic model for the stability of polymorphs in Si NWs . . . 62
3.4.2 Electronic transport in bulk Si . . . 62
3.4.3 DFT-NEGFF methodology to study transport in nanostructures . . . 63

4 Silicon quantum dots embedded in a SiO_2 matrix 65
4.1 Computational details . . . 66
4.2 Description of the systems . . . 67
4.3 Electronic structure . . . 68
4.3.1 Band offset . . . 73
4.3.2 Correction of the barriers values . . . 74
4.3.3 An empiric expression for the band edges of Si QD in SiO_2 crystalline matrix . . . 75
4.4 Electronic transport . . . 79
4.4.1 *I-V* characteristics . . . 79
4.4.2 Dependence with size and amorphization level . . . 80
4.5 Conclusions . . . 82
4.5.1 Electronic transport through a single Si QD . . . 82
4.5.2 DFT-TH methodology to study transport in nanostructures . . . 84

5 Doped silicon quantum dots embedded in a SiO_2 matrix 87
5.1 Computational details . . . 87
5.1.1 On the complexity of the systems . . . 88
5.2 Description of the systems . . . 88
5.2.1 Morphological features . . . 89
5.2.2 Formation energy . . . 91
5.3 Electrical structure . . . 94
5.4 Electrical transport . . . 97
5.5 Other doping atoms . . . 102
5.6 Conclusion . . . 103

6 Summary and Conclusions 105
6.1 Conclusions . . . 105
6.1.1 On the framework and methods . . . 105
6.1.2 On the QD size . . . 107

6.1.3 On the effects of doping . . . 107
6.2 Future work . . . 108

A Mulliken population of doped Si QDs **111**

B Scientific Curriculum **117**
B.1 Academic Degrees . . . 117
B.2 Publications . . . 118
B.3 Contributions in Conferences . . . 119
B.4 Participation in Projects . . . 120
B.5 Experience with Scientific Equipments and Techniques . . . 121
B.6 Specialization courses . . . 121

C Resum en català **123**
C.1 Introducció . . . 123
C.1.1 Transport en nanoelectrònica . . . 125
C.1.2 Treballs previs sobre punts quàntics de Si intrínsecs, el seu transport electrònic i el seu dopatge . . . 127
C.2 Objectius d'aquesta Tesi Doctoral . . . 128
C.3 Estructura de la Dissertació . . . 129
C.4 Resultats i conclusions . . . 130
C.4.1 Sobre la metodologia proposada . . . 130
C.4.2 Sobre la mida dels QDs . . . 131
C.4.3 Sobre l'efecte del dopatge . . . 131

Chapter 1

Preface

It is questionless that silicon has become the most used material in electronics [1, 2]. The qualities of silicon are well-known: from its abundance and economic value to the capacity to easily combine with oxides and become the essential material for electronic integrated circuits, in CMOS technology or other types of transistors. The capacity to scale-down their size is the basis of the success of current technology. A step further, though, is the idea of integrating electronic and photonics in a so-called "all-Si" technology [3]. However, new strategies are needed to overcome the two principal obstacles of a possible *bulk Si photonics*: the indirect band gap and the band gap amplitude, suitable for operation only in the infrared range. Thus, the indirect transitions between the conduction band minimum and the top of the valence band (and the complementary) in bulk Si is strongly suppressed due to the low probability of the phonon assistance interaction needed in order to satisfy the momentum conservation law.

The observation of visible-range emission in nanocrystallites and porous Si in the early 1990 [4–6] opened the field of study of this PhD Thesis, *silicon nanoscience*, in the form of nanostructures, such as nanowires, nanorods, nanoparticles or quantum dots (QDs) [7].

Due to the quantum confinement of the carriers inside the QD [8], the band gap of the material increases when QD size decreases (see the top panel of Fig. 1.1), giving values higher than bulk Si energy gap and making Si QDs good candidates for tunable-band gap devices. Moreover, due to the localization of electronic states within nanostructures, following the Heisenberg uncertainty principle, the momentum distribution is not restricted (silicon in the nanoscale becomes effectively a direct band gap material).

Based on these effects, several new applications have been reported in the last years, from light emission devices [9] to tandem solar cells [10] or other kind of opto-electronic devices [11].

This PhD Thesis has been developed in the framework of the European Project NASCEnT (silicon NAnodots for Solar CEll Tandem), which main objective was to create a tandem solar cell of silicon quantum dots (Si QDs) as a candidate for third generation of solar cells in order to overcome the Shockley-Queisser limit [12, 13], i.e. the maximum theoretical efficiency of optoelectronic devices, of current single solar cells.

Apart from the technological problems, such as junctions, contacts, ... the main source of limiting the efficiency of solar cells is that not all the energy range of solar spectra can be absorbed and converted into electricity. The most important power loss mechanisms in single band gap solar cells are related to the photons that have lower or higher energy than the band gap of the material, which are not absorbed or lose the difference between their energy and the band gap by heating the device, respectively. The last problem can be improved through a tandem solar cell of materials with different band gap, in order to minimize the loses by thermalization by having more than one band gap available to absorb energy. The theoretical efficiency limit increases from 29% for single pn junction to 42.5% for 2-cell tandem solar cells, with an optimized band gap of 1.7-1.8 eV for the top cell on a bottom cell of bulk Si [14].

Third generation solar cells concentrate the efforts to find a solution for the above losses with abundant materials not toxic and with approaches which permit scale mass production. Thus, the proposed device in NASCEnT project (see the bottom panel of Fig. 1.1 for a schematic view of the desirable device) was a tandem solar cell with bottom bulk Si layer with a top layer with a distribution of embedded Si QDs, in order to have a range of band gaps where excitons will be able to thermalize to. Moreover, the main advantages of Si QDs with respect to other candidates for tandem solar cells, such as III-V multijunction (toxic and cost-intensive) or a-Si/μ-Si dual junction cells (restricted to two junctions and show degradation effects), are: the possibility of two or more junctions, the non-toxicity and abundance of Si and silicon dielectric matrices (SiO_2, SiC, Si_xN_y), and the compatibility with current silicon technology.

In this context, this PhD Thesis aims to contribute to a better understanding of the electron transport properties in Si QDs of different sizes and different doping conditions, embedded in dielectric matrices.

1.1 Transport in nanoelectronics

From 1985 to the present, the size of electronic devices has decreased several orders of magnitude, from μm to nm scale, and the predominant kind of transport inside them has also changed. While in big channels the diffusive transport (random paths due to electron scattering) is the main kind of transport, in small channels only ballistic transport takes place [15].
In diffusive transport, the resistance R of a device is proportional to the resistivity ρ of the material and to the geometry of the device: $R = \rho\frac{L}{A}$, L being the length and A the area of the device. If we go deeper in the nanoscale, the length L goes to zero, and, then, R would go to zero, too. However, we can see that this does not happen in the real nanoworld, as one always measures a resistance, even being small. The explanation is due to the existence of the so called "quantum resistance", a resistance due to the channel-contacts interface [15], which is non-zero and small, compared to the resistance in big devices: $R = \frac{h}{q^2}\frac{1}{M}$, where M is an integer, and $\frac{h}{q^2}$ is approximately $25\,\mathrm{k}\Omega$. The inverse, the quantum conductance, is approximately $38.6\,\mu\mathrm{S}$.
Being λ the ballistic mean free path, i.e. the typical length before scattering, the total resistance of a device of length L can be written as,

$$R = \frac{h}{q^2}\frac{1}{M}\left(1 + \frac{L}{\lambda}\right)$$

where the two limits, diffusive transport for $L >> \lambda$ and ballistic transport for $L << \lambda$, are recovered.
Even with a channel of length $L = 0$ with perfect contacts, a device has a resistance equal to that of a hypothetical section of length λ.

Therefore, transport in nanostructures should be different from transport in bulk materials. The common techniques used for classical transport, such as Boltzmann equation [16], may not be useful for nanodevices, where there is a nanometer-sized active region, where quasi-ballistic transport takes place, attached to much larger electrodes (reservoirs) [15, 17]. To study such open

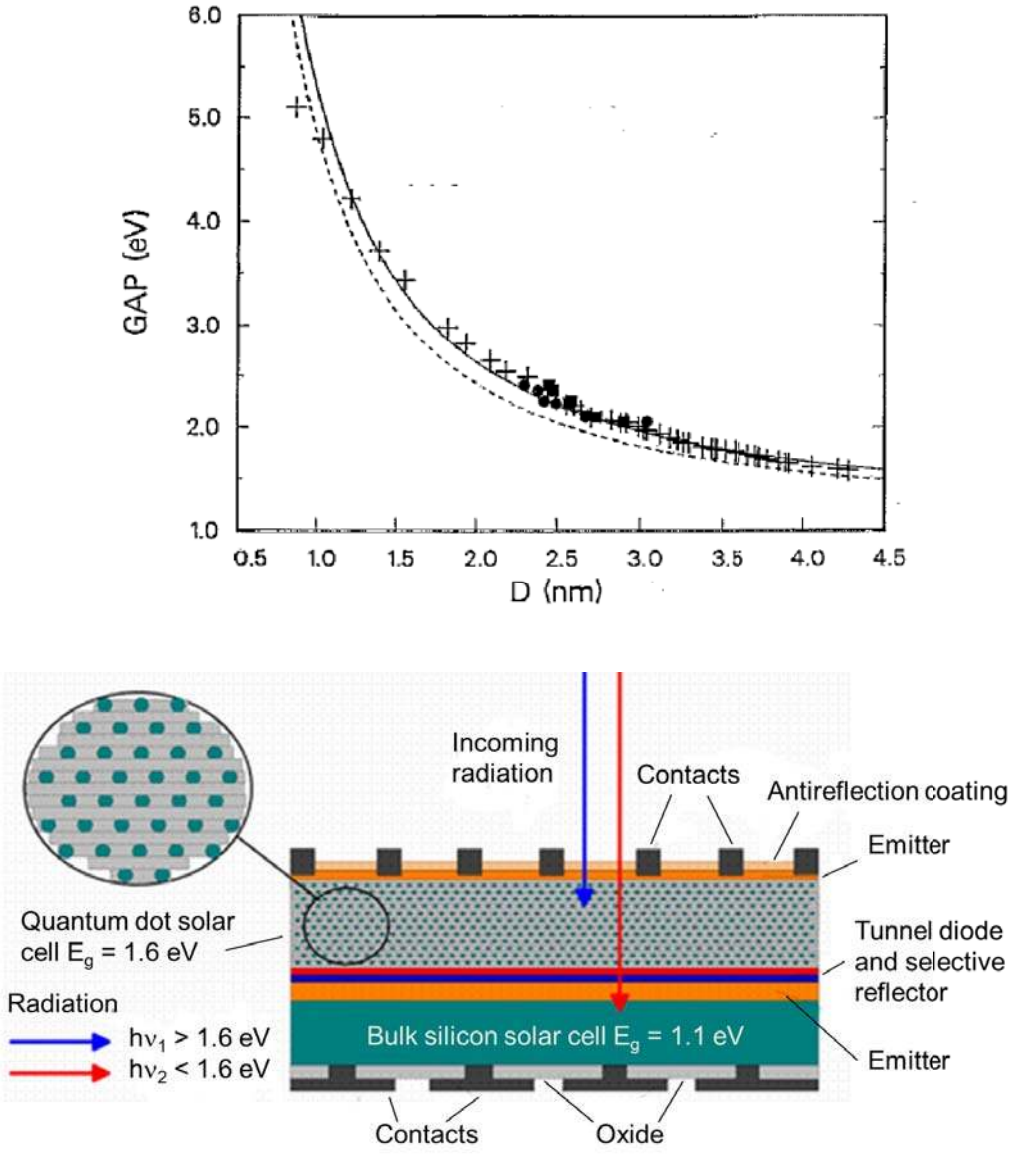

Figure 1.1: (top) Reprinted with permission from [8]. Copyright 1992, AIP Publishing LLC.: Relation between free-standing Si QD diameter and band gap. (bottom) Tandem solar cell of layers with Si QDs and bulk Si used in the european project NASCEnT.

quantum systems several approaches can be used: Quantum Master Equations [18], Transfer Hamiltonian (TH) formalism [19,20] or Non-Equilibrium Green Functions Formalism (NEGFF) [15,17,21]. The first and second one can be used for weak coupling between the electrons reservoir and the active region, hence the coupling is treated perturbatively, while the last one is used for strong coupled systems [21].

Non-Equilibrium Green Functions Formalism or Transfer Hamiltonian method?

NEGFF can be used for studying different transport material properties, such as electron conductance [22,23] or thermoelectric characteristics [21]. Generally, a Tight Binding (TB) approach is used [15] but a Density Functional Theory (DFT) approach is necessary to accurately explain the charge transfer when the intrinsic properties of the atoms in the active region are important [21]. Some computational codes that implement the DFT-NEGFF framework are Areshkin's implementation [24], MCDCAL code [25], TranSIESTA code [26], ATK code [27], MT-NEGF-DFT code [28,29], or Inelastica package [30]. In Ref. [22] an extensive method to simulate quantum photovoltaic devices using NEGFF is explained. The potentiality of the technique to treat transport atomistically was the motivation to choose NEGFF in the beginning of this PhD Thesis.
Our first steps with NEGFF showed that the treatment of bulk Si was successful. However, we observed that the computational effort demanded by NEGFF computations for systems with a large number of atoms exceeds the capabilities of the current high-computing facilities.
In order to overcome this difficulty, a different approach was searched: TH formalism together with capacitive coupling between the Si QD and the electrodes. This allowed us to study the current through the nanodevice without describing explicitly the electrode atoms and focusing the attention only in the DFT characteristics of the device active region (Si QD + matrix).
Transfer Hamiltonian (TH) method has been previously used to model tunneling current of different kind of configurations such as scanning tunnel spectroscopy [19] or resonant tunneling in semiconductor double barriers [20,31,32]. It was natural, then, to propose it for exploring the transport properties of Si QD, since the confining potential of these nanostructures can be described in the latest form.

A code to simulate electronic transport in nanostructures: SIMQdot

One of the most important features of SIMQdot is the possibility to use DOS computed by DFT, as has been done in this PhD Thesis.
A special issue not always taken into account in the description of electronic transport is how the own potential of the nanostructure influences its electronic states (was explained in Section 2.3). From a schematic point of view, electronic transport between one side and another side of the device takes place because there are occupied states with electrons on one side and available states without carriers on the other side, the distribution of the electronic states being described by the density of states (DOS) of the material. In a general view, the potential U shifts the DOS of the device while the electrochemical potential μ sets the energy where there are electrons. Thus, $\mu - U$ gives an idea of which are the really filled states [15]. This mechanism is taken into account in the transport calculations of this PhD Thesis, and it is one of the main differences with respect to other previous transport studies of nanodevices.
The program used to compute the transport in this PhD Thesis, SIMQdot, was created by Sergio Illera and coded with MATLAB©. The basis of the code can be found in the following papers: basic transport mechanisms between QDs in series or in parallel with constant transition rates and one level per QD [33], comparison of the methodology with NEGFF and extension of the model to an array of multiple QDs [34], detailed explanation of the code with the capability of using WKB approximation to describe the tunnel transmission and of using more than one state per QD, in particular the solution of the Schrödinger equation for a particle inside a spherical well inside the effective mass approximation (EMA) [35], and, finally, how to couple the electron transport with optical transitions due to incident light, like the situation in a solar cell device [36].

1.2 Brief overview of silicon quantum dots, electronic transport and the present work

Previous transport studies have been mostly concentrated on the study of single and two QDs using NEGFF [37–40] with one level of energy and constant transition rates. Arbitrary arrays of QDs are still a challenge. To our

knowledge, the unique computations of transport in an extended array have been done by: (1) Carreras et al. [41], which use a semi-empirical tunneling current model, (2) Han et al. [42] and (3) Aeberhard et al. [43] employing one energy level per QD and NEGFF; and (4) Taranko et al. [44] using one energy level per QD and the equation of motion method.
On the other hand, one of the natural descriptions of a QD inside TH formalism is as a particle inside a three dimensional square [45] or spherical [35] potential well. The main advantage of this description is that it allows describing arbitrarily big QDs.

However, our porpoise in this PhD Thesis was to take also into account the influence of the surrounding dielectric matrix and impurity atoms on the transport properties, and this features are provided through fully *ab initio* DOS. The earliest theoretical works of tunneling transport shown that one has to assume the density of states of the material as one of the main relevant factors in the calculation in order to correctly describe the experimental data [46]. Hence, we thought necessary,specially in the nanoscience field, to combine the performance of TH formalism with the accuracy of DFT for a deeper insight into the material properties. For example, DFT calculations shown that the relationship between energy gap and diameter in embedded Si QDs slightly differ from the predictions of the particle-in-a-box approximation: DFT also shows modulations related to the oxidation state of the QD and the strain induced by the matrix [47].

Moreover, the proposed model can be efficiently coded in order to allow the computation of arbitrary large arrays of multiple QDs [35]. This can be simply done within the adopted formalism by taking into account the capacitive coupling and the transmission coefficients between the QDs.
As a first step, only WKB approximation of Fowler-Nordheim (Eq. 2.46) and direct tunnel (Eq. 2.47) transmission coefficients are introduced in SIMQdot code as transport mechanisms, as they are the two more relevant tunneling mechanisms in QDs inside dielectric matrices [48, 49]. In fact, inelastic scattering has been shown to be unimportant for highly quantum confined systems, like the ones studied in the present work [50, 51]. However, TH technique can be also used to describe it by knowing the transfer matrix elements for this scattering mechanism, as has been used to study the inelastic tunnelling due to the interaction between electrons and the vibrational modes of the molecules inside a tunnel barrier [52].

Doping Si QDs

Doping is essential in opto-electronic devices as a way to improve the mechanisms to dissociate electron-hole pairs. P- and n- doped Si QDs in a SiO_2 matrix have already been achieved showing electrically activated impurity atoms located in substitutional sites which enhance the conductivity with respect to undoped samples [3, 53–56]. Previous studies show that doping a nanostructure can be totally different than a bulk system [57–59], preventing the direct application of the wide knowledge of standard doped semiconductors to nanostructures. Moreover, the promising new advances in experimental techniques to dope Si QDs as small as 2 nm [60] in a controlled way open the possibility to start overlaping the theoretical and the experimental size regimes.
In particular, a nanoscale p-n junction formed by doped Si QDs embedded in a dielectric matrix has been proposed by several authors as the basis of a third generation of solar cells [61, 62]. However, further optimization is needed in order to improve the present solar cell characteristics, such as the open circuit voltage and the low current densities (tens of microamperes per square centimetre) [10].
However, to our knowledge, theoretical studies have only been done on free-standing Si QDs [57, 58, 63–68]. With this PhD Thesis, we want to start to complete the knowledge with doping Si QDs embedded in dielectric matrices.

About the applicability of DFT results

The range of diameters used in this PhD Thesis, from 1 to 1.7 nm, is near the upper limit achievable with current computational facilities. They could seem *a priori* too small to be useful for photovoltaic applications because one may think that quantum confinement energy becomes too large or the resulting conduction between these kind of Si QDs would be extremely poor. However, it is worth stressing that common experimental samples contain QDs with a broad distribution in size, typically from 1 to 10 nm [69]. In some recent experiments, samples with narrow distributions have been produced, with average diameters of less than 2 nm [70]. Among others, their use as high energy absorbers in tandem solar cells is the touchstone of several research projects. Besides, theoretical and experimental works have already demonstrated that the smallest QDs in the samples are the most optically active ones in photoluminescense (PL) [71], while the 1 nm-sized Si QDs have

been identified as the most suitable for multiple-exciton-generation (MEG) processes, which is a highly desired condition in photovoltaic cells [72]. Regarding the confinement energy, several experimental measurements of Si QDs embedded in SiO_2 have shown that, even in the small QD limit, the gap never exceeds 2-3 eV [73].

1.3 Aim of this PhD Thesis

This Thesis initiated a collaboration between our group and the group of Prof. Ossicini of the University of Modena and Reggio Emilia, who has been modeling Si QDs for the last five years [47, 74–79]. In this context, we contributed with the capacity to study the transport properties of these models by taking advantage of mixing two different techniques, TH and DFT, which seems to open a really wide range of applications. In this PhD thesis we have only covered a single Si QD inside SiO_2 matrix, but one could in principle expand the procedure in order to explore the transport of an array of Si QDs, different dielectric matrices, include the interaction with light or with phonons, design transistors, memristors or thermoelectrics, etc. This PhD thesis provides the first steps of a procedure which seems to have no limits!

Thus, the aim of this work was to develop an approach to study transport in nanostructures by taking advantage of the atomistic information that *ab initio* methods can provide. After dealing with NEGFF, we finally decided to use TH technique for transport characteristics, much simpler than NEGFF but with similar results in the limit of weak coupling between the central active region and electrodes [34]. Thus, in this PhD Thesis we developed an approach that mixes DOS from a DFT calculation, allowing to use realistic states per QD, with TH formalism, trying to get the best characteristics from each framework. In particular, the transport through a single Si QD embedded in a SiO_2 dielectric matrix and the influence of the Si QD size, the amorphization level, and the doping were studied.

1.4 Outline

This PhD Thesis is organized as follows:

- In Chapter 2 the theory and codes used in this PhD Thesis are briefly

explained.

- In first place, concerning results, the DFT-NEGFF methodology was tested in Chapter 3. In this Chapter, a thermodynamic study of the stability of two polymorphs of Si depending on the size of Si nanowires was presented. Secondly, we studied the electronic transport properties of these two polymorphs of bulk Si in the main crystallographic directions of growth of Si nanowires.

- In second place, the study of electronic transport through a single Si QD embedded in a SiO_2 matrix is presented in Chapter 4. Firstly, the methodology DFT-TH proposed is widely studied, specially related to the parameters used in SIMQdot. Secondly, the influence on electronic transport of size and amorphization level of Si QD is showed.

- In third place, in Chapter 5, the extrinsec properties of the systems presented in the previous Chapter are studied. The p-doping (n-doping) was modelled by substituting a Si atom by a B (P) atom, in different possible impurity positions. The formation energy and structural and electronical properties are described in a first place, followed by the study of the electron current for n-doped systems and the hole current for the p-doped ones.

- Finally, a Chapter 6 with the conclusions of this PhD Thesis and a special section with possible ideas to extend the here-present work are provided.

The research leading to this PhD Thesis has been published in the following papers:

- A combination of the thermodynamical study of Si NWs stability (Section 3.2) and the electronic transport calculation of bulk Si (Section 3.3) was published in Ref. [80]: "Stability Model of Silicon Nanowire Polymorphs and First-Principle Conductivity of Bulk Silicon".

- The presentation of the methodology with the dependence of transport properties on the Si QD size and amorphization level was published in Ref. [81]: "Silicon quantum dots embedded in a SiO_2 matrix: From structural study to carrier transport properties".

- A complete study of the doping structures will be published briefly (Ref. [82]): "Doping embedded silicon quantum dots: structural and electronic transport study".

Chapter 2

Theoretical framework

The aim of this chapter is to provide a brief description of the theories underlaying the codes used in the present work to investigate our systems of interest. The *ab initio* code SIESTA based in the Density Functional Theory (DFT) was used for the morphological and electrical properties, while, for the transport properties, two different approaches were used, Non-Equilibrium Green Functions Formalism (NEGFF) with *ab initio* code TranSIESTA and Transfer Hamiltonian (TH) formalism as implemented in SIMQdot code.

2.1 Density Functional Theory

The purpose of Condensed Matter Physics is to describe real materials through the motion and interactions of the atoms that compose them, i.e. by solving the Schrödinger equation of the system. Commonly, due to the huge number of interactions involved and the difficulty to solve the interaction between many-body objects, this would be a tough task to carry out. Several theories have been developed during the last decades in order to find a simplification of the description of complex materials, being Hartree-Fock (HF) and Density Functional Theory (DFT) the most widely used. The latest one has been the commonly used for the description of semiconductor materials.

2.1.1 Some words about Hartree-Fock, correlation and exchange

Hartree-Fock (HF) theory manages the incapacity to solve the exact interaction between the electrons of a many-body system by describing their energy as the sum of the direct and exchange terms of the electron-electron interaction (Eq. 2.2). In this way, the self-exchange energy correctly cancels the self-Coulomb energy. It is a good method for systems where the high-density of the inner-shell electrons is important, like metals. However, the correlation energy is neglected in this theory and, although its contribution is small in the mentioned high density regime, HF is not suitable for systems where the low-density of valence electrons is significant, for which correlation may be as important as exchange [83]. In this context, DFT, which describes both exchange and correlation interaction, is more appropriate for semiconductor materials where the valence electrons are the protagonists. Moreover, it is also more desirable for large systems, where the combination of Slater determinants in HF would demand a huge computational effort.
The Hamiltonian for a many-body interacting system with N_e electrons in coordinates $\{\boldsymbol{r}_\mathrm{i}\}$ and N_n nuclei in coordinates $\{\boldsymbol{R}_\mathrm{I}\}$ with atomic numbers $\{Z_\mathrm{I}\}$ and mass $\{M_\mathrm{I}\}$ is, in atomic units[1]:

$$\hat{H} = -\frac{1}{2}\sum_{\mathrm{i}}^{N_e}\nabla_{\mathrm{i}}^2 - \frac{1}{2}\sum_{\mathrm{I}}^{N_n}\frac{1}{M_\mathrm{I}}\nabla_{\mathrm{I}}^2 - \sum_{\mathrm{i}}^{N_e}\sum_{\mathrm{I}}^{N_n}\frac{Z_\mathrm{I}}{|\boldsymbol{r}_\mathrm{i}-\boldsymbol{R}_\mathrm{I}|} + \frac{1}{2}\sum_{\mathrm{i}}^{N_e}\sum_{\mathrm{j}\neq\mathrm{i}}^{N_e}\frac{1}{|\boldsymbol{r}_\mathrm{i}-\boldsymbol{r}_\mathrm{j}|} + \frac{1}{2}\sum_{\mathrm{I}}^{N_n}\sum_{\mathrm{J}\neq\mathrm{I}}^{N_n}\frac{Z_\mathrm{I}Z_\mathrm{J}}{|\boldsymbol{R}_\mathrm{I}-\boldsymbol{R}_\mathrm{J}|} \tag{2.1}$$

With the Bohn-Oppenhaimer approximation (explained in Section 2.1.3), the electronic part of the Hamiltonian used in the HF approximation is:

$$\hat{H}_e = -\frac{1}{2}\sum_{\mathrm{i}}^{N_e}\nabla_{\mathrm{i}}^2 + V_{ext} + \sum_{\mathrm{i}<\mathrm{j}}^{N_e}\frac{1}{|\boldsymbol{r}_\mathrm{i}-\boldsymbol{r}_\mathrm{j}|}$$

and the energy of an interacting homogeneous electron gas is: [84, 85]

[1] In atomic units, the numerical values of the following fundamental constants are all the unity: electron mass m_e, elementary charge e, reduced Planck's constant $\hbar = \frac{\mathrm{h}}{2\pi}$, and Coulomb's constant $\frac{1}{4\pi\epsilon_0}$.

$$E_{HF} = \sum_{\mathrm{i}=1}^{N_e} \langle \mathrm{i}|H_0(\mathrm{i})|\mathrm{i}\rangle + \frac{1}{2}\sum_{\mathrm{i,j}}^{N_e} \left[\underbrace{\langle \mathrm{ij}|\frac{1}{|\boldsymbol{r}_\mathrm{i} - \boldsymbol{r}_\mathrm{j}|}|\mathrm{ij}\rangle}_{\text{direct term}} - \underbrace{\langle \mathrm{ij}|\frac{1}{|\boldsymbol{r}_\mathrm{i} - \boldsymbol{r}_\mathrm{j}|}|\mathrm{ji}\rangle}_{\text{exchange term}} \right], \tag{2.2}$$

where the wave functions of the system $|i\rangle$ are Slater determinants.
By using plane waves, one can see that the eigenvalues of this equation are plane waves with the free electron energy augmented by the exchange term

$$\epsilon(\boldsymbol{k}) = \frac{k^2}{2} - \frac{k_F}{\pi} f(x)$$

where $x = k/k_F$, the Fermi wave vector $k_F = (3\pi^2 n)^{1/3}$, n is the electron density, and $f(x) = 1 + \frac{1-x^2}{2x} ln|\frac{1+x}{1-x}|$.
Exchange interaction arises from Pauli exclusion principle where electrons are antisymmetric and cannot have the same space position and spin value, so, electrons with parallel spins tend to go away one from each other, thus, reducing the Coulomb repulsion. Hence, the exchange term contributes to lower the system energy.
The total energy per electron in the HF approximation is calculated as the sum of single electron energies $\epsilon(\boldsymbol{k})$ corrected by half of the exchange term $\epsilon_x(\boldsymbol{k})$:

$$E_{HF}/N_e = \frac{2}{N_e}\sum_{\boldsymbol{k}} \epsilon(\boldsymbol{k}) + \frac{1}{2N_e}\sum_{\boldsymbol{k}} \epsilon_x(\boldsymbol{k}) \tag{2.3}$$

where the total energy exchange per electron, for each spin channel σ is:

$$\epsilon_x^\sigma = \frac{E_x^\sigma}{N_e^\sigma} = -\frac{3}{4\pi} k_F^\sigma = -\frac{3}{4}\left(\frac{6}{\pi} n^\sigma\right)^{1/3} \tag{2.4}$$

The most known failures of HF methods are the divergence of the effective mass (due to the logarithmic term) and the huge underestimation of the cohesive energies in metals (for the case of Li, HF approximation yields to a positive cohesive energy). It is, thus, evident that the inclusion of only the exchange energy can yield to a wrong description of some materials. It has been shown that with the inclusion of correlation there is a cancellation of

errors leading to a successful description of systems (typically, DFT overestimates exchange but underestimates correlation effects).
The correlation energy, thus, is defined as the difference between the total exact energy and the HF energy, i.e. kinetic energy and exchange energy. In a general view, Pauli exclusion principle also gives a correlation in electrons' motion which is a result of the collective behavior of the electrons to screen and decrease the Coulomb interaction. Differently from the exchange term, the correlations are more important for electrons with opposite spins, because they are more likely to occupy nearby positions.
Exchange and correlation describes the effect of electron-electron repulsion, i.e. the presence of an electron in r reduces the probability of finding another electron in r'. As both the exchange and correlation terms tend to keep electrons apart, one can describe the exchange and correlation contributions in terms of a hole surrounding each electron and keeping the other electrons from approaching it. The so called exchange-correlation (XC) hole is related to DFT by an adiabatic connection set by Harris [86]. Moreover, the difference description of electrons interaction by Hartree and XC contributions can also be interpreted as the separation between short-range and long-range Coulomb effects.

2.1.2 About Density Functional Theory

Hohenberg and Kohn [87] in their famous paper of 1964 together with the paper of Kohn and Sham one year later [88] set the basis of the density functional theory (DFT), that worth the Nobel Prize of Chemistry to W. Kohn in 1998[2]. They extended the idea that Thomas [89] and Fermi [90] already had in the decade of 1920: is there a way to condensate all the degrees of freedom information present in the wave function of an interacting many body system into only one parameter, the electronic density? Hohenberg and Kohn (H-K) derived the theory that we use nowadays [87]:

> Given an interacting electron gas with an electronic density $n(\boldsymbol{r})$ in an external potential $v(\boldsymbol{r})$, there exists a universal functional of the density $F[n]$, independent of $v(\boldsymbol{r})$, with a minimum energy value $E \equiv \int v(\boldsymbol{r})n(\boldsymbol{r})d\boldsymbol{r}+F[n]$ equal to the correct ground-state (GS) energy associated to $v(\boldsymbol{r})$.

[2] http://www.nobelprize.org/nobel_prizes/chemistry/laureates/1998/kohn-lecture.pdf

> The GS is found by the minimization of the energy functional with the constrain $\int n(\boldsymbol{r})d\boldsymbol{r} = N$, N being the number of electrons in the system.
> Moreover, all the GS properties of a system can be completely described by its electron density, and the potentials can be written only as functionals of $n(\boldsymbol{r})$.

Kohn and Sham [88] (K-S) provided the self-consistent scheme to convert the interacting many-body problem into a set of non-interacting single particle equations that are the ones implemented in the *ab initio* codes available at the moment.

> From the H-K theorem it is formally possible to replace the many-electron problem by an exactly set of self-consistent one-electron equations by using an effective one-particle potential $v_{xc} \equiv \frac{\delta E_{xc}[n]}{\delta n(\boldsymbol{r})}$ in the equations and an universal functional[3] $G[n] \equiv T_s[n] + E_{xc}[n]$ in the energy variational principle. An explicit form of v_{xc} can only be obtained if the exact functional E_{xc} with all many-body effects included is known. This effective potential will, then, reproduce the exact density of the system, and the total energy will be
>
> $$E = \sum_{\mathrm{i}=1}^{N} \epsilon_{\mathrm{i}} - \frac{1}{2}\int\int \frac{n(\boldsymbol{r})n(\boldsymbol{r'})}{|\boldsymbol{r}-\boldsymbol{r'}|} d\boldsymbol{r}d\boldsymbol{r'} + E_{xc}[n] - \int v_{xc}(\boldsymbol{r})n(\boldsymbol{r})d\boldsymbol{r}, \tag{2.5}$$
>
> where ϵ_{i} are the eigenvalues of the K-S equations (Eq. 2.6).

In other words, with H-K theorem and K-S equations, the interacting system is now a system of non-interacting electrons moving in the effective one-body potential $v_{eff}(\boldsymbol{r}) = v(\boldsymbol{r}) + u([n],\boldsymbol{r}) + v_{xc}([n],\boldsymbol{r})$, where $u([n],\boldsymbol{r}) = \int d\boldsymbol{r'} \frac{n(\boldsymbol{r})}{|\boldsymbol{r}-\boldsymbol{r'}|}$ is the direct Coulomb potential and $v_{xc}([n],\boldsymbol{r}) = \frac{\delta E_{xc}[n]}{\delta n(\boldsymbol{r})}$ is the exchange-correlation potential. The equations to solve are, now ,the K-S equations, in atomic units:

[3] $G[n]$ is related to the universal functional $F[n]$ of the H-K theorem by substracting the classical Coulomb energy: $F[n] = \frac{1}{2}\int \frac{n(\boldsymbol{r})n(\boldsymbol{r'})}{|\boldsymbol{r}-\boldsymbol{r'}|} d\boldsymbol{r}d\boldsymbol{r'} + G[n]$. $T_s[n]$ is the kinetic energy of a system of non-interacting electrons with density $n(\boldsymbol{r})$, while $E_{xc}[n]$ is the exchange and correlation energy of an interacting system with density $n(\boldsymbol{r})$.

$$\left\{-\frac{1}{2}\nabla^2 + v_{eff}(\boldsymbol{r})\right\}\psi_{\mathrm{i}}(\boldsymbol{r}) = \epsilon_{\mathrm{i}}\psi_{\mathrm{i}}(\boldsymbol{r}). \tag{2.6}$$

As we don't know the exact form of the exchange-correlation functional, K-S provided two approximations to described it:

1. Local Effective Potential
   If the density of the system is sufficiently slowly varying, the exchange and correlation term of the Eq. 2.5 can be substituted by the corresponding uniform electron gas term by

   $$E_{xc}[n] = \int n(\boldsymbol{r})\epsilon_{xc}(n(\boldsymbol{r}))d\boldsymbol{r}, \tag{2.7}$$

   where $\epsilon_{xc}(n(\boldsymbol{r}))$ is the exchange and correlation energy per electron of a uniform electron gas of density n.

2. Nonlocal Effective Potential
   To include exchange effects exactly, we can use

   $$E_{xc}[n] = E_x[n] + \int n(\boldsymbol{r})\epsilon_c(n(\boldsymbol{r}))d\boldsymbol{r}, \tag{2.8}$$

   where $E_x[n]$ is the exchange energy of a HF system with density n (Eq. 2.4) and $\epsilon_c(n(\boldsymbol{r}))$ is the correlation energy per particle of a homogeneous electron gas.

The K-S paper set, then, a self-consistent procedure, called self-consistent field (SCF) method, to compute the density matrix (see Fig. 2.1 for a schema):

1. Assumption for $n(\boldsymbol{r})$

2. Construction of $\varphi(\boldsymbol{r})$ from Eq. 2.10 and of μ from Eq. 2.11 or Eq. 2.14

3. Computation of a new $n(\boldsymbol{r})$ from Eq. 2.13 and from Eq. 2.12 or Eq. 2.15

and the total energy of the system by leaving all the many-body effects in the functional $E_{xc}[n]$

$$E = \int v(\boldsymbol{r})n(\boldsymbol{r})d\boldsymbol{r} + \frac{1}{2}\int\int \frac{n(\boldsymbol{r})n(\boldsymbol{r'})}{|\boldsymbol{r}-\boldsymbol{r'}|}d\boldsymbol{r}d\boldsymbol{r'} + T_s[n] + E_{xc}[n]. \tag{2.9}$$

For the Local Effective Potential approximation,

$$\varphi(\boldsymbol{r}) = v(\boldsymbol{r}) + \int \frac{n(\boldsymbol{r'})}{|\boldsymbol{r}-\boldsymbol{r'}|}d\boldsymbol{r'} \tag{2.10}$$

and the exchange and correlation contribution to the chemical potential of a uniform gas of density n is

$$\mu_{xc}(n) = \frac{d(n\epsilon_{xc}(n))}{dn} \tag{2.11}$$

In this context, the density n is obtained by solving the one-particle Schrödinger equation

$$\left\{-\frac{1}{2}\nabla^2 + \varphi(\boldsymbol{r}) + \mu_{xc}(n(\boldsymbol{r}))\right\}\psi_{\mathrm{i}}(\boldsymbol{r}) = \epsilon_{\mathrm{i}}(\boldsymbol{r})\psi_{\mathrm{i}}(\boldsymbol{r}) \tag{2.12}$$

and setting

$$n(\boldsymbol{r}) = \sum_{\mathrm{i}=1}^{N} |\psi(\boldsymbol{r})|^2. \tag{2.13}$$

However, for the Nonlocal Effective Potential approximation,

$$\mu_c(n) = \frac{d(n\,\epsilon_c(n))}{dn} \tag{2.14}$$

and the equation to solve is now

$$\left\{-\frac{1}{2}\nabla^2 + \varphi(\boldsymbol{r}) + \mu_c(n(\boldsymbol{r}))\right\}\psi_{\mathrm{i}}(\boldsymbol{r}) - \int \frac{n_1(\boldsymbol{r},\boldsymbol{r'})}{|\boldsymbol{r}-\boldsymbol{r'}|}\psi_{\mathrm{i}}(\boldsymbol{r'})d\boldsymbol{r'} = \epsilon_{\mathrm{i}}(\boldsymbol{r})\psi_{\mathrm{i}}(\boldsymbol{r}) \tag{2.15}$$

where $n_1(\boldsymbol{r},\boldsymbol{r'}) = \sum_{\mathrm{j}=1}^{N} \psi_{\mathrm{j}}(\boldsymbol{r})\psi_{\mathrm{j}}^*(\boldsymbol{r'})$ is the one-particle density matrix as defined in Ref. [87].

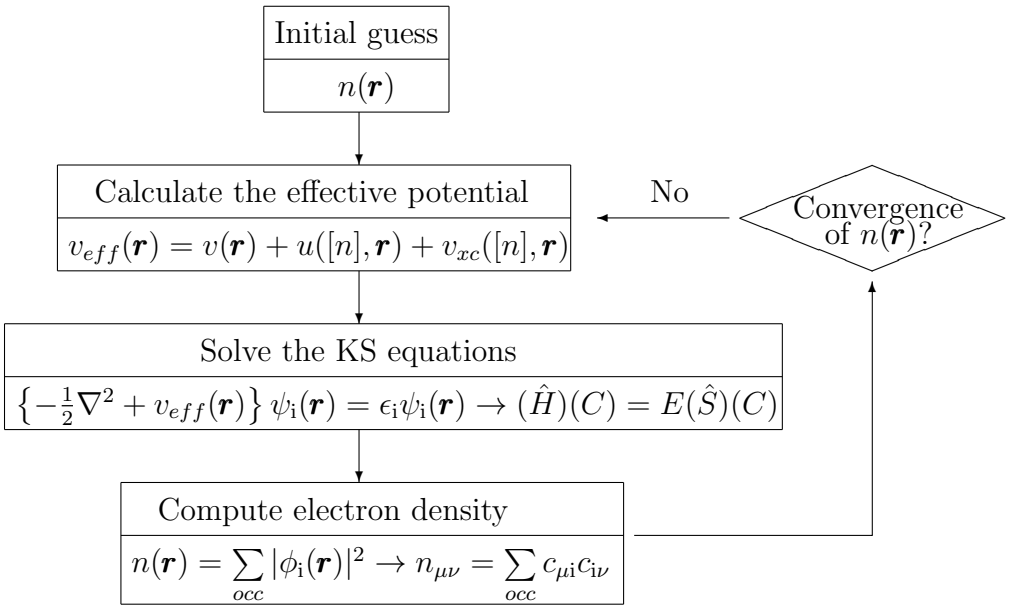

Figure 2.1: Schema of the self-consistent field cycle (SCF) in DFT calculations.

Exchange-Correlation Functional approximation: LDA and GGA

The exchange-correlation functional is only known for the free electron gas case [87]. For the other systems, two main approximation are used [91]: the Local Density Approximation (LDA) and the Generalized Gradient Approximation (GGA).

LDA (Eq. 2.7) approximates the exact exchange-correlation potential by its solely linear dependence on the electron density. It was presented by Ceperley and Alder [92] and it is normally used under the parametrization done by Perdew and Zunger (PZ) [83] or Perdew and Wang (PW92) [93].

In this way, the results of many-body calculations for the homogeneous system [92, 94] can be used into calculations for inhomogeneous systems. By construction, LDA becomes exact when the densities vary slowly enough on the scale of the local Fermi wave length $\lambda_F = 2\pi/k_F$ and the screening length [83]. Ceperley and Alder [92] used Monte Carlo calculations to determine the regions of stability of systems with intermediate densities between the two limits where the GS of an electron gas can be properly established: the limit of (a) high densities, where it is similar to a perfect gas [95], and of (b) low densities [96], where electrons crystallize.

Moreover, the parametrization of Perdew and Zunger [83] introduced a method for considerably improving the LDA results by subtracting the self-interaction energy, which emerges because there is not an exact cancellation between the direct and the exchange term in DFT.
Hence, Ceperley [94] established the parametrization for any density as, being r_s the Wigner-sphere radius in units of Bohr radii related to the electronic density by $n^{-1} = \frac{4}{3}\pi r_s^3$:

1. Exchange energy

$$E_x = -\frac{3}{4}\left(\frac{3}{\pi}\right)^{1/3} \int n(\boldsymbol{r})^{4/3} d\boldsymbol{r} \tag{2.16}$$

2. Correlation energy at low density regime, $r_s \geq 1$

$$\epsilon_c = \gamma/(1 + \beta_1\sqrt{r}_s + \beta_2 r_s) \tag{2.17}$$

3. Correlation energy at high density regime, $r_s < 1$

$$\epsilon_c = A \ln r_s + B + C r_s \ln r_s + D r_s \tag{2.18}$$

   where the values for the different constants can be found in Ref. [83, 93, 95].

The local spin-density approximation (LSDA)

$$E_{xc}^{LSDA}[n_{up}, n_{down}] = \int \epsilon_{xc}(n_{up}, n_{down}) n(\boldsymbol{r}) d\boldsymbol{r} \tag{2.19}$$

is used to explicitly take into account both spins in the calculation. An accurate description for $\epsilon_{xc}(n_{up}, n_{down})$ has been constructed from Monte Carlo simulations of jellium by Perdew et al. [83, 93].

LDA treats all systems as homogeneous. Although this is a huge approximation for real systems, normally not as homogeneous as an electron gas, it has been widely used. However, there are some known results, such as the wrong description of magnetic systems (Fe in LDA is FCC paramagnetic while in experiments it is BCC ferromagnetic), and an improvement of the approximation can be done by introducing the derivative information

of the density into the exchange-correlation functional, as it is done in the Generalized Gradient Approximation (GGA):

$$E_{xc}^{GGA} = \int d\boldsymbol{r} f(n(\boldsymbol{r}, \boldsymbol{\nabla} n(\boldsymbol{r})) \tag{2.20}$$

where the choice of the function f yields to the different GGA flavors. One of the most used is the parametrization done by Perdew, Burke and Ernzerhof (PBE) [97], where all parameters are fundamental constants, trying to simplify previous GGA parameterizations and, moreover, looking for retaining the correct features of LSDA combining them with the most energetically important features of gradient-corrected nonlocality.
A particular parametrization used in Section 3 is PBEsol [98] that was specifically constructed to improve the lattice parameter of solids, and therefore other equilibrium properties related to it such as bulk moduli, phonon frequency or ferroelectricity, and jellium surface exchange energy of solids and surfaces.

Potentially more accurate exchange-correlation functionals are

1. The meta-GGA that also includes the second derivative of the electron density [99].

2. The hybrid-functionals, where the exchange part of the energy functional is a mixture of the exact exchange energy calculated from HF theory and a DFT exchange functional [100] leading to Nonlocal Effective Potentials (Eq. 2.8) in the case of using only E_X from HF.

2.1.3 Approximations in present DFT computations and notes about the code

The DFT code used in this PhD dissertation, Spanish Initiative for Electronic Simulations with Thousands of Atoms (SIESTA), applies some approximations in order to solve real materials. The first and second approximations are always present in DFT codes whereas the third one, the use of pseudo potentials rather than the so-called all-electron calculations, is commonly used, and the last one, to use numerical atomic orbitals as a basis set, is a particularity of SIESTA, which, in principle, may let to compute big systems with less computational effort than the so-called plane waves (PW) codes. In

all electron calculations normally local orbitals are used, whereas pseudo potential methods normally use PW. However, SIESTA [101,102] is faster than other DFT codes because mixes both, local orbitals (basis set is numerical pseudo atomic orbitals of finite range) and pseudo potential approximation.

1. Bohn-Oppenhaimer approximation: decoupled movement of electrons and nuclei due to the difference in mass between them. We can consider that the kinetic energy for nuclei is much lower than the electrons kinetic energy, so nucleus are considered frozen, only the kinetic energy of electrons is taken, and the Coulomb interaction between nuclei is then fixed as an external potential.

2. Description of the exchange-correlation term of the K-S equations: as has been explained in the previous section, an approximation to the exchange-correlation potential is needed. In this PhD dissertation we used LDA and GGA, depending on the size of the systems studied.

3. Pseudo potential: Herring [103] noticed that, usually, it is not necessary to include core electrons in calculations (the core states of a solid are quite similar to those in the free atom and slightly change under electrical perturbations), so we use the so-called pseudo potential approximation, where only the valence electrons are explicititly used in the computation. To achieve the separation between core and valence electrons, one replaces the true all electon potential V_{AE} by a pseudo potential V_{PS}, that, applied to the pseudo wave functions, gives the same eigenvalues than the original atomic potential. After computing the all electron wave functions for the valence electrons of the specie under study, one creates a pseudo wave function, where the strong oscillations due to the core states are smoothed out before a certain core radius r_c (see Fig. 2.2) but it matches the all electron wave function after it. The corresponding pseudo potential matches the true potential outside the core radius.

   Differently from true wave functions, where the eigenfunctions of the valence electrons $|\psi\rangle$ are orthogonal to the core states $|c\rangle$ produced by the same potential V_{AE}, because of pseudo wave functions $|\phi\rangle$ do not have the core states, they don't have to be orthogonal to pseudo wave functions with different quantum number. As the valence states will be strongly oscillating near the atomic core, which prevents the expansion

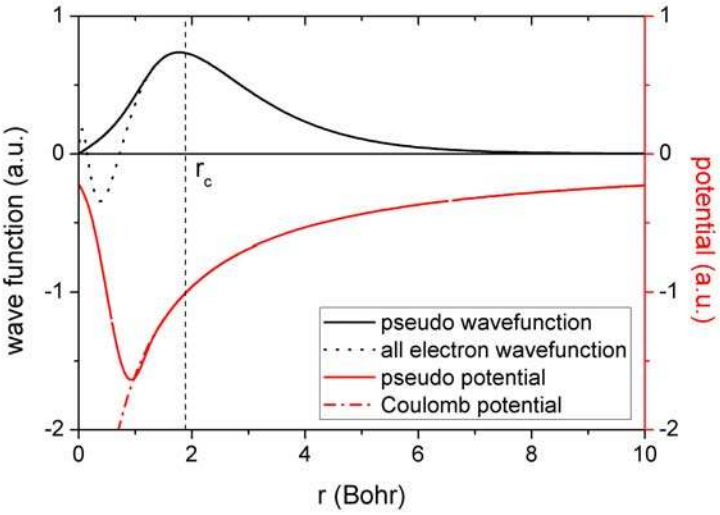

Figure 2.2: Wave function for an all electron calculation (black dot line), pseudo wave function which does not have the orthogonal part of the core electrons before r_c (black solid line), Coulomb potential (red dot line), and the generated pseudo potential (red solid line).

in terms of smoothly functions, the idea is to create a new pseudo wave function with the same eigenvalue of the valence state but without the restriction of orthogonality with the core states and that is equal to the original wave function after a certain cutoff radius.

$$\left.\begin{aligned}(T+V_{AE})|\psi\rangle &= \epsilon|\psi\rangle \\ (T+V_{AE})|c\rangle &= \epsilon_c|\psi\rangle\end{aligned}\right\} \Rightarrow \langle\psi|c\rangle = 0$$

$$|\psi\rangle = \left(\mathbb{I} - \sum_c |c\rangle\langle c|\right)|\phi\rangle \tag{2.21}$$

From the equation of the pseudo wave function $|\phi\rangle$ we can obtain the pseudo potential V_{PS} by,

$$(T + V_{AE}) \left(\mathbb{I} - \sum_c |c\rangle\langle c| \right) |\phi\rangle = \epsilon \left(\mathbb{I} - \sum_c |c\rangle\langle c| \right) |\phi\rangle$$
$$\left(T + V_{AE} + \sum_c (\epsilon - \epsilon_c) |c\rangle\langle c| \right) |\phi\rangle = \epsilon |\phi\rangle$$
$$(T + V_{PS}) |\phi\rangle = \epsilon |\phi\rangle$$

4. Basis sets: The wave functions of a system are normally expanded in a basis set in order to save computational time because computing coefficients is a much easier task than finding the wave functions value over all range of coordinates.

$$\phi_{\mathrm{i}}(\boldsymbol{r}) = \sum_\alpha c_{\mathrm{i}\alpha} f_\alpha(\boldsymbol{r}) \tag{2.22}$$

Two kinds of basis sets can be found in *ab initio* codes: not localized (PW) or localized (atomic orbitals, being gaussian or numerical). The first one is considered most accurate and it has the advantage of using only one parameter for its description: the cutoff energy or the maximum kinetic energy that the PW can have. Also, PWs have the same accuracy in all the space. However, hundreds of PW are commonly needed per each atom in order to have a proper description of a system. For the last reason, localized basis set are commonly used due to the low number of basis functions needed to have similarly precision. In particular, SIESTA uses a lineal combination of atomic orbitals (LCAO) as a basis set:

$$\phi_{\mathrm{Ilmn}}(\boldsymbol{r}) = R_{\mathrm{Iln}}(|\boldsymbol{r}_{\mathrm{I}}|) Y_{\mathrm{lm}}(\hat{\boldsymbol{r}}_{\mathrm{I}}), \tag{2.23}$$

where R_{Iln} is the radial part expressed in terms of numerical pseudo atomic orbitals with finite range, defined by their size (number of orbitals for a given $\mathrm{l\,m\,n}$), range (spatial extension of the orbitals), and shape of the radial part. Y_{lm} is the angular part in terms of spherical harmonics.
Several DFT codes use gaussian functions to describe atomic orbitals, like GAUSSIAN [104] or CRYSTAL [105], but SIESTA uses numerical

atomic orbitals (NAO) to describe wave functions, i.e. it solves numerically the radial part of the Schrödinger equation of the atom.
The size of the basis set is the number of radial functions per atom used and it could be single-ζ, i.e. one radial function per atom, or multiple-ζ, which lets the possibility to be flexible in the radial part. Finally, in order to allow a proper description of effects perturbing the symmetry of the electron density, an angular flexibility can be added to the basis set with a polarization orbital, i.e. to let the atom to have more angular momentum.
Higher size of basis set goes to the PW value of energy inside the approximation of the pseudo potential and functional of your calculation [101]. For the atoms used in this PhD dissertation, the DZP is commonly used in all the studies found in literature.
In spite of their improvement of computational time, some issues concerning the use of atomic orbitals can arise, but they can be solved using enough accuracy, i.e. by increasing the basis set size of the system under study. As an example, one of the known problems intrisic to local basis set is the basis set superposition error (BSSE), procedent from the fact that LCAO are centered on the atom instead of being homogeneus like PW. The quality of the basis is, then, geometry dependent and may lead to overstimation of the interaction energy between different species of the system.

Among the physical properties that DFT codes provide, in this PhD Thesis we were interested in:

- Total K-S energies E_{KS}
- Eigenvalues of the K-S equations ϵ_{i} and wave functions $\phi_{\mathrm{i}}(\boldsymbol{r})$
- Density of states (DOS): $g(\epsilon) = \sum_i \sum_\mu \sum_\nu c_{\mu i} c_{i\nu} S_{\mu\nu} \delta(\epsilon - \epsilon_i)$
- Projected density of states (PDOS), which corresponds to the DOS projected in the orbital μ: $\sum_i \sum_\nu c_{\mu i} c_{i\nu} S_{\mu\nu} \delta(\epsilon - \epsilon_i)$, being the overlap matrix $S = \langle \phi_\nu | \phi_\mu \rangle$ because of the use of nonorthogonal basis set.
- Mulliken population, which is an estimation for the partial atomic charge: $P_{\mu\nu} = D_{\mu\nu} S_{\mu\nu}$, in terms of the density matrix $D_{\mu\nu} = 2 \sum_i c_{\mu i} c^*_{\mu i}$,

where the sum has been done over the molecular orbitals of each basis function.

2.2 Non-Equilibrium Green Functions Formalism

When one poses the study of transport at the nanoscale some challenges emerge, such as how to deal with open systems, i.e. infinite systems but with non-periodic boundary conditions, how to describe non-equilibrium conditions, like a system with two different electrochemical potentials, or how to describe the interface between the contact and the device region. All this issues can be treated with NEGFF, and its implementation in codes such as TranSIESTA allows also to use the *ab initio* description of DFT to study nonperiodic systems, such as an atomic or molecular-scale system (the contact or central C scattering region) connected to two semi-infinite left (L) and right (R) electrode regions at different electrochemical potential. Thus, TranSIESTA code [26] uses the Keldysh formalism [106] to compute the electronic transport properties only in a finite region (L+C+R) of the infinite system.

2.2.1 Description of nanodevices inside NEGFF

NEGFF is based in the retarded GF G^R and the lesser GF $G^<$ of a system, also known as particle propagator, which describes the density of available states and how electrons occupy those states, respectively [17]. In a DFT-NEGFF framework, the retarded GF of a system is obtained by inverting the DFT Hamiltonian H and using the overlap matrices S from a given electron density, $G^R(E) = (E \cdot S - H)^{-1}$.

Self-energies or how to solve the coupling with electrodes

In macroscopic theories, the relation between contacts and device is usually fixed by the Schottky barrier height in the case of metal-semiconductor junctions. In microscopic transport theories, however, the electrode density of states and their occupation, and the coupling between the electrode and the device is required. In particular, inside NEGFF, this information is contained in the retarded electrode self-energy Σ^R.

Hence, the retarded device GF G_D^R is written in terms of the retarded GF of the isolated electrode g^R (see Eq. 2.27) and the problem of describing the coupling of the device to the reservoirs is reduced to the calculation of the contact GF, which is only needed to be known in the vicinity of the device, simplifying the computation with surface GF methods [22].

How to deal with open boundary systems: device and electrode Hamiltonian

GFs can describe non-periodic systems if we are able to separate the system Hamiltonian into two subsystems and write it as an unperturbed part H_0 and the interaction between the two subsystems V, $H = H_0 + V$. The expressions of the unperturbed Hamiltonian and the interaction are:

$$H_0 = \begin{pmatrix} H_D & 0 \\ 0 & H_E \end{pmatrix}; V = \begin{pmatrix} 0 & V \\ V^+ & 0 \end{pmatrix} \tag{2.24}$$

H_E being the Hamiltonian of the electrode and H_D of the device subsystems.

The corresponding unperturbed GF is known:

$$G_0 = (E\mathbb{I} - H_0)^{-1} = \begin{pmatrix} (E\mathbb{I} - H_D)^{-1} & 0 \\ 0 & \underbrace{(E\mathbb{I} - H_E)^{-1}}_{g^R} \end{pmatrix}. \tag{2.25}$$

From the Dyson equation,

$$G^R(E) = \begin{pmatrix} G_D^R & G_{DE}^R \\ G_{ED}^R & G_E^R \end{pmatrix} = G_0(E) + G_0(E)VG^R(E), \tag{2.26}$$

we can write the retarded GF of the device G_D^R only in terms of the retarded GF of the isolated reservoir g^R, by using the expression $G_{ED}^R = g^R V^+ G_D^R$:

$$G_D^R = [E\mathbb{I} - H_D - Vg^R V^+]^{-1} = [E\mathbb{I} - H_D - \Sigma^R]^{-1} \tag{2.27}$$

which defines the retarded boundary self-energy,

$$\Sigma^R = Vg^R V^+, \tag{2.28}$$

as the effect of the electrode on the device region.

In conclusion, the non-hermitian matrices $\Sigma_{L,R}(E)$ represent the retarded self-energies for the left (L) and right (R) electrode, and can be seen as the escape rates of electrons from the active region into the semi-infinite ideal electrodes, so that an open quantum system can be described by the non-hermitian Hamiltonian $H_{open} = H_0 + \Sigma_L(E) + \Sigma_R(E)$. The matrices $\Gamma_{L,R}(E) = \mathrm{i}[\Sigma_{L,R}(E) - \Sigma^+_{L,R}(E)]$ describe the level broadening due to the coupling to the electrodes.

2.2.2 Expressions used in TranSIESTA code

Due to the finite basis set used in TranSIESTA, the system Hamiltonian (Eq. 2.29) can be separated into three independent parts: the contact region (C), and the left (L) and right (R) electrodes.

$$H_{TranSIESTA} = \begin{pmatrix} H_L + \Sigma_L & V_{LC} & 0 \\ V_{CL} & H_C & V_{CR} \\ 0 & V_{RC} & H_R + \Sigma_R \end{pmatrix} \tag{2.29}$$

Specially important is the use of bulk electrode values in the L,R parts (Hamiltonian matrices $H_{L,R}$ and self energies $\Sigma_{L,R}$) of the system hamiltonian from a separately previous bulk calculation of the electrodes with periodic boundary conditions, as will be explained below.
The one corresponding to the interaction between electrode-contact region $V_{LC,RC}$ and the Hamiltonian of the contact region H_C are both computed explicitly with TranSIESTA GFs in an open boundary system.

Calculation of the density matrix

The computation of the density matrix is different depending on whether it is an equilibrium situation, i.e. at zero bias voltage, or a non-equilibrium one, i.e. at finite bias.

1. At equilibrium

   The integration of the lesser GF over energies determines the density matrix by,

$$D_{\mu\nu} = \frac{1}{2\pi\mathrm{i}} \int dE G^<_{\mu\nu}(E) = \int_{-\infty}^{\infty} dE \hat{\rho}_{\mu\nu}(E) f(E - \mu_F) \tag{2.30}$$

where $f(E)$ is the distribution function of the system, μ_F the chemical potential, and the spectral density matrix can be written as

$$\hat{\rho}(E) = -\frac{1}{\pi} Im[G^R(E + \mathrm{i}\delta)]. \tag{2.31}$$

In the coherent transport regime, i.e. when electron-phonon or phonon-phonon interaction are not taken into account, $G^<(E)$ can be expressed only in terms of $G^R(E) = [E \cdot S - H - \Sigma_L(E) - \Sigma_R(E)]^{-1}$.
For a given finite base set $\phi(\boldsymbol{r})$, the density matrix in the real space is

$$\rho(\boldsymbol{r}) = \sum_{\mu\nu} D_{\mu\nu} \phi_\mu(\boldsymbol{r}) \phi_\nu(\boldsymbol{r}). \tag{2.32}$$

2. At non-equilibrium

   When a finite bias voltage is applied, a difference between the left (μ_L) and right (μ_R) electrochemical potential appears and a current flows leading to a non-equilibrium situation. A description of the electrostatic potential is, then, needed.
   In TranSIESTA code it is written as:

$$V_H(\boldsymbol{r}) = \varphi(\boldsymbol{r}) + \boldsymbol{a} \cdot \boldsymbol{r} + b \tag{2.33}$$

   where $\varphi(\boldsymbol{r})$ is a solution of the Poisson's equation for a given electron density.
   The linear term is determined by imposing boundary conditions: the left electrode is at a voltage $+V_b/2$ and the right electrode at $-V_b/2$, the bias voltage applied being $eV_b = \mu_L - \mu_R$. Thus, the linear term is $-\frac{V_b}{L}\left(z - \frac{L}{2}\right)$, L being the distance between electrodes.

   The scattering states from the left electrode, similar for the right electrode, can be written in basis of the equilibrium wave function $\psi_L^0(\boldsymbol{x})$ by

$$\psi_L(\boldsymbol{x}) = \psi_L^0(\boldsymbol{x}) + \int d\boldsymbol{y} G^R(\boldsymbol{x}, \boldsymbol{y}) V_L \psi_L^0(\boldsymbol{y}). \tag{2.34}$$

   Now, the expression for the non-equilibrium density matrix is

$$D_{\mu\nu} = \int_{-\infty}^{\infty} dE \rho^L_{\mu\nu}(E) f(E-\mu_L) + \rho^R_{\mu\nu}(E) f(E-\mu_R) \tag{2.35}$$

where the spectral density matrix is defined by

$$\rho^L_{\mu\nu}(E) = \left[G^R \frac{1}{\pi} \underbrace{Im[\Sigma_L]}_{\Gamma_L} (G^R)^+ \right]_{\mu\nu} . \tag{2.36}$$

For an extended derivation of the equations see the Appendix A.

Calculation of the current in a nanodevice

TranSIESTA computes the elastic scattering by the potential of the device region. It does not treat the inelastic scattering due to electron-electron interaction, i.e. Coulomb blockade, phonons impurities, or other inelastic scattering centers.
The Landauer formalism sees the conductance of a quantum device as the transmission probability to go through this region [15, 107]. Moreover, it assumes that electrons are non-interacting particles, that the electrodes are perfect crystalline, i.e. there is no scattering inside the leads, that the electrons incident from the left (right) electrode are in thermal equilibrium with the left (right) reservoir of electrons, and that there is no back-scattering at leads interface.
Thus, under Landauer-Buttiker formalism, the transmission spectra is:

$$T(E) = \mathrm{Tr}[t^+ t], \tag{2.37}$$

t being the transmission matrix, i.e. $\psi_{out} = t\,\psi_{in}$.
The current flowing from the left to the right electrode due to a bias voltage applied V_b, is related to the probability to have transmission in this bias window $\mu_L - \mu_R$:

$$\begin{aligned} I(V_b) &= \frac{2e}{h} \left[\int dE \left(-\frac{\partial f}{\partial E} \right) T(E, V_b) \right] (\mu_L - \mu_R) \\ &= \frac{2e}{h} \int dE \, (f_L(E) - f_R(E)) \, T(E, V_b) \end{aligned} \tag{2.38}$$

where the derivative of the equilibrium Fermi distribution $f(E-E_F)$ is approximated by $\frac{\partial f}{\partial E} \sim -\frac{f(E-\mu_L)-f(E-\mu_R)}{\mu_L-\mu_R}$ and $f_{L,R}(E) = f(E-\mu_{L,R})$ are the Fermi-Dirac distribution functions of the left and right lead, respectively.

In NEGFF the transmission coefficient is computed from the self-energy and the GF of the finite system by

$$\begin{aligned} t(E) &= \left(Im[\Sigma_R(E)]\right)^{1/2} G^R(E) \left(Im[\Sigma_L(E)]\right)^{1/2} \\ &= \left(\Gamma_R(E)\right)^{1/2} G^R(E) \left(\Gamma_L(E)\right)^{1/2}. \end{aligned} \tag{2.39}$$

Procedure for computation

First of all, a finite region is needed to be described in order to perform the computation. From the GF of the infinite system

$$G(E) = \begin{pmatrix} \ldots & -V_L^+ & & & \\ -V_L^- & E{\cdot}S - H_L & -V_{LC} & & \\ & -V_{CL} & E{\cdot}S - H_C & -V_{CR} & \\ & & -V_{RC} & E{\cdot}S - H_R & -V_R^+ \\ & & & -V_R^- & \ldots \end{pmatrix}^{-1}$$

by defining a finite region with part of the left and right electrodes and the contact region, the GF of the finite system can be written as

$$G(E) = \begin{pmatrix} E{\cdot}S - H_L - \Sigma_L & -V_{LC} & 0 \\ -V_{CL} & E{\cdot}S - H_C & -V_{CR} \\ 0 & -V_{RC} & E{\cdot}S - H_R - \Sigma_R \end{pmatrix}^{-1},$$

where

$$\begin{cases} \Sigma_L = V_L g_L^R V_L^+ \\ \Sigma_R = V_R g_R^R V_R^+ \end{cases} \tag{2.40}$$

are the self-energies of the leads which describe the coupling of the explicit atoms used in the calculation of the finite system to the remaining part of the semi-infinite electrode through the unperturbed surface electrode GF $g_{L,R}^R$.

With the considerations explained in the next section, the interactions V_L

and V_R used to construct the self-energies $\Sigma_{L,R}$ are only related to the interaction between the bulk electrode and the electrode atoms that are explicitly in the finite region, not with atoms of the contact region. Thus, only electrode atoms are involved, and this quantities can be calculated from a bulk electrode calculation, a much more easy task.
The other term needed to compute $\Sigma_{L,R}$, the unperturbed surface electrode GF $g^R_{L,R}$, is also taken in the first step of the TranSIESTA procedure, a bulk calculation of the electrodes. The self-energies are computed from the initial bulk electrode calculation by cutting the bulk infinite electrodes into two semi-infinite systems and using either ideal construction [108] or efficient recursion method [109] to calculate the interactions.
Then, in a second step, a SCF cycle of the finite region is computed, and the Hamiltonian of the finite region (Eq. 2.29) is obtained from the GF rather than a normal diagonalization. With the GF, the density matrix is obtained from Eq. 2.30 and Eq. 2.35, which begins the SCF cycle again.
Finally, the transmission function is obtained with a post-processed tool, TBTrans [26], which uses the self-energies of the electrodes and the GF of the whole system (Eq. 2.39).

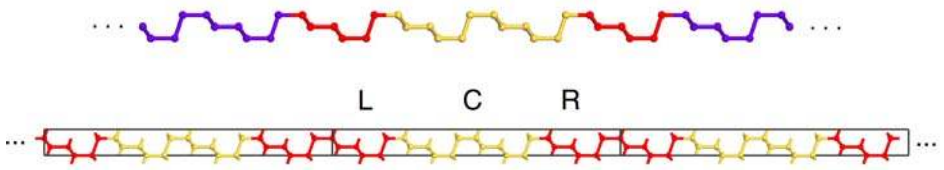

Figure 2.3: (top) From the infinite system (blue atoms in electrode goes to infinite) the finite region is the following: the selected atoms from the left L and right R electrode (red), and the central region C (yellow). (bottom) This finite region is a supercell with periodic boundary conditions in the TranSIESTA calculation.

As a conclusion, the main steps for a transport calculation inside TranSIESTA code are:

1. Definition of the system: electrodes + contact region (Fig. 2.3).

2. Periodic boundary calculation of bulk electrodes (left and right): $H_{L,R}$, $\Sigma_{L,R}$ and overlap matrices $S_{L,R}$ are computed from the K-S equation at equilibrium. Hamiltonian and density matrix (DM) values for the electrodes in the finite system are fixed to these bulk values ($c^0_{l\mu}$).

3. Open boundary calculation of the finite system L-C-R: H_C, V_{LC} and V_{CR} are computed in a supercell approach (See Fig. 2.3). Non-equilibrium density matrix $D_{\mu\nu}$ is computed from the non-equilibrium coefficients $c_{\mathrm{l}\mu} = \sum_{\nu}(GV)_{\mu\nu}c^0_{\mathrm{l}\nu}$.
   A SCF cycle starts:

   (a) reads the electrode data

   (b) builds H from the density matrix using K-S equations

   (c) solves the open problem using GFs formalism,
   $G(E) = [E\mathbb{I} - H_{transiesta}]^{-1}$

   (d) builds new density matrix,
   $D_{\mu\nu} = \sum_{\mathrm{l}} c_{\mathrm{l}\mu}c^*_{\mathrm{l}\nu}n_F(\epsilon_L - \mu_L) + \sum_{\mathrm{r}} c_{\mathrm{r}\mu}c^*_{\mathrm{r}\nu}n_F(\epsilon_R - \mu_R)$

   (e) SCF cycle repeats steps (b) to (d) until convergence.

4. Transport calculation, post-processing tool TBTrans: computation of the electron current I at the bias voltage V_b using the Eq. 2.38 and Eq. 2.39.

Considerations in the description of the system

Some considerations in the description of the system are needed in order to accomplish the approximations took in the computation.

1. The width of the bulk electrode cell has to be large enough in order to not have interaction between second neighbor cells

2. Central region C large enough in order to don't have interaction between left and right electrodes.

3. L and R leads large enough in order to don't have interaction between C and the bulk region of the electrodes.

2.2.3 Exemple of the use of NEGFF in a transport calculation

In order to clarify the above mentioned equations we can compute the current through a QD with only one energy level ϵ_1. As mentioned by Sun et al. [38]

the retarded self energy Σ^R can be seen as an energy broadening of the levels inside the contact region, due to the contact region-lead coupling V. Being Γ_L (Γ_R) this broadening due to left (right) contact, the self-energy is written as

$$\Sigma^R = -\mathrm{i}\frac{\Gamma}{2};$$

being $\Gamma = \Gamma_L + \Gamma_R$. In the special case of only one quantum dot, all the matrices are scalar terms and, thus,

$$H_C = \epsilon_1 \ ; \ \Sigma^R = -\frac{\mathrm{i}}{2}(\Gamma_L + \Gamma_R).$$

The Green Function of the system is easily written as

$$G^R = [E - H_C - \Sigma^R]^{-1} = \frac{1}{E - \epsilon_1 + \mathrm{i}\frac{\Gamma}{2}}$$

Finally, the transmission coefficient is,

$$T(E) = Tr[\Gamma_L G^R \Gamma_R (G^R)^+] = \frac{\Gamma_L \Gamma_R}{(E-\epsilon_1)^2 + \frac{\Gamma^2}{4}}$$

We can see how the transmission coefficient of one QD has a lorentzian shape peaked at the energy level and with a line width equal to Γ, the QD-lead coupling strength.
The case of two QDs in series with energy levels ϵ_1 and ϵ_2 and a coupling between them t_{12} will have only the interaction between the first QD and the left lead Γ_{L1} and between the second QD and the right lead Γ_{2R}.
The broadening and corresponding retarded self-energy will be written as

$$\Gamma = \begin{pmatrix} \Gamma_{L1} & 0 \\ 0 & \Gamma_{2R} \end{pmatrix}; \Sigma^R = -\frac{\mathrm{i}}{2}\begin{pmatrix} \Gamma_{L1} & 0 \\ 0 & \Gamma_{2R} \end{pmatrix}$$

The expression for the retarded Green Function is, then,

$$G^R(E) = \begin{pmatrix} E - \epsilon_1 + \frac{\mathrm{i}}{2}\Gamma_{L1} & -t_{12} \\ -t_{12} & E - \epsilon_2 + \frac{\mathrm{i}}{2}\Gamma_{2R} \end{pmatrix}^{-1}$$

The expression for the transmission coefficient and other examples can be found in Ref. [38]. However, the cases under study are more complicated than QDs with only one energy state. So, analytical solution is not possible and the use of DFT codes such as TranSIESTA is mandatory.

2.3 Transfer Hamiltonian formalism

The code used for transport calculations through a silicon quantum dot is based on the Transfer Hamiltonian approach for the expression of the current, and on the WKB approximation for the expressions of the transmission coefficients.

2.3.1 Transfer Hamiltonian formalism: transport in quantum devices

Payne developed in his paper [20] the method to describe resonant tunneling current by calculating the occupancy of the resonant level through an extension of TH previously adopted by Bardeen [46]. The TH technique is used to study the electronic tunneling transport through a barrier, based in the division of the tunnel junction into subsystems, each one consisting of a single electrode connected to a semi-infinite potential barrier (Fig. 2.4). In this sense, the attraction of the technique is its simplicity and that the description of transport is given in terms of the properties of only the uncoupled subsystems with the electronic states of the electrodes as a perturbation into the device, with

$$\begin{cases} H_1\psi_1 = \epsilon_1\psi_1 \\ H_2\psi_2 = \epsilon_2\psi_2 \\ H_R\psi_R = \epsilon_R\psi_R \end{cases} .$$

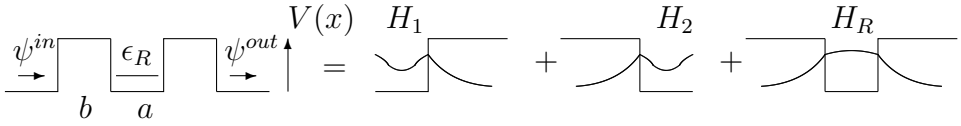

Figure 2.4: Schema of the barrier in TH formalism and how it is divided into two subsystems containing each electrode and a semi infinite barrier.

The transition rate between initial states on one side of the barrier and final states on the other side is calculated from the Fermi Golden rule, and the matrix element for the transition is [20]

$$M_{1\to 2} = \frac{\hbar^2}{2m}\int_S (\psi_1 \nabla\psi_2^* - \psi_2^*\nabla\psi_1)dS \tag{2.41}$$

where ψ are one-electron stationary states of the uncoupled subsystems and the integral is performed over a generic surface S located well inside the barrier separating the two subsystems. In this expression derived by Bardeen [46] the vanishing of the wave function of one subsystem in the other permits to simplify the notation. In this way, the distant electrode in the two subsystems is replaced by a continuation of the barrier, neglecting the reflected wave function at the interface between the distant electrode and the barrier. The current from electrode 1 to the resonant energy level ϵ_R is, (see Payne [20] for a complete explanation of the derivation of the expressions)

$$j_{1\to R} = \frac{2\pi}{\hbar} \underbrace{|M_{1\to R}|^2}_{T(E)} \rho_1(\epsilon_R)(f_1(\epsilon_R) - f_R) \tag{2.42}$$

where $M_{1\to R}$ is the transfer Hamiltonian matrix (Eq. 2.41), $\rho_1(\epsilon_R)$ is the density of states of the electrode at the resonant level, $f_1(\epsilon_R)$ is the Fermi function for electrode 1 at the resonant level and f_R is the occupancy of the resonant tunneling level. If we have a density of states instead of having only one resonant level, it would be included in the above equation (see Eq. 2.48). Similarly, the current from the resonant level to the right electrode can be written. By using the solution of the Schrödinger equation for each subsystem as is written in Payne paper [20], with the same momentum for all the wave functions of the different subsystems, the current through a double barrier with a resonant level ϵ_r is

$$j_{Res} = \frac{2k^2K^2}{(K^2+k^2)^2} \frac{1}{(a/2+1/K)} \frac{\hbar k}{m} e^{-2Kb}$$

where k is $\hbar^2k^2/2m = \epsilon_r$, and $\hbar^2K^2/2m = V - \epsilon_r$.
It is worth to note that the occupancy of the resonant level, or, in extension, the distribution function of the QD, will vary until the currents in and out the level are equal. In the code, we calculate directly this steady state, leading to a set of rate equations which allow to solve the system.

Similitude with Landauer-Buttiker formula

Similarly to Landauer-Buttiker formalism (Eq. 2.38), the current in TH formalism (Eq. 2.42) is proportional to the transmission through the device and the number of available states. A relation between them can be done by identifying the transmission coefficient T(E) with the square

of the transfer matrix and the density of states of the different elements $T_{ij}(E) = |M_{ij}|^2 \rho_i(E)\rho_j(E)$. In TH formalism, the matrix elements are obtained by Eq. 2.41. However, WKB approximation is normally used in order to simplify the calculation of the transmission coefficients [19].
The election of the transmission coefficients and QD density of states (DOS) will lead to different approaches to the description of a Si QD inside a dielectric matrix. In particular, in this PhD Thesis we use WKB approximation for direct tunnel and Fowler-Nordheim mechanisms and DFT results for Si QD DOS.

2.3.2 WKB approximation: expressions for transmission coefficients

WKB (Wentzel-Kramers-Brillouin) approximation finds a solution to 1D Schrödinger equation in sections where the potential varies slowly, i.e. the wave length $\lambda = \frac{2\pi}{k}$ is much shorter than the distance where the potential varies. Following Sakurai's book [110], a solution for the Schrödinger equation

$$\frac{d^2}{dx^2}\psi + k^2(x)\psi = 0 \tag{2.43}$$

can be of the form

$$\psi(x) = A(x)e^{iW(x)/\hbar}, \tag{2.44}$$

where $k(x) = \left[\frac{2m}{\hbar^2}(E - V(x))\right]^{1/2}$ for $E > V(x)$ and $k(x) = -i\left[\frac{2m}{\hbar^2}(V(x) - E)\right]^{1/2}$ for $E < V(x)$. For a constant potential V, one recovers the standard solution $\psi(x) = Ae^{\pm ikx}$. By introducing the ansatz Eq. 2.44 in Eq. 2.43, the following equation is obtained

$$i\hbar\frac{d^2W(x)}{dx^2} - \left(\frac{dW(x)}{dx}\right)^2 + \hbar k^2(x) = 0.$$

The condition of slowly varying potential implies, in terms of the ansatz or the potential,

$$\hbar\left|\frac{d^2W(x)}{dx^2}\right| \ll \left|\frac{dW}{dx}\right|^2 \text{ or } \left|\frac{dk(x)}{dx}\right| \ll |k(x)^2|$$

and, in terms of the wave length λ,

$$\frac{\lambda}{2\pi} \ll \frac{2(E - V(x))}{|dV(x)/dx|}.$$

Applying a series approximation until the first order [110],

$$W(x) \approx \pm\hbar \int dx' k(x') + \frac{\mathrm{i}}{2}\hbar \ln(k(x))$$

Thus, the WKB approximation of Eq. 2.44 is,

$$\psi(x) = \frac{1}{\sqrt{|k(x)|}} e^{\pm \int dx' k(x')}. \tag{2.45}$$

Solving the Schrödinger equation for a potential barrier, the transmission coefficient in this approximation reads [111]

$$T(E) = exp\left\{-\frac{2}{\hbar}\int_{x_0}^{x_1} \sqrt{2m^*_{diel}(V(x) - E)}dx\right\}$$

where x_0 and x_1 are the so-called classical turning points, where $V(x) = E$. In this PhD thesis the two more relevant tunneling mechanisms in QDs inside dielectric matrices were used [48, 49]. The expression of the transmission coefficients for Fowler-Nordheim mechanism (Eq. 2.46), which corresponds to a triangular barrier, and direct tunnel (Eq. 2.47), which is for a trapezoidal barrier, are:

$$T(E) = exp\left\{-4\frac{\sqrt{2m_{diel}}}{3\hbar q E_{diel}}\left[q\phi_1 - (E - E_{c1})\right]^{3/2}\right\} \tag{2.46}$$

$$T(E) = exp\left\{-4\frac{\sqrt{2m_{diel}}}{3\hbar q E_{diel}}\left[(q\phi_1 - E)^{3/2} - (q\phi_0 - E)^{3/2}\right]\right\} \tag{2.47}$$

being E_{diel} the electric field in the dielectric barrier, m_{diel} the effective mass inside the dielectric, E_{c1} the conduction band edge of the QD, and ϕ_1 and ϕ_0 the potential barrier height and modified potential barrier height, respectively.

2.3.3 Brief overview about SIMQdot, the code used in transport calculations

This code studies the electronic transport in nanodevices, in particular QDs embedded in dielectric matrices. It uses non-coherent rate equation approach

to obtain the charge density in each quantum dot, the TH formalism for the current expression, and transition coefficients and capacitive couplings for the interactions between QDs and between the QDs and the leads. The way to model the QDs is as spheres inside a dielectric matrix coupled to semi-infinite metallic electrodes. Then, the transport is computed by the TH through spherical quantum wells of width equal to the diameter of the QD and the capacitive coupling between the QD and the electrode is that of a sphere with an infinite plane.

Tsu-Esaki model [112] is used to describe the barriers with the following possible transitions: electron in conduction band (CB) to electron in CB of the other side of the barrier, with the corresponding effective mass of the dielectric m_e, hole in valence band (VB) to hole in VB of the other side of the barrier, with effective mass of the dielectric m_h, and electron in VB to electron in CB, with effective mass m_{eh}. The last one only appears in transport between QDs, thus, it is not used in this PhD thesis where we have focused on the electronic transport properties through a single QD.

The essential difference with respect to other approaches also capable to treat arrays of QDs [41] is the inclusion of the local potential due to the QD inside the computation of its charge. As it is well explained in Datta book [15] once a bias voltage is applied the density of states inside the QD is not static but it depends on the potential created inside the QD due to the external applied electric field.

As has been showed in earlier studies, in order to correctly explain experimental data, the inclusion of the local field created by the charge accumulated inside the QD is important [32]. In this sense, it is necessary to compute the non-equilibrium distribution function of the QD, different from the equilibrium situation where a voltage is not applied.

Following Ref. [33] (see Illera papers for a complete derivation of the formalism), the net flux (I_L) between left electrode L and contact region C (in this case the QD), I_L^+ (I_L^-) corresponding to incoming electrons from L to C (outcoming from C to L), is

$$I_L = I_L^+ - I_L^- = \frac{4\pi q}{\hbar} \int T_L(E)\rho_L(E)\rho_{QD}(E)(f_L(E) - n(E))dE, \qquad (2.48)$$

where $T_L(E)$ is the transmission coefficient between the left electrode and the first QD, $f_L(E)$ is the distribution function of the L lead, and $n(E)$ is the distribution function inside the QD.

Similarly, the net flux (I_R) between the right electrode R and the contact region, I_R^+ (I_R^-) corresponding to the incoming electrons from R to C (outcoming from C to R), is

$$I_R = I_R^+ - I_R^- = \frac{4\pi q}{\hbar} \int T_R(E)\rho_R(E)\rho_{QD}(E)\left(f_R(E) - n(E)\right) dE$$

Imposing the steady state, i.e. $\frac{dN}{dt} = I_L + I_R = 0$, in the number of electrons N inside the QD, a expression for the non-equilibrium QD distribution function n is obtained. Thus, the current I through the nanodevice, corresponding to the TH formalism, is

$$I = I_L - I_R = \frac{4\pi q}{\hbar} \int \frac{T_L(E)\rho_L(E)\rho_{QD}(E)T_R(E)\rho_R(E)}{T_L(E)\rho_L(E) + T_R(E)\rho_R(E)} \left(f_L(E) - f_R(E)\right) dE,$$

and the total number of electrons N in the QD is

$$N = \int \rho_{QD}(E)n(E)dE. \tag{2.49}$$

However, as we have stated above the voltage applied V_b to the external electrodes changes the electrostatic potential inside the QD (U=-qV). From the Poisson equation (Eq. 2.50) for the QD, we see that there is a relation between the local potential and the number of electrons inside the QD

$$\boldsymbol{\nabla}(\epsilon_r \boldsymbol{\nabla} V) = -q\frac{\Delta N}{\Omega \epsilon_0} \tag{2.50}$$

where ϵ_r is the relative permitivity of the dielectric matrix, ϵ_0 is the vacuum permitivity, and Ω the volume of the QD. The solution of the Poisson equation (Eq. 2.50) is

$$U = \underbrace{\sum_{\mathrm{j}} \frac{C_{\mathrm{j}}}{C_{tot}}(-qV_b)}_{U_L} + \underbrace{\frac{q^2}{C_{tot}}}_{U_0} \Delta N \tag{2.51}$$

where U_L is the Laplace solution of the system, C_j are the different capacitive couplings between the QD and the electrodes, C_{tot} the total capacity for the QD, U_0 is the charge energy constant, i.e. the potential increase as a consequence of the addition of one electron, and ΔN is the change in the number of electrons calculated with respect to the reference number N_0 originally in

the QD.
Hence, Eq. 2.49 has to be changed to correctly include the self charge U ($\rho_{QD}(E) \rightarrow \rho_{QD}(E-U)$), imposing a self-consistent solution for the equations of N, n and U:

1. $U = U_L + \frac{q^2}{C_{tot}}\Delta N$
2. $N = \int \rho_{QD}(E-U)n(E)dE$
3. Repeat step 1 and 2 until convergence.

Finally, just some words about the parameters that you have to provide to the code:

1. Effective mass of the electrons and holes in the valence and conduction band of the dielectric ($0.40\,m_e$ and $0.32\,m_e$ for electrons and holes inside SiO_2 matrix, respectively [113], m_e being the free electron mass).
2. Relative dielectric constant of the dielectric (3.9 for SiO_2 matrix).
3. Electron and hole barrier of the dielectric (depends on the Si QD diameter).
4. Geometrical information: dimension of the device, position and radius of each QD.
5. Density of states for each QD (in this PhD Thesis it is provided from a previous DFT calculation).

Chapter 3

Transport of bulk Si in the main crystallographic growth directions of Si nanowires

In this Chapter we present the study of the electronic transport properties through NEGFF of two polymorphs of bulk Si, namely cubic diamond and hexagonal diamond, in different crystallographic growth directions of Si nanowires (Si NWs). In this study we aimed to asses the suitability of the TranSIESTA procedure, starting with the easiest configuration, bulk Si, and having in mind more complicated structures, such as Si NWs or Si quantum dots.
A detailed description of NEGFF theoretical framework and TranSIESTA code implementation was previously done in Section 2.2.

Why the study of bulk Si?

The original goal of this PhD Thesis was the study of electronic transport in silicon nanostructures, and the framework selected to explore this field was the combination of Density Functional Theory (DFT) for the atomistic *ab initio* description of the structures and Non-Equilibrium Green Functions Formalism (NEGFF) for the computation of the electronic transport properties.
The first step was building the atomistic model for Si by means of DFT and to check its transferability, i.e. it can be used in order to obtain ground state

properties of different structures based on silicon. Secondly, it was necessary to determine if the model was plausible for its use in the NEGFF procedures. A case of scientific and technological interest in order to test our model in this first approximation to DFT-NEGFF framework was found: the influence of crystallographic direction and polymorphism on the transport of bulk Si as an approximation for electronic transport in thick Si NWs.

Si NWs belong to a unique class of semiconductor NWs because they are integrable within the conventional silicon-based device technology. In fact, the experimental realization of electronic devices with Si NWs has been already achieved [114]. For this reason, Si NWs represent a particularly attractive class of building and connecting blocks for nanodevices such as field-effect transistors (FETs) [114–116], passive diode structures [116], integrated logical circuits [117], and biosensors [118, 119]. Due to their wide range of diameters, at least five orders of magnitude between few nanometers to several hundreds micrometers [120], one can expect *a priori* different transport properties between them.
On the other hand, recent experimental [121–125] and theoretical [126–129] studies showed the possibility of other phases different than the common cubic diamond for Si, with remarkable differences in band structure, particularly their capacity of changing silicon from indirect into a direct band gap material. It is worth noting that the abundance of these polymorphism show a relation with Si NW size.

In this context, we proposed (a) studying the plausible causes for the distribution of polymorphisms in the different range of Si NWs through a thermodynamic model (see Section 3.2) and the ground state properties of these polymorphs through DFT (see Section 3.3.1) and (b) selecting the main crystallographic directions of growth of Si NWs in order to analyze the differences in electronic transport of bulk Si (see Section 3.3.2).
The above-mentioned studies will let us to set the basis for our atomistic model of Si and evaluate the applicability of DFT-NEGFF method in the more complex nanostructures we are interested in.

The band structure anisotropies of bulk Si potentially ensure a dependence of electronic transport properties on the crystallographic directions, but to date, this issue is poorly addressed in bulk Si. Moreover, the investigation of hexagonal polymorphs may have practical consequences, as semiconductor device

technology could take advantage of the materials crystallization in different polytypes, either by phase transition or at growth. For instance, in poly-Si thin films in integrated circuit devices, the twinning deformation causes formation of hexagonal structures with electronic consequences [130, 131].
Therefore, the lack of theoretical studies about transport dependence on the orientation of bulk Si and the technological interest on the polymorphisms of Si motivated us to investigate the effects of the internal atomic structure and polymorphism of bulk Si in its transport properties. Recent experiments have provided convincing evidence that most Si NWs grow around a monocrystalline bulk Si core [132] and that the transport is mainly inside it, hence, the study of bulk Si as an approximation to the thickest range of Si NWs is justified. It is, thus, interesting to assess the impact of the crystal structure on the transport properties of bulk Si and to determine which orientation is best suited to the engineering of not-ultra-thin Si NW-based devices.

Previous studies of transport in Si NWs: from ultrathin to thick Si NWs

Even in Si NWs with sizes of the scale of tens of nanometers, the number of atoms grow easily up to hundred of thousands of atoms, which is unreachable from an atomistic description point of view. To describe them by *ab initio* methods, the number of atoms is a key parameter, reaching the limit of current computational facilities for only the small range of Si NWs, up to 6 nm of diameter.
In the literature, interesting electronic and transport properties of ultrathin cubic diamond Si NWs were reported with DFT [133–138] and Tight Binding (TB) [139–142] models. As a matter of fact, metallic or semimetallic behavior depending on the reconstruction of $\langle 100 \rangle$ Si NWs (diameter $d = 1.5$ nm) [133, 134], the strongly dependence of transport in $\langle 110 \rangle$ Si NWs ($d = 1.5$ nm) on impurity position [135], cagelike NWs have higher electrical conductivity than tetrahedral NWs ($d = 2$ nm) [141], or the importance of the conducting subbands width on transport properties of doped Si NWs in different directions ($d \sim 1$ nm) [136] were reported.
The works of Ng et al. [137], who calculated the I-V characteristic in different directions of 1 nm wide Si NWs by DFT-NEGFF, and those of Persson et al. [142], who studied the charge transport dependence on NW orientation in disordered 2 nm wide Si NWs, suggest that surface reconstruction leads to surface conducting states, which may contribute to enhance the conduc-

tivity with respect to bulk Si. For these Si NWs of $d \sim$ 1-2 nm the preferred direction for electron transport was $\langle 110 \rangle$, which also has a smaller effective mass than the other crystallographic directions in Si NWs up to 6 nm of diameter [138, 142].
Approaches based on semiclassical equations, like Boltzmann equation [143], allowed computing bigger systems up to 300 nm wide wires.
To our knowledge, no theoretical work concerning thick SiNWs based on *ab initio* methods has been published yet. Thus, we propose here to study the bulk behavior with first-principles methods in order to approximate the transport properties in thick Si NWs.

3.1 Computational details

All *ab intitio* calculations of the thermodynamic stability of Si NWs were performed with CRYSTAL06 [105] code within the B3LYP approximation. This code was chosen in order to speed up the computations of fully atomistic models of Si NWs by taking advantage of the point symmetries in the NW model. A 3-21 G(d) type basis set was adopted with a 0.6 a_0^{-2} exponent for the d polarization function. The two scaling factors were 1.387 and 1.354 for the inner and outer valence shells, respectively, as proposed by Cargnoni and Gatti [144]. Thresholds for the truncation of the Coulombic and exchange series were set to 6 6 6 6 16 and the shrinking factor for the Monkhorst-Pack net to 8 for both lattices. The DFT computation of each Si NW was done in a week with a 32-core machine.
On the other hand, the DFT-NEGFF framework was used to study bulk transport properties. First, SIESTA code [101, 102] was used for the relaxation of the structures and further structural study. Subsequently, TranSIESTA code [26] was used for the electronic transport properties.
The small size of our systems, as they were not computationally-demanding, allowed us to use a GGA functional, which tends to improve total and atomization energies [145–147], structural energy differences [148, 149], and, in general, gives better structural parameters with respect to experimental ones [147]. Specifically, PBEsol, a special parametrization for solids of PBE, was used due to the better lattice constants and jellium surface exchange energies it gives [98]. Solutions of the Kohn-Sham equations were expanded as linear combination of atomic orbitals (LCAO) of finite range, with a kinetic energy cutoff of 0.02 Ry. The basis set used was standard double-ζ plus

polarization (DZP). Real space mesh cutoff and k-grid values were set to converge total energy values within 0.1 meV and maximum absolute forces over atoms better than 0.004 eV/Å in all cases (we used a mesh cutoff of 300 Ry and a kgrid value of 30Å). The relaxation with SIESTA of bulk supercells were done in few hours per each system with a 24-core machine. However, to compute a whole *I-V* curve with TranSIESTA took around 10 days with a 24-core machine, per system.

3.2 Thermodynamic model for the stability of polymorphs in Si NWs

Recent experiments reported the evidence of the stability of a polymorph different than standard cubic diamond in a certain diameter range of Si NWs, synthesized by standard chemical-vapor-deposition assisted with Au catalyst [121]. HRTEM analysis [121] and Raman spectroscopy measurements [124, 150] confirmed the coexistence of two different phases, namely, cubic diamond (with cubic structure and space group Fd3m, from thereafter called "cubic") and hexagonal diamond (with hexagonal wurtzite structure and space group $P6_3mc$, from thereafter called 'hexagonal"). Single-crystal and single-phase nanowires were obtained (only one polymorph per NW) in both cases.
Dominance of one or the other phase seems to be related to the NW diameter (see Figure 3.1). In particular, thinner NWs (diameters below 20 nm) are mainly cubic-like, whereas average-size NWs (between 20 and 100 nm) are mainly hexagonal-like and thicker ones are again cubic, as expected for bulk silicon.

To explain this situation we used a thermodynamic model based on the parametric description of the Gibbs free energy of each system: the minimization of this parameter is related to the stability of the polymorhps, i.e. the lower the Gibbs free energy, the more stable the polymorph is. The formulation done by Barnard et al. [151, 152] was used, who proposed the following expression for the Gibbs free energy of a nanostructure in terms of the bulk and surface contributions:

$$G_x^0 = G_x^{bulk} + G_x^{surface} \tag{3.1}$$

where

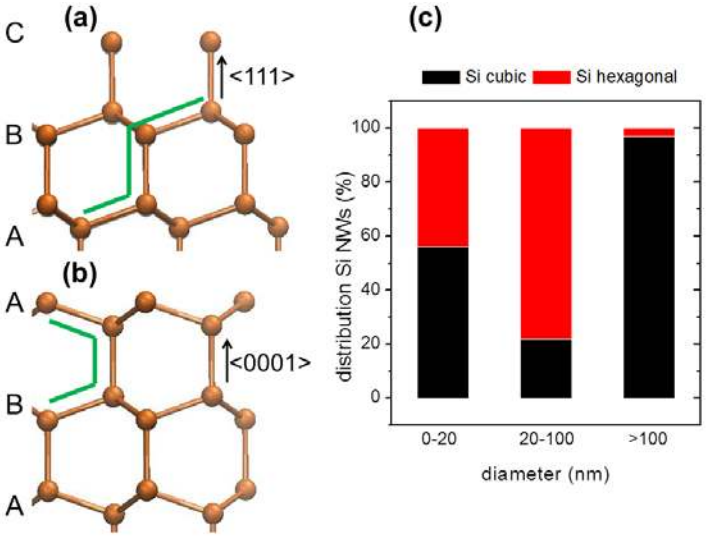

Figure 3.1: Theoretical considerations on the structure. Comparison of the stacking of the tetrahedra in (a) cubic diamond and (b) hexagonal diamond structures. The diamond structure can be understood as an ABC stacking along the ⟨111⟩ direction, whereas the hexagonal can be understood as ABA stacking along the ⟨0001⟩ direction. (c) Distribution of Si NW polymorphs depending on the size (adapted from Fontcuberta i Morral et al. [121]).

$$\begin{cases} G_x^{bulk} = \Delta_f G_x^0 \\ G_x^{surface} = \dfrac{M}{\rho_x} q \sum_j g_j \gamma_{xj} \end{cases} \tag{3.2}$$

in terms of the molar mass M, the density ρ_x of the material in the phase x, the surface to volume ratio q, and the surface Gibbs free energy γ_{xj} of facet j per surface area. $\Delta_f G_x^0$ is defined as the standard free energy of formation. The weighting factors g_j are defined so that $\sum_j g_j = 1$. The ratio q can be evaluated explicitly for each nanostructure as a function of its radius on the basis of geometrical considerations. Since only one family of planes faceting each nanostrucuture exists, we can assume $g = 1$.

The values G_x^0 and γ_{xj} were previously calculated by *ab initio* bulk and surface calculations, respectively, for the facet {121} of the cubic diamond phase in the ⟨111⟩ direction, and for the facets {110} and {100} of the hexagonal diamond phase in the ⟨001⟩ direction, which were the experimental cross sections found in Ref. [121]. Other facets for the cubic diamond phase were calculated (see Table 3.1) seeing that {121} is one of the lowest configuration

for this polymorph.

polymorphism	Si cubic				Si hexagonal	
facet	{111}	{121}	{110}	{100}	{110}	{100}
surface free energy (J/m^2)	1.92	1.95	2.13	2.47	1.37	1.54

Table 3.1: Surface Gibbs free energies γ_{xj} for the surface terminations and phases under study.

As expected, mean surface free energy γ_x for the different facets of hexagonal phase is about $0.6\,J/m^2$ smaller than the cubic phase. Therefore, due to the tendency of systems to minimize the total energy, we expect this phase to be more stable in the range where the surface to volume ratio is important, i.e in thin NW range.

In Fig. 3.2, we see, by plotting Eq. 3.1, that the hexagonal phase is about 12 kJ/mol less stable than cubic Si in the bulk region (see high number of atoms, i.e. thicker NW range). The inset in Fig. 3.2 shows that the crossover between the Gibbs free energies of hexagonal NWs and cubic NWs occurs at an equivalent diameter of 100 nm long, making the hexagonal nanostructures more stable for NWs thinner than 100 nm in diameter (few atoms).

Notice that this model is able to predict only one single crossover of the energies, corresponding to the transition from the nano- to the microscale (around 100 nm). This means that metastable phases in the macroscale can be stable in the nanoscale range due to the contribution of the surface in the thermodynamic stability, which plays a major role as the size decreases. This is consistent with the experiments. However, in order to recover the cubic diamond as a stable phase in the range below 20 nm diameter, the effect of two different contributions only important in the nanometric range (edges and planar defects) were explored.

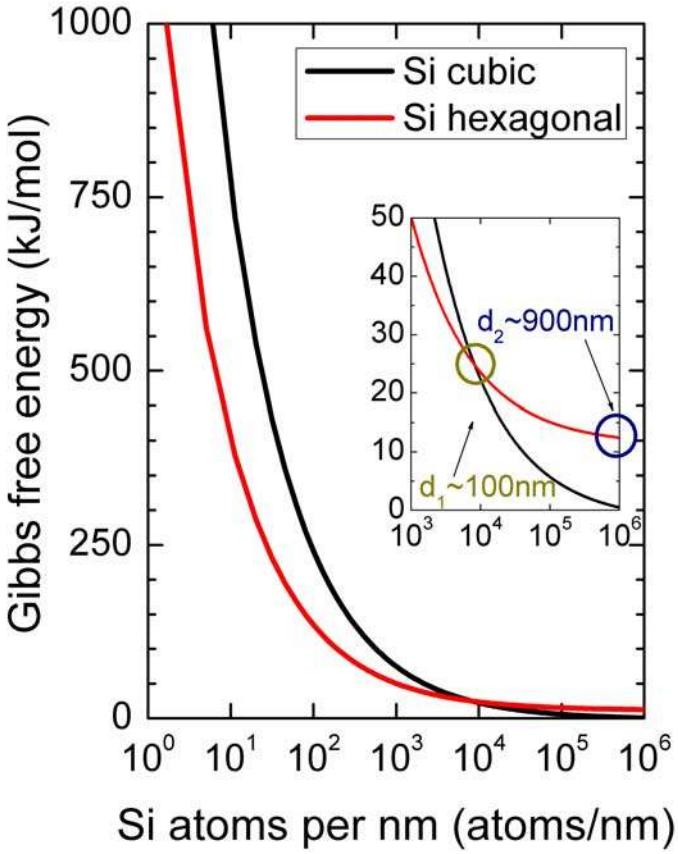

Figure 3.2: Gibbs free energy versus the number of atoms per nanometer in length of the nanowire for cubic (red line) and hexagonal (blue line) polymorphs. Crossovers of the different polymorphs are detailed in the inset.

Effect of Edges: Fully Atomistic Calculation

Edge contributions are particularly complex to introduce in the previous analytic model [151]. For this reason, DFT computations of selected diameters of Si NWs (between 2-10 nm) were performed (see Ref. [80] for more details). These simulations implicitly take into account all the contributions to the Gibbs free energy in pristine Si NWs: bulk, surface, edges, and other possible terms, such as the surface stress contributions. The results obtained with full *ab initio* calculations (discrete data points in Fig. 3.3) were qualitatively compatible with the results obtained with the analytic model for the Gibbs free energy, meaning that edge effects, and other implicit contributions to the free energy of thin NWs, decrease the values but do not significantly alter the conclusions drawn previously.

Effect of Planar Defects

HRTEM observations of defective Si NWs have shown that planar twins are the most common planar defect and they usually take place in the cubic phase [122, 123]. In a cubic silicon structure, these defects represent a 60° rotation of the structure along the ⟨111⟩ axis (see right panel of Fig. 3.3). Interestingly, the resulting local atomic arrangement is analogue to the hexagonal phase.
The contribution of planar defects to the total Gibbs free energy can be expressed as

$$G^{def} = \frac{M}{\rho} q_{def} n_{def} \gamma_{def} - \frac{n_{def}}{n_{total}} \Delta G^0 \tag{3.3}$$

where q_{def} is the plane to volume ratio of the atoms contained in the defect, n_{def} is the number of atoms in the planar defect per surface unit, and γ_{def} is the plane free energy of the defect. In order to avoid double-counting of the energy contribution from the atoms in the defect (first term in Eq. 3.3), the bulk contribution of these atoms must be susbtracted from the Gibbs free energy (second term in Eq. 3.3). The values of γ_{def} were evaluated from *ab initio* calculations of the total energy of a bulk supercell containing a planar defect (see Ref. [80] for more details).
Structural analyses of defective Si NWs also revealed that the density of defects is strongly variable [122]. For this reason, several defect densities, i.e. number of planar defects perpendicular to the NW axis per unit length, of

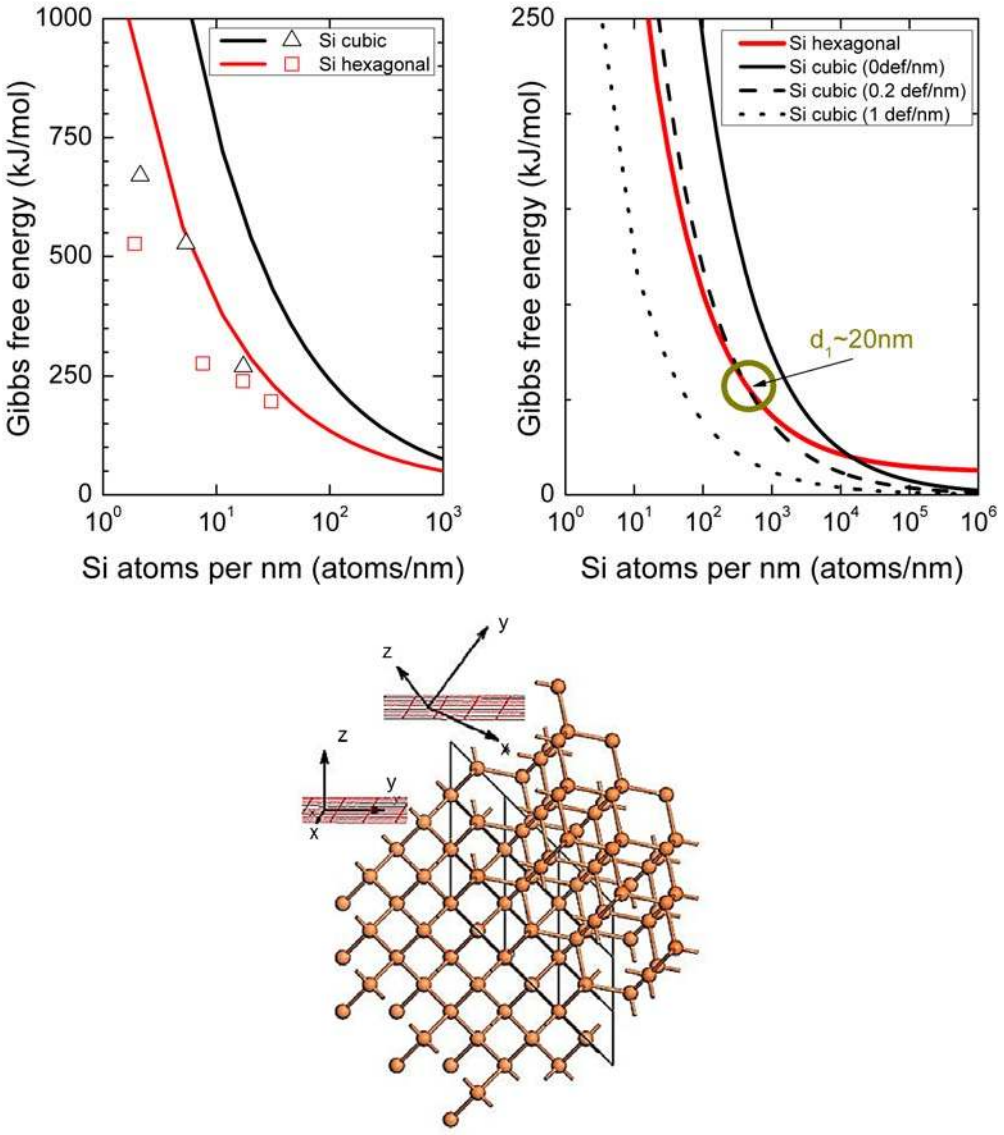

Figure 3.3: Gibbs free energy as a function of the number of atoms per nanometer in length of the nanowire (left) from thermodynamic model of Eq. 3.1 (solid lines) and from DFT calculation of Si NWs (discrete data point) for cubic (red) and hexagonal (blue) polymorphs, and (right) from thermodynamic model of Eq. 3.3 for the hexagonal phase (blue line) and the cubic phase with different number of defects per nanometer (red lines). (bottom) Planar twin created by rotation of 60° along the cubic ⟨111⟩ axis.

cubic-like Si NWs were considered modifying g_{def} and n_{def} in Eq. 3.3. They are compared to a pristine hexagonal Si NW in Fig. 3.3.
Our results clearly demonstrate (a) that the defect contribution reduces the energy of cubic Si NWs and (b) that at certain defect densities this reduction is enough to explain the thermodynamic feasibility of the cubic phase in thin nanowires. Specifically, 0.2 defects per nm are enough to reproduce the crossover between cubic and hexagonal phases at corresponding diameter of 20 nm. Thus, planar defects are a plausible explanation for the crossover of the distribution in lower diameter range.

3.3 Electronic transport in bulk Si

An atractive scenario emerge from the above thermodynamic study suficiently simple to start using NEGFF: which would be the most suitable growth direction and polymorph of Si NWs, in each range of diameters, in terms of electronic transport? We started to study bulk Si as an approximation for the transport in thick Si NWs, while the smallest range of Si NWs have been already covered by several studies (Section 3). It is worth to mention that technological limitations in the integration of ultra-thin Si NWs ($d < 15$ nm) in real devices hinder the applicability of those results [153] and current synthesis techniques can furbish us with a wide range of Si NWs with radically different crystallographic and electronic properties ($\langle 001 \rangle$ in Ref. [154, 155], $\langle 110 \rangle$ in Ref. [154–157], and $\langle 111 \rangle$ in Ref. [156–158]) that are expected to display different transport properties, according to the here-reported results. However, an exhaustive work providing experimental evidences of such effects is still missing in the literature and also there is a total lack of studies about the impact of the crystallographic direction in electronic properties of bulk Si. Here, we present a theoretical study of the electron transport properties of bulk Si along the most significant growth directions of Si NWs [120]: $\langle 001 \rangle_{\mathrm{d}}$, $\langle 110 \rangle_{\mathrm{d}}$ and $\langle 111 \rangle_{\mathrm{d}}$ for the cubic phase, and $\langle 001 \rangle_{\mathrm{h}}$ for the hexagonal phase (cross sections can be found in Fig. 3.4).

3.3.1 Atomistic models of the main growth directions of Si NWs

In Fig. 3.5 there is an scheme of the system under study: a central scatter region (C) connected to two semi-infinite left (L) and right (R) electrodes,

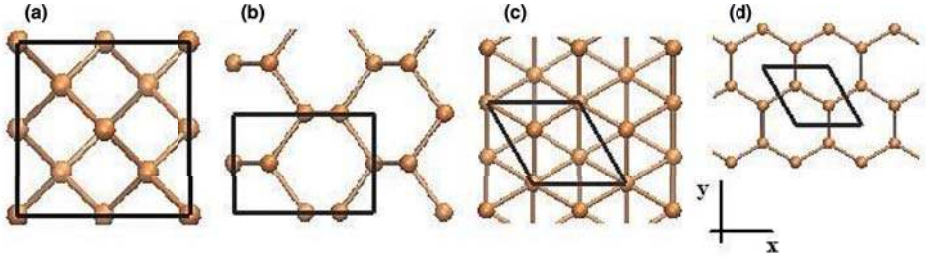

Figure 3.4: Cross section of bulk Si along each direction of interest: (a) $\langle 001 \rangle_{\mathrm{d}}$, (b) $\langle 110 \rangle_{\mathrm{d}}$, and (c) $\langle 111 \rangle_{\mathrm{d}}$ for the cubic phase and (d) $\langle 001 \rangle_{\mathrm{h}}$ for the hexagonal phase. In black is represented the unit cell for each crystallographic direction.

where the electron current is computed when an external bias voltage V_b is applied, V_b being proportional to the difference between the electrochemical potential of the left lead μ_L and right lead μ_R, $\mathrm{e}V_b = \mu_L - \mu_R$. The electrodes and scatter region were both of bulk silicon in the same crystallographic direction, as it is commonly done in this kind of studies [159].

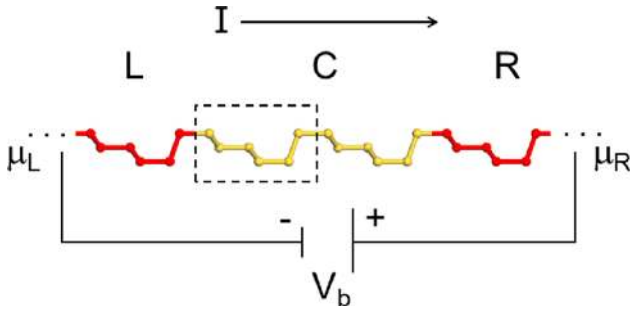

Figure 3.5: Scheme of the different regions in a TranSIESTA computation for the $\langle 111 \rangle_{\mathrm{d}}$ direction: left (L) and right (R) semi-infinite electrodes and the central scatter region (C). An electron current I is created when a bias voltage V_b, proportional to the difference between the electrochemical potential of the left (μ_L) and right (μ_R) lead, is applied. The unit cell is represented with a dashed line.

The number of atoms per electrode unit cell and scatter central region unit cell was different for each crystallographic direction, because of the difference in unit cell length for the different directions. Hence, in order to (a) ensure a good electrode behavior as a reservoir of electrons and (b) preventing the overlap between left and right electrode, it was necessary to find the minimal number of unit cells specific for each direction for the electrode and scattering region, respectively (see Table 3.2).
The structural properties of cubic diamond (space group Fd3m, IT number 227) and hexagonal diamond (space group $P6_3mc$, IT number 186) poly-

	$\langle 001\rangle_{\mathrm{d}}$	$\langle 110\rangle_{\mathrm{d}}$	$\langle 111\rangle_{\mathrm{d}}$	$\langle 001\rangle_{\mathrm{h}}$
atoms/unit cell	8	4	6	4
unit cells/electrode	2	3	1	2
unit cells/central region	2	3	2	2
atoms in total/system	48	36	24	24
cross section (Å× Å)	5.47×5.47	5.47×3.87	3.87×3.87	3.85×3.85
central region length (Å)	10.95	11.61	9.48	12.73

Table 3.2: Description of the unit cells for each crystallographic direction. Note that the cross section for $\langle 001\rangle_{\mathrm{d}}$ and $\langle 110\rangle_{\mathrm{d}}$ is cubic, i.e. angles of 90° 90° 90°, and the cross section for $\langle 111\rangle_{\mathrm{d}}$ and $\langle 001\rangle_{\mathrm{h}}$ is hexagonal, i.e. angles of 90° 90° 120°.

morphs were reported in Ref. [80]. Specially interesting is the difference of 0.012 eV in the total energy per atom between polymorphs, confirming the stability of cubic diamond in bulk Si, and the difference of 0.17 eV in band gap energy between polymorphs, being hexagonal diamond the smaller one, in accordance with other theoretical [126] and experimental studies [122,160]. This give us confidence on the proposed model in order to describe polymorphism on bulk Si.

3.3.2 Si bulk transport properties

I-V characteristics

The current-voltage I-V characteristics and the transmission spectra $T(E)$ of the different crystallographic directions were computed (Fig. 3.6). In order to prevent possible geometrical effects, due to the differences in the lattice parameter, we present the current *density*, i.e. the current per surface unit cell perpendicular to the transport.
We checked that an electrode size larger than the minimal electrode unit cell for each direction (see Table 3.2) does not alter the transport properties. This confirms that our electrodes' models are good enough to study the differences in the electronic transport of the scattering central region: these electrodes, spite being a semiconductor, act as a real infinite reservoirs of electrons that can be sent from one side and be collected in the other, being dispersed by the central region. Thus, upon conduction, electron transport is only limited by the properties of the central scattering region. Moreover, the influence of the scatter region was checked, finding a smaller current for

a larger scattering central region, as expected. This way, the final unit cells used in the calculation were the smallest ones to valence accuracy and computational cost. Finally, as regards the intrinsic variations in the number of atoms of the scattering central region due to the differences in the crystal structure of each direction, it must be beard in mind that each one of these models represents the minimum structural unit in which transport along a given crystallographic direction can be defined. In other words, the relative differences and ordering of the *I-V* characteristics predicted per structural unit in each direction should still be valid for NWs with different orientations containing similar number of such elementary transport units.

As we can expect due to the anisotropy of the band diagram of bulk Si, there is a different behavior of transport in the different directions. Once activated the ballistic transport, there is a greater conduction for the $\langle 001 \rangle_{\mathrm{d}}$, followed by the $\langle 110 \rangle_{\mathrm{d}}$ and $\langle 001 \rangle_{\mathrm{h}}$, and being the last one the $\langle 111 \rangle_{\mathrm{d}}$. Moreover, the conduction gap, i.e. the voltage at which the current starts significantly to grow, is smaller for hexagonal phase than for cubic phase related to the difference in band gap value between polymorphs.

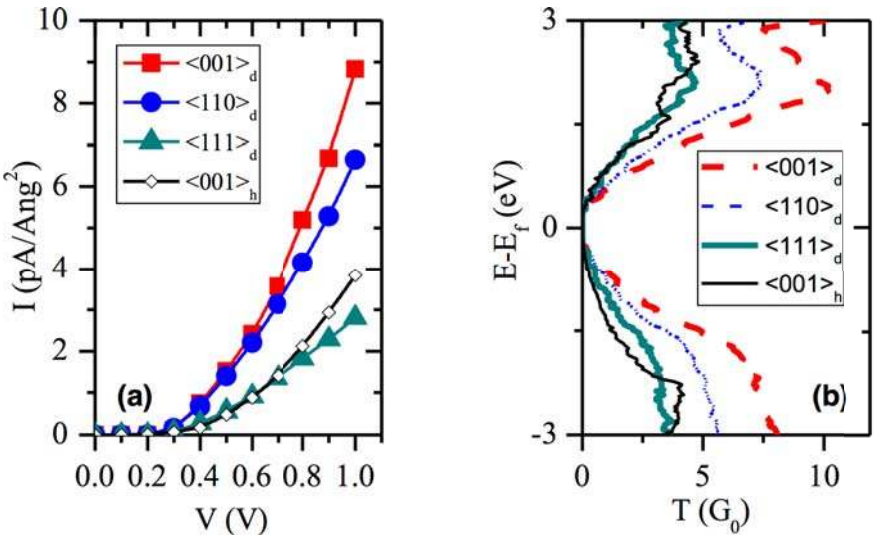

Figure 3.6: (left) *I-V* characteristic (*I* in this case is the current per unit of transversal area) of bulk Si in the systems under study. (right) Zero-bias transmission spectra (G_0 is the quantum of conductance) for each direction of interest.

From the linear part of the computed *I-V* characteristic, we have extracted the ballistic conductance G_B in each direction, commonly shown in bulk ma-

terials as conductance per unit area (Table 3.3). Referring to the dimensions of each unit cell (width W and length L) and assuming that the current flows homogeneously through the channel, we can calculate the corresponding conductivity as $\sigma = G_B L/W$. The order of conductances and their value in bulk Si is different than ultrathin Si NWs [137], because confinement effects alter the band diagram of materials [142]. In this sense, the election of the growth direction of Si NWs in different ranges of diameters should be related to the different behavior of transport properties depending on their size.

Wave function orbitals, band structure and CBM effective mass: preferred direction for transport

	$\langle 001 \rangle_{\mathrm{d}}$	$\langle 110 \rangle_{\mathrm{d}}$	$\langle 111 \rangle_{\mathrm{d}}$	$\langle 001 \rangle_{\mathrm{h}}$
G_B (10^4 S/cm^2)	18.15	12.45	4.90	8.55
σ (S/cm)	0.019	0.014	0.009	0.011
m_e^* (m_e)	0.86	1.21	1.59	1.10
$E_c - E_F$ (eV)	0.20	0.36	1.06	0.69

Table 3.3: Calculated conductance and conductivity from the *I-V* characteristic, and effective mass of the conduction band minimum (CBM) and energy difference between CBM and Fermi energy extracted from the band structure along each direction of interest.

Fine features of the electron structure were explored in order to find an explanation for the ordering of the conductances. Theoretical studies of ultrathin Si NWs computed the effective mass in each direction by fitting a parabolic curve for the conduction band minimum (CBM) [142], with the direction with less effective mass being the one that has a higher conductance. Inside cubic polymorph, this parameter has a direct correlation with conductance (see the band structure for each system in Fig. 3.7). However, it seems that transport properties among polymorphs are the result of a balance (see Table 3.3) of the effect of (a) the effective mass m^* (response to an external electric field and, from a material point of view, it would be related to the change in velocity of an electron moving in that direction), (b) the relative energy difference between the CBM E_c and the Fermi energy E_F (carrier concentration n of the CBM, Eq. 3.4, is related exponentially to this energy difference), and (c) the probability of the electron to be along the direction of transport (related to the projection of the lowest unoccupied molecular

orbital (LUMO) into the transport direction, see Fig. 3.8). A direct correlation between the $E_c - E_F$ energy difference and conductance is found for all the systems.
Assuming parabolic bands in general theory of semiconductors, the carrier concentration in conduction band n in non-degenerate semiconductors is described as:

$$n = 2\left(\frac{2\pi(m_l^* m_t^{*2})^{1/3} k_B T}{h^2}\right)^{3/2} exp\left(-\frac{E_c - E_F}{k_B T}\right) \tag{3.4}$$

where m_l^* and m_t^* are the longitudinal and transverse effective mass, respectively, k_B is the Boltzmann constant, h is the Planck constant, E_c is the energy corresponding to the minimum of the conduction band, and E_F the Fermi energy, respectively.

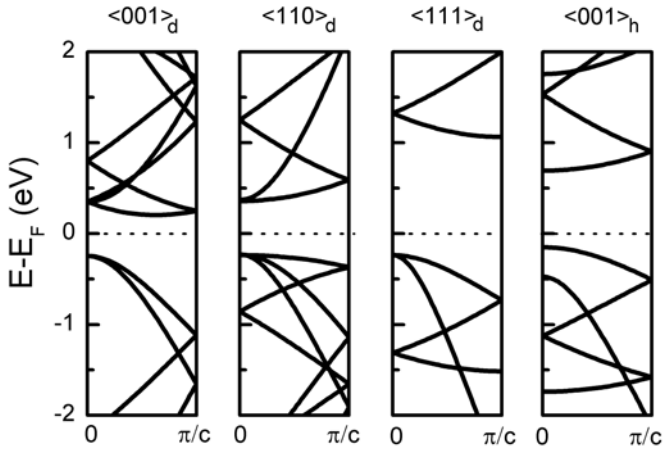

Figure 3.7: Band structure along the z axis for each system.

It is well known that the minimum of the conduction band in bulk Si are ellipses along the $\langle 001\rangle_{\mathrm{d}}$ direction, in contrast with the valence orbitals that are found along the $\langle 111\rangle_{\mathrm{d}}$ direction. Hence, $\langle 001\rangle_{\mathrm{d}}$ is more probably occupied by conductive electrons than other direction minima (it is supported by a high occupancy n) and hence transport in that direction is enhanced. Also, m^* in this direction is lower than the others, so the electrons will move faster along it, contributing to a higher conductance. Direction $\langle 111\rangle_{\mathrm{d}}$, though, has the lowest conductance, due to the fact of having the largest effective mass and smallest occupancy n. The case of $\langle 110\rangle_{\mathrm{d}}$ and $\langle 001\rangle_{\mathrm{h}}$ is interesting because

m^* of the $\langle 110 \rangle_d$ is larger than $\langle 001 \rangle_h$ but the occupancy of $\langle 001 \rangle_h$ is lower than $\langle 110 \rangle_d$, and, finally, $\langle 110 \rangle_d$ has higher conductivity. Although DFT is a ground state theory, the information in the qualitative shape of excited states is commonly used. The orbital for CBM (LUMO) in each direction supports this behavior and gives a qualitative information about the possible space orientation of conduction electrons probability. The probability of an electron to be along the transport direction (z axis) is higher in the $\langle 001 \rangle_d$ and $\langle 110 \rangle_d$ directions than in $\langle 001 \rangle_h$ or $\langle 111 \rangle_d$, where the orbitals are mostly perpendicular to the transport direction.

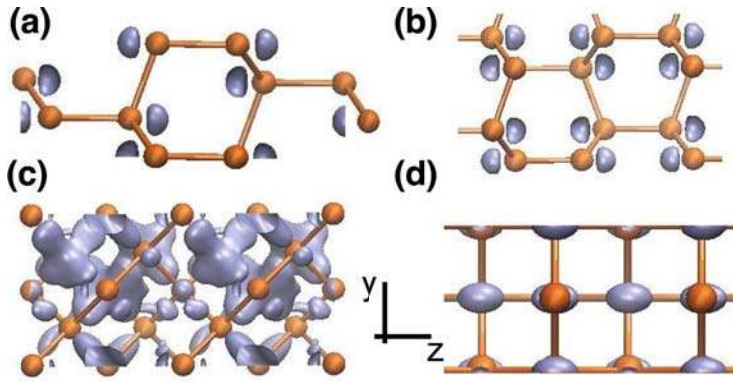

Figure 3.8: Kohn-Sham orbitals at 70% of their maximum amplitude of the LUMO state for the directions (a) $\langle 111 \rangle_d$ with two valleys, (b) $\langle 001 \rangle_h$ with one valley, (c) $\langle 001 \rangle_d$ with six valleys, and (d) $\langle 110 \rangle_d$ with one valley. The plots are in the yz plane, with the z axis being the direction of transport.

Finally, it is worth giving a comment about the values of our conductivities, which are about three orders of magnitude higher than the standard value for bulk Si in freshman physics books [161]. TranSIESTA code only computes elastic transport and does not take into account inelastic scatter due to phonons or impurities. Thus, it can largely overestimate the experimental values obtained for bulk Si. Also, conductivity in Si NWs is not fully reproduced by our model, because it does not contain surface states, which seem to be responsible for the reported large conductivities in NWs [137, 162].

3.3.3 Transport properties of a planar defect

From the thermodynamical study we saw that planar defects are an explanation for the stability of cubic diamond in ultra thin Si NWs. We present here preliminary results of the influence of planar defects on electronic transport. We did not do an extensive study of them due to their complexity and

divergence from the original theme of study of this PhD Thesis, i.e. silicon quantum dots. Moreover, we had already decided not to continue with this DFT-NEGFF methodology. However, the preliminary results show that a deep study of them would be really interesting for a future work.

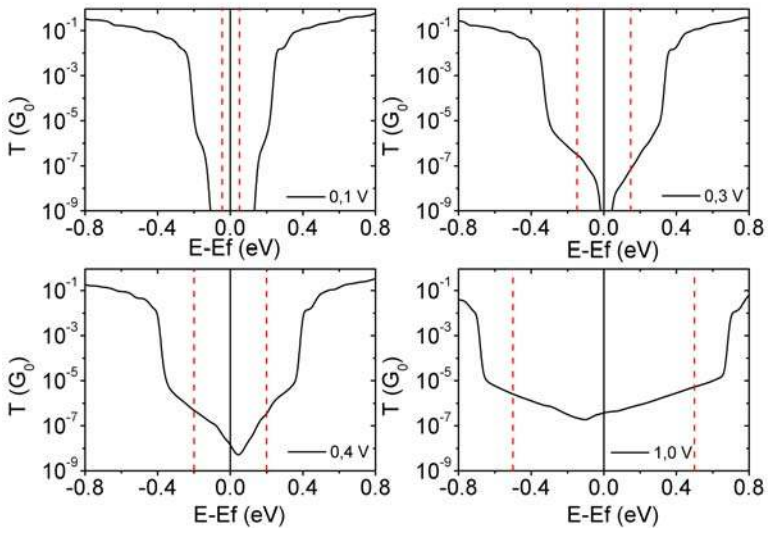

Figure 3.9: Transmission spectra for different bias voltage in the $\langle 001 \rangle_{\mathrm{h}}$ direction ($E_g = 0.36\,\mathrm{eV}$).

Following Ref. [163], we started with a planar defect on the hexagonal bulk structure, by making a 60° twin of one plane of atoms. In a next step, we would compare it with a twin in the $\langle 111 \rangle$ direction of cubic bulk structure as described in Section 3.2.

In Fig. 3.9 we see how the transmission channel is opened when the states of the scattering central region lay in between the valence band (VB) of left electrode and the conduction band (CB) of the right electrode. This occurs because the polarization V_b produces a relative displacement of the electrodes energy bands: the Fermi level of the left electrode is shifted up to eV_b/2 and the Fermi level of the right electrode is shifted down to - eV_b/2. Hence, the energetic distance between the VB of the left electrode and the CB of the right electrode decreases with V_b. When there is an overlapping between the valence and conduction states of both electrodes, i.e. when V_b is of the order of E_g, transmission spectra is non zero in all the range of integrated energies and the conduction starts to grow exponentially. However, we can see in the

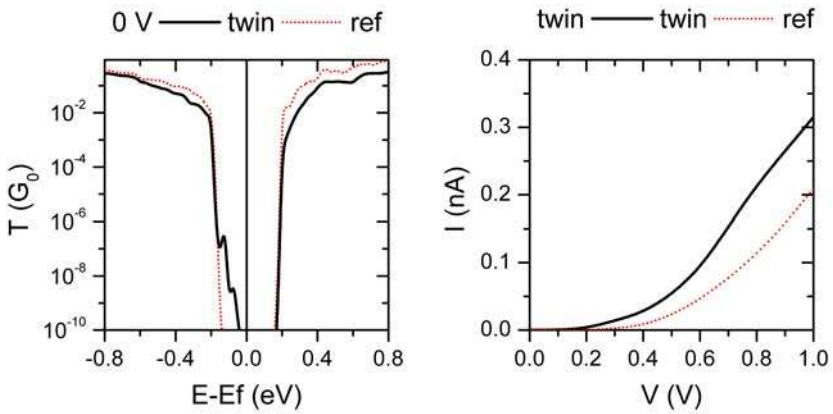

Figure 3.10: (left) Zero bias transmission spectra and (right) I-V characteristic for an structure with a twin (the pristine structure is shown for comparison).

I-V characteristics (Fig. 3.6) that there is a small but significant value of the current for V_b smaller than E_g, due the small but non-zero value of the transmission function in some energies of the conduction window around E_F for those V_b (see top right pannel of Fig. 3.9).

Thus, we can see that the inclusion of a defect creates a state in the forbidden gap, drastically changing the transmission spectra and letting the conduction to start at a V_b smaller than E_g, doubling the final current value (Fig. 3.10).

3.4 Conclusions

In this Chapter we covered the study of Si polymorphism and Si NWs as a sufficiently simple, but interesting, test problem for the implementation of DFT-NEGFF procedure. After deeply studied its rangle of applicability, we determined that it was not the optimum simulation framework to address the study of Si QD systems.
The main conclusions of this Chapter are summarized below.

3.4.1 Thermodynamic model for the stability of polymorphs in Si NWs

This study intends to cover the gap between the minute dimensions of current atomistic models of NWs (d < 4 nm) and the typical sizes of real nanodevices (d > 15 nm). In the latter range, the electrical transport phenomena are still dominated by bulk properties, being bulk Si a good approximation to mimic the transport properties in thick Si NWs [164]. As we have seen, the direction most suitable for electron transport is different between thin Si NWs and bulk Si, hence, it is important to take into account the difference in electronic transport due to the size of the Si NWs used in order to properly design a device. We have shown how *ab initio* modeling of electron transport can provide theoretical hints and guidelines to improve and taylor the performance of Si NW-based devices.

Through an analytic model for the Gibbs free energy, the stability of different Si polymorphs at different NW diameter has been described, taking into account contributions from volume, surface, edge, and planar defects. This model predicts three different ranges of diameters, which correspond to the ones observed experimentally. The thicker Si NWs (>100 nm) are made of bulk Si in the cubic phase, due to the lower bulk free energy of this polymorph. In the intermediate range (20-100 nm), the surface to volume ratio becomes more important and, being the hexagonal phase the polymorph with a lower surface free energy, Si NWs tend to grow in the hexagonal phase in this range. Finally, for NWs with lower diameters (<20 nm), a certain density of planar defects in cubic Si NWs makes this phase the most stable one.

3.4.2 Electronic transport in bulk Si

By the study of transport properties of bulk Si with NEGFF, we found a dependence of electron transport on the crystallographic direction and polymorph of bulk Si. This is due to the anisotropy of band structure, being the $\langle 001 \rangle_{\mathrm{d}}$ the most suitable for electronic transport and $\langle 111 \rangle_{\mathrm{d}}$ the direction with the lowest conductance. Although the hexagonal polymorph has a lower conductance than directions $\langle 001 \rangle$ and $\langle 110 \rangle$ of cubic diamond, it has a smaller band gap and conduction takes place earlier. This feature can be interesting for some applications.
Different aspects of the electron structure may influence in the qualitative

order of the *I-V* characteristic at high voltages. The minimum of the CBM of bulk Si is located along the $\langle 001 \rangle$ direction, hence, this direction has the highest probability to be occupied and transport in this direction is enhanced. Concerning the LUMO orbitals, the probability of electrons being along the transport direction (z axis) is higher for the directions $\langle 001 \rangle_{\mathrm{d}}$ and $\langle 110 \rangle_{\mathrm{d}}$, with orbitals along the transport direction, than for $\langle 001 \rangle_{\mathrm{h}}$ and $\langle 111 \rangle_{\mathrm{d}}$ with perpendicular orbitals to transport direction. The effective mass associated to a minimum of an energy band along a certain direction is related to the response of an electron to an external field, hence, a lower effective mass will lead to a faster response to it and more conductance in this direction. Thus, $\langle 001 \rangle_{\mathrm{d}}$ ($\langle 111 \rangle_{\mathrm{d}}$) being the direction with the smallest (highest) effective mass, it corresponds the highest (lowest) conductance. In the directions where it is similar ($\langle 110 \rangle_{\mathrm{d}}$ and $\langle 001 \rangle_{\mathrm{h}}$), the shape of the conduction orbitals (LUMO) is essential in the transport, with the direction with orbitals perpendicular to the transport being the one with lower conductance. Finally, from a classical point of view, the occupancy of the CBM is related to the energy difference between the CBM and the Fermi energy. We saw a direct correlation between this quantity and the conductance en each direction.

3.4.3 DFT-NEGFF methodology to study transport in nanostructures

Finally, on one hand, we have satisfactorily tested our DFT models for silicon and, on the other hand, we have seen that NEGFF methodology is not suitable for the study of more complex systems. Mainly, this is due to the explicitly description of the electrodes in DFT-NEGFF computations, which increases the final number of atoms and hinders the description of the system due to the introduction of a metall/oxide heterojunction (increasing in a not desired way the complexity of the systems). This kind of system can grow easily to 700 atoms, due to the large Al electrodes (a 5×5×2 supercell per electrode) needed to couple the 2×2×2 silica matrix. Moreover, we had important problems to converge the non-equilibrium density matrix with NEGFF of such a system, never founding a solution for the SCF cycle and having huge oscillations of the charge computed by the program.
For this reason, we have decided to use transfer Hamiltonian (TH) formalism to compute the electronic transport through silicon quantum dots in the following Chapters. The main advantage of TH recalls in its simplicity due

to the non atomistic description of the electrodes, which allows to focus only in a DFT description of the scattering central region.

Chapter 4

Silicon quantum dots embedded in a SiO_2 matrix

As mentioned in previous sections, the aim of this PhD Thesis was the modelling of electronic transport in devices based in silicon quantum dots (Si QDs) embedded in dielectric matrices. Among the possible materials for the dielectric matrix, we focused on silicon oxide (SiO_2) due to its technological relevance and wide description, both in experimental and theoretical works [10]. Other matrices, such as silicon carbide (SiC) or silicon nitride (Si_xN_y), are starting to be modeled in the last years, and are still poorly adressed in the experimental literature [165–170]. The knowledge about embedded Si QDs of the last decade shows that the optical and electrical properties of Si QDs are strongly dependent on the size and the crystallinity of the QD [171, 172], hence, we expect an influence of these parameters in the electron transport properties.

After discarting DFT-NEGFF as a suitable method for our systems, we present in this section the study of the electronic transport properties, through Transfer Hamiltonian (TH) method, of a Si QD embedded in a SiO_2 matrix and the influence of Si QD size and the amorphization level of the strucure. It is worth noting that TH is a suitable description only valid for systems with a weak coupling between active region and electrodes.

A detailed description of TH formalism and its implementation in SIMQdot was done in Section 2.3.

In particular, firstly, the structural relaxation of the systems will be done by DFT. Secondly, the projected density of states (PDOS) of the subsystem formed by the Si atoms of the QD and the O shell surrounding will

be computed, followed by the extraction of the energy barrier height values for each system. Finally, both PDOS and energy barrier hieght values will be provided to the code SIMQdot which will compute a current-voltage *I-V* characteristic by TH method.
With this study we are interested in setting the basis of the DFT-TH procedure, starting with the transport through one single QD, but having in mind other possible extensions of the work presented in Section 6.2.

4.1 Computational details

The relaxation of all the systems and the calculation of the DOS were computed with the DFT code SIESTA [101, 102]. Calculations were performed using norm-conserving Troullier-Martins [173] pseudopotentials with nonlinear core corrections within the Local Density Approximation (LDA) with a Ceperley-Alder [92] exchange-correlation potential, as parameterized by Perdew-Zunger [83]. It is worth noting that, differently from the previous section calculations where GGA was used, LDA exchange-correlation potential was used in all QD computations of this PhD thesis due to the large number of atoms forming the embedded QD systems (around 700 atoms). A cut-off of 250 Ry on the electron density and no additional external pressure or stress was applied. All the calculations were performed at 0 K temperature with only Gamma point k-sampling and standard double-ζ basis set for all the atoms. Atomic positions and cell parameters have been left totally free to move and the structures were relaxed by conjugate gradients minimization until forces were below 0.04 eV/Å in all the atoms. The relaxation with SIESTA of each Si QD took around 10 days with a 64-core machine, while the computation of each PDOS took less than a day with a 16-core machine. For the sake of comparison, all the systems have the same oxide thickness of 1.1 nm between the SiQD and the electrodes in the electronic transport computations with SIMQdot code. This value is in the typical range where tunneling is measured [174]. The relative dielectric constant of the oxide value used was 3.9, while the oxide effective mass of electrons and holes was set to $0.40\,m_e$ and $0.32\,m_e$, respectively [113], m_e being the free electron mass. Each *I-V* curve is computed in about five minutes with SIMQdot code in a standard computer.

4.2 Description of the systems

Among the different ways to construct a Si QD embedded in a silicon oxide matrix, we followed the methodology proposed by Ossicini et al., verified in several previous studies [47, 74–78].
Since, in real systems, QDs are characterized by a certain amount of amorphization, especially at small QD sizes, we have considered the two opposite ideal cases of perfectly crystalline and completely amorphous systems. The β-cristobalite SiO_2 matrix, in the following named c-SiO_2, was adopted for the crystalline phase since it is the simplest Si/SiO_2 interface due to its diamond-like structure [175]. The glass model for amorphous SiO_2, in the following named a-SiO_2 or silica, was generated using classical molecular-dynamics simulations of quenching from a melt, as described in Ref. [176].
Starting from a SiO_2 supercell, the QD was created by removing the O atoms inside a sphere of a given cut-off radius and relaxing the structure with SIESTA code.
In Fig. 4.1 the differences are clearly visible between the different grade of crystallization of both kind of systems.

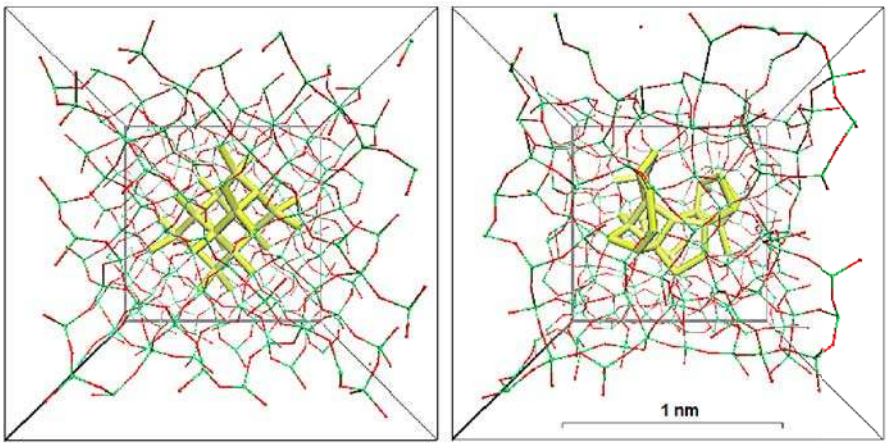

Figure 4.1: Ground-state structure of the QD of 32 Si atoms in β-cristobalite (left panel) and in silica (right panel). Red spheres are O atoms, green spheres are Si atoms, and the yellow thick sticks represent the Si atoms of the QD.

Different systems characterized by the number of Si atoms forming the QD were studied (see Table 4.1), namely c-Si_{10}, c-Si_{17}, c-Si_{32}, c-Si_{35} and c-Si_{47}

for crystalline Si QDs of 10, 17, 32, 35, and 47 Si atoms; and a-Si_{10}, a-Si_{17}, a-Si_{32}, a-Si_{35}, and a-Si_{47} for amorphous Si QDs. All the structures were created from a 3×3×3 supercell $Si_{216}O_{432}$ of 21.5 Å of size, except the Si_{10} QDs which were created from a 2×2×2 supercell $Si_{64}O_{128}$ of 14.32 Å of size.
It is worth mentioning that we have decided to remove some of the above systems from the computational set for the *I-V* characteristics. On one hand, the smallest QD (the Si_{10}) was neglected, since it is formed solely by Si interface atoms, and no Si core atoms. We have observed that such condition renders the Si_{10} unsuitable for comparison with the other QDs. And, on the other hand, the a-Si_{35} system creates two subsystems, one small cluster of three Si atoms and another cluster of 32 Si atoms, due to the deformation of the QD after the relaxation. As we are studying pristine Si QDs, without any kind of defect, we decided to exclude it from the following results.

After the relaxation, the bond length of Si atoms inside the QD approaches the bulk Si value. For this reason, we propose to use the bulk Si atomic density $\rho_a = N_a/a^3$, with $N_a = 8$ Si atoms in a cubic cell of side a = 5.39 Å, to estimate the corresponding final QD radius r_{QD} (which differs from the original cut-off radius). Considering that the QD is formed by n_{Si} Si atoms and n_O interface O atoms, we propose to evaluate r_{QD} from:

$$\frac{(n_{Si} + n_O)}{\rho_a} = \frac{4}{3}\pi r_{QD}^3. \tag{4.1}$$

The oxidation state Ω for each Si QD is described following Guerra et al., by

$$\Omega = \frac{\text{interface O atoms}}{\text{interface Si atoms}}. \tag{4.2}$$

4.3 Electronic structure

The electronic properties of the systems were calculated with SIESTA code. We were specially interested in the density of states, fundamental parameter for the transport calculations.
Therefore, the DOS of the different systems were computed, and the density of states projected into the subsystem formed by the Si atoms of the QD and the first shell of O atoms surrounding it was extracted. These PDOS will be the one used in the transport calculation of Section 4.4.

	Si atoms	Si interface atoms	Si core atoms	O interface atoms	d (nm)	Ω
c-Si_{10}	10	0	10	16	0.99	1.6
c-Si_{17}	17	5	12	36	1.25	3.0
c-Si_{32}	32	12	20	32	1.49	2.8
c-Si_{35}	35	5	30	36	1.38	1.2
c-Si_{47}	47	17	30	60	1.59	2.0
a-Si_{10}	10	1	9	20	1.04	2.2
a-Si_{17}	17	5	12	33	1.23	2.8
a-Si_{32}	32	7	25	45	1.42	1.8
a-Si_{35}	35	9	26	46	1.45	1.8
a-Si_{47}	47	16	31	59	1.58	1.9

Table 4.1: Description of the atoms composing each Si QD (Si core atoms and Si interface atoms) and the O shell surrounding it, the Si QD diameter (d), and the oxidation state (Ω) of each system.

Results in Fig. 4.2 clearly show the decrease of energy band gap and the increase of electronic states for increasing QD sizes. Due to the induced deformation by the embedded Si QD of the surrounding matrix, c-SiO_2 matrix tends to lose its symmetry after the atomic relaxation, behaving as the amorphous one. Hence, the DOS of the a-SiO_2 matrix has been used as reference also for crystalline structures.

The reason for including the interface O atoms as part of the description of the QD, both in the definition of the QD radius and in the PDOS, is that they form states that behave as part of the QD, and not of the embedding matrix [77]. This can be seen in the fact that the behavior of (1) free-standing hydrogenated QDs is different from that of (2) free-standing oxygenated QDs and (3) Si QDs embedded in SiO_2 matrix, due to the absence of O atoms at the QD surface in the first case. It is worth noting that in free-standing hydrogenated QDs the energy gap is related to the QD diameter solely by the quantum confinement [8], while in the second and third case, the surrounding O atoms and the stress induced by the embedding matrix have an important role over the optical and electrical properties. In case (3), the band gap is almost completely determined by the barrier provided by the first shell of O atoms, while a competition between the oxidation (that tends to blue-shift the absorption spectra) and the strain induced by the embedding matrix (that tends to red-shift it) has been observed [47, 177].

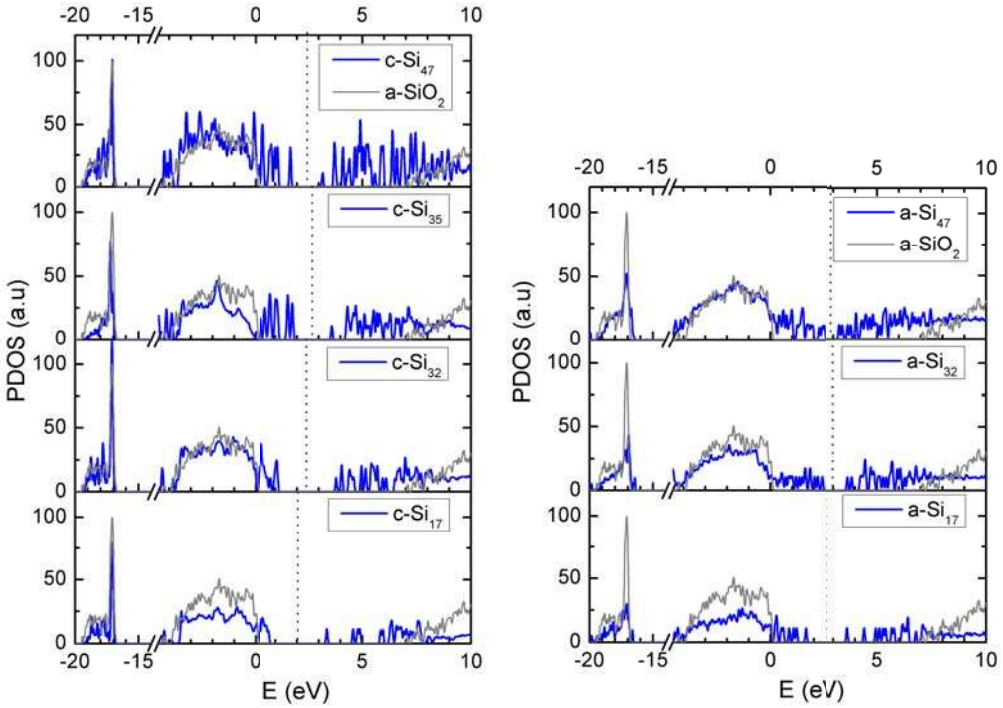

Figure 4.2: PDOS of the crystalline and amorphous Si QDs (blue line) compared to a-SiO_2 DOS (grey line). The valence band maximum of silica defines the zero energy in all the cases. The Fermi energy is located in the middle of the HOMO-LUMO band gap of the embedded systems (black dot line).

Among the electric properties of Si QDs, it is interesting to mention that the HOMO level is mainly localized at the interface while the LUMO extends over the entire QD region [75] and that amorphous systems present smaller E_g than crystalline systems of similar size (see Table 4.3), in accordance with photoluminescence measurements where the energy gap for QDs around 2.5 nm in diameter was determined to be 1.9 eV for amorphous QDs [171] and 2.7 eV for crystalline ones [172].

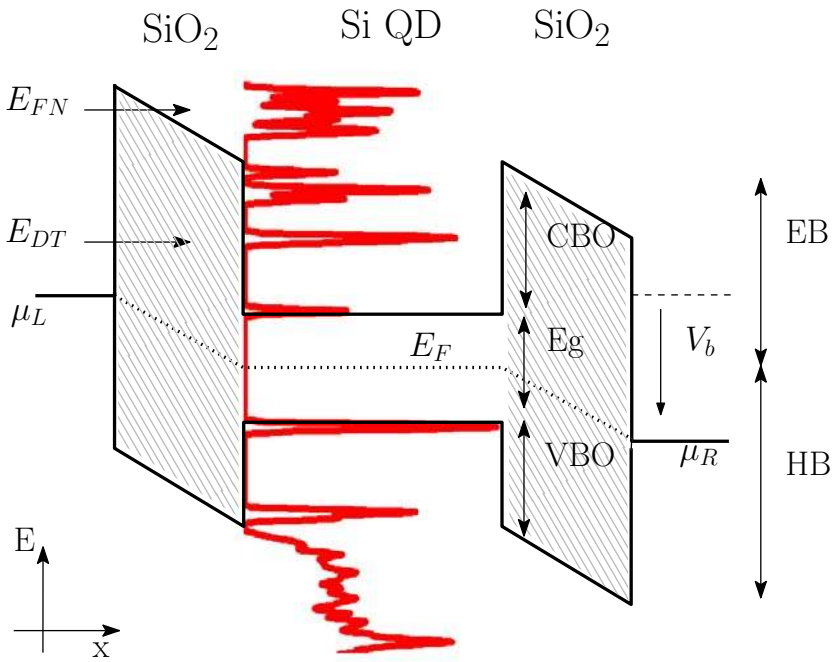

Figure 4.3: Band diagram (solid black lines) of the system, DOS of the Si QD (solid red line), and Fermi energy E_F (dotted black line) when a bias voltage V_b is applied. The conduction and valence band offset (CBO and VBO) are the difference between the conduction and valence SiO_2 band edge and half the embedded system energy gap E_g, while the electron (hole) barrier EB (HB) is the conduction (valence) SiO_2 band edge with respect to E_F of the embedded system. The two possible tunnel mechanisms are shown: Fowler-Nordheim (FN) and direct tunnel (DT).

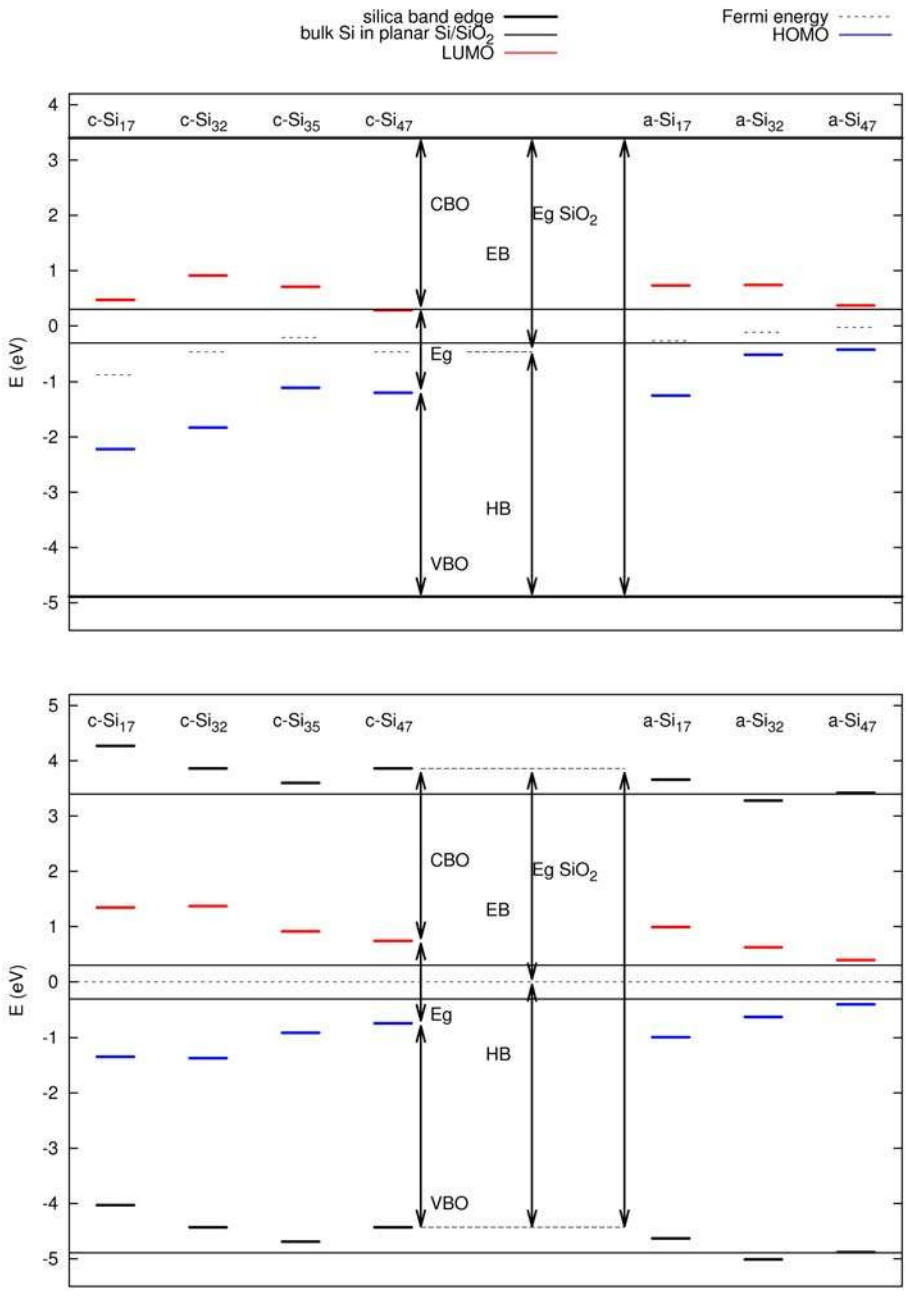

Figure 4.4: Energy band profile of the QDs (HOMO in blue lines and LUMO in red lines): (top) with respect to the same silica band edges (solid black lines), and (bottom) with respect to the same Fermi energy E_F (black dot line). The value for bulk Si in planar Si/SiO_2 interface (thin black lines) with the same computational parameters used in this work is shown for comparison.

4.3.1 Band offset

One of the parameters to give to SIMQdot code is the potential well created by the SiO_2 matrix surrounding the QD. Fig. 4.3 shows the definitions used in this PhD thesis: the Fermi energy E_F of the whole system is taken as the zero of energies and is located in the middle of the HOMO-LUMO band gap of the QD (E_g). Then, by aligning the Si QD PDOS using the strong peak of a-SiO_2 DOS as reference, present at about -17 eV in all the studied structures (see Fig. 4.2), we can give a value for the conduction (valence) band edge of the silica in the embedded systems, namely electron (hole) barrier EB (HB). The energy difference between the conduction (valence) band edge of the SiO_2 matrix and the LUMO (HOMO) level of the Si QD gives the conduction (valence) band offset, CBO (VBO).

As can be seen in Fig. 4.4, the interface between Si QD and SiO_2 forms a type-I heterojunction (i.e. a straddling gap, differently from a staggered gap, type II, or a broken gap, type III) like the interface between these two materials in bulk planar systems. However, as quantum confinement, oxidation, and stress influence the energy gap of the Si QD, it is natural to think that the potential barrier produced by the dielectric matrix may also have a dependence with Si QD size.

The main electrical features of Si QDs with size and amorphization level are:

1. E_g decreases with Si QD size, with oscillations due to oxidation state. E_g is smaller for amorphous systems.

2. Band offset increases with the QD size (more pronounced for valence band, VB, than for conduction band, CB), consistently with the planar value corresponding to very large diameter.

3. The number of states increase with Si QD size.

4. HB and EB collect the contrary dependence of E_g and band offsets with Si QD size. EB and HB have contrary tendency with Si QD size, while the former decreases, the latter increases with size, both up to planar value.

5. Crystalline VBOs are lower than the amorphous counterparts for QDs of similar diameter.

The first one implies reduction of the current for large Si QDs, while the second and third ones implies enhancement of the current: while larger band offsets give lower transmission probability, E_g determines the conductivity threshold. Thus, large QDs have high barriers (i.e. low transmission probability), but at high V_b they might present higher currents, as a large number of states enters the conduction window (i.e. the energy range between μ_L and μ_R) and are available to the carriers.
Li et al. [178] explained the different behavior of CB and VB by analyzing the spatial distribution of the HOMO and LUMO states, and they justified the sensitivity of the HOMO state to the surrounding matrix by considering its localization at the QD interface. Conversely, since the LUMO state extends over the whole QD, differences in the surrounding matrix have negligible effects on it.

4.3.2 Correction of the barriers values

It is well known that Kohn-Sham eigenvalues give an underestimated E_g that can be corrected by solving the quasiparticle equation within the GW approximation [179–181]. However, while the latter correction is noticeable in bulk materials (i.e. Si, SiO_2), in strongly confined systems the enhanced excitonic interaction is known to reduce E_g of about the same amount. As a consequence, the E_g of QDs computed by DFT-LDA is, at the end, similar to those obtained by more sophisticated many-body methods [75, 182] (see Table 4.2 for a comparison).

E_g (eV)	experimental	DFT LDA-LCAO	DFT LDA-PW	corrections to DFT-LDA-PW
bulk Si	1.1	0.6	0.51 [183]	1.08 [183]
bulk a-SiO_2	9.0 [184]	7.1	5.6 [180]	10.1 [180]
Si QD ($d \sim 1.6\,\mathrm{nm}$)	1.9 [73]	1.5	1.81 [185]	1.86 [185]

Table 4.2: Comparison of the energy gap E_g of bulk Si, bulk SiO_2 and a Si QD between experimental data, present DFT results with LCAO basis, and corrections to DFT computations found in literature. It is worth noting that the correction to DFT calculations has to be done with PW basis results.

Moreover, it has been shown through the Bruggeman effective medium approximation that the dielectric function of the SiO_2 embedded matrix is

independent and decoupled from the states of the subsystem formed by the Si atoms of the QD and the O atoms of the interface [77].
For the above reasons, in the case of small embedded QDs, one deals with "correct" E_g values (determined by QD states), but "uncorrect" band offsets due to the systematic error in the SiO_2-related energy values. In the case of a Si/SiO_2 slab calculation in the bulk limit, we have obtained VBO and CBO of 2.6 eV and 3.9 eV, respectively, to be compared with the experimental values of 4.6 eV (VBO) and 3.1 eV (CBO) [186]. Thus, we have applied a constant correction of 2.0 eV to VBO and HB values, and of -0.8 eV to CBO and EB values and not to E_g (Table 4.3). As our QD size range is small, we used the same energy shift for all the data.

	d (nm)	E_g (eV)	CBO (eV)	VBO (eV)	EB (eV)	HB (eV)
c-Si_{10}	0.99	2.02	2.47	3.80	3.48	4.81
c-Si_{17}	1.25	2.68	2.93	2.68	4.27	4.02
c-Si_{32}	1.49	2.74	2.49	3.06	3.86	4.43
c-Si_{35}	1.38	1.82	2.69	3.78	3.60	4.69
c-Si_{47}	1.59	1.48	3.12	3.69	3.86	4.43
a-Si_{10}	1.04	1.46	2.67	4.16	3.40	4.89
a-Si_{17}	1.23	1.98	2.67	3.64	3.66	4.63
a-Si_{32}	1.42	1.24	2.66	4.39	3.28	5.01
a-Si_{35}	1.45	0.50	3.11	4.68	3.36	4.93
a-Si_{47}	1.58	0.78	3.02	4.49	3.41	4.88

Table 4.3: Corrected conduction and valence band offsets (CBO and VBO) of QDs with respect to electron (EB) and hole (HB) barrier, QD band gaps (E_g), and Si QD diameters (d) of each system.

4.3.3 An empiric expression for the band edges of Si QD in SiO_2 crystalline matrix

As has already been explained in previous sections, hydrogenated Si QDs are correctly described by the particle-in-a-box model, where the box size is given by the QD diameter and the potential barrier represents the embedding dielectric matrix. Such approach leads to a $1/d^{\alpha}$ relationship between the energy gap E_g and diameter d, with $\alpha \leq 2$ [75].

However, as can be seen in Fig. 4.5 and has been shown in previous works [47, 187], the presence of the silica matrix deviates this relationship from the pure quantum confinement effect, and modulates it by the oxidation state of the Si QD.
As an extension of Guerra's work [187], which includes a fit for -H and -OH terminated Si QDs computed with PW basis set, we present an empiric expression for the present embedded crystalline Si QDs computed with LCAO basis set.

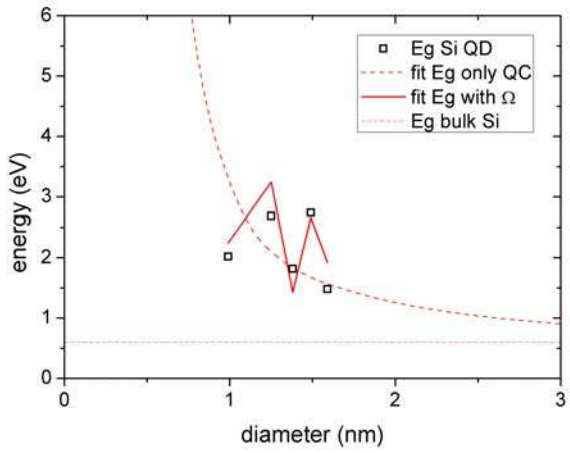

Figure 4.5: Fit of the E_g taking into account only quantum confinement (dashed line) and with the inclusion of oxidation Ω (solid line).

The relationship for the present embedded Si QDs between E_g and d in the particle-in-a-box model is (for energies in eV and diameters in nm):

$$E_g(d) = 0.6 + 2.2\frac{1}{d^{1.8}} \tag{4.3}$$

while, by including the correction due to the oxidation state it is:

$$E_g(d, \Omega) = 0.6 + \frac{1.4}{d} + \frac{1.2}{d^2}(\Omega - 1.41). \tag{4.4}$$

The oxidation term is negligible for Si QDs with a diameter larger than 3 nm, where E_g is only related to quantum confinement [188]. It is worth noting that Ω tends to $\sqrt{2}$ for large diameters in randomly generated Si QDs [187] and that the discrete effect of Ω produces a sharped curve with d.

The value of E_g for bulk Si, first term of E_g fit (Eq. 4.4), is dependent on the basis set used in the calculation. The difference in the other two terms is related to the strain induced by the matrix, not present in the -OH terminated Si QDs.

Besides, the electron and hole barriers are also important parameters in transport calculations. Thus, we also present an empiric estimation for the band offsets (Eq. 4.5) and the potential barriers (Eq. 4.6) in Fig. 4.6:

$$\begin{cases} CBO(d) = 3.1 - \dfrac{0.6}{d^2} \\ VBO(d,\Omega) = 4.6 - \dfrac{1.2}{d} - \dfrac{1.0}{d^2}(\Omega - 1.41) \end{cases} \tag{4.5}$$

where, because of the small dependence of the CBO with the Si QD size, the correction due to the oxidation degree was not included.

The final fit for the oxide barriers is the sum of half of the band gap and the band offset:

$$\begin{cases} EB(d,\Omega) = \dfrac{E_g}{2}(d,\Omega) + CBO(d) = 3.4 + \dfrac{0.7}{d} + \dfrac{0.6}{d^2}\left[(\Omega - 1.41) - 1\right] \\ HB(d,\Omega) = \dfrac{E_g}{2}(d,\Omega) + VBO(d,\Omega) = 4.9 - \dfrac{0.5}{d} - \dfrac{0.4}{d^2}(\Omega - 1.41) \end{cases} \tag{4.6}$$

Validation of the computational estimation with experiments

Seguini and coworkers [189] experimentally extrapolated the barriers of Si QDs embedding in SiO_2 matrix with diameter range 1.9-4.3 nm. From photoionization measurements they evaluated the energy difference between the VB of the Si QD and the CB of the SiO_2, corresponding to our $E_g + CBO$ values. As a comparison, their smallest QD of $d = 1.9$ nm have a $Eg + CBO = 4.65$ eV, while our largest Si QD with $d = 1.6$ nm has a $Eg + CBO = 4.6$ eV.
The energy range for this quantity, calculated from our fit for different oxidation degree of a QD with $d = 1.9$ nm, would be from 4.8 eV ($\Omega = 3$) to 4.13 eV ($\Omega = 1$). The exact oxidation value to reproduce the experimental value of $Eg + CBO = 4.65$ eV with our fit is $\Omega = 2.55$. However, it is higher than the

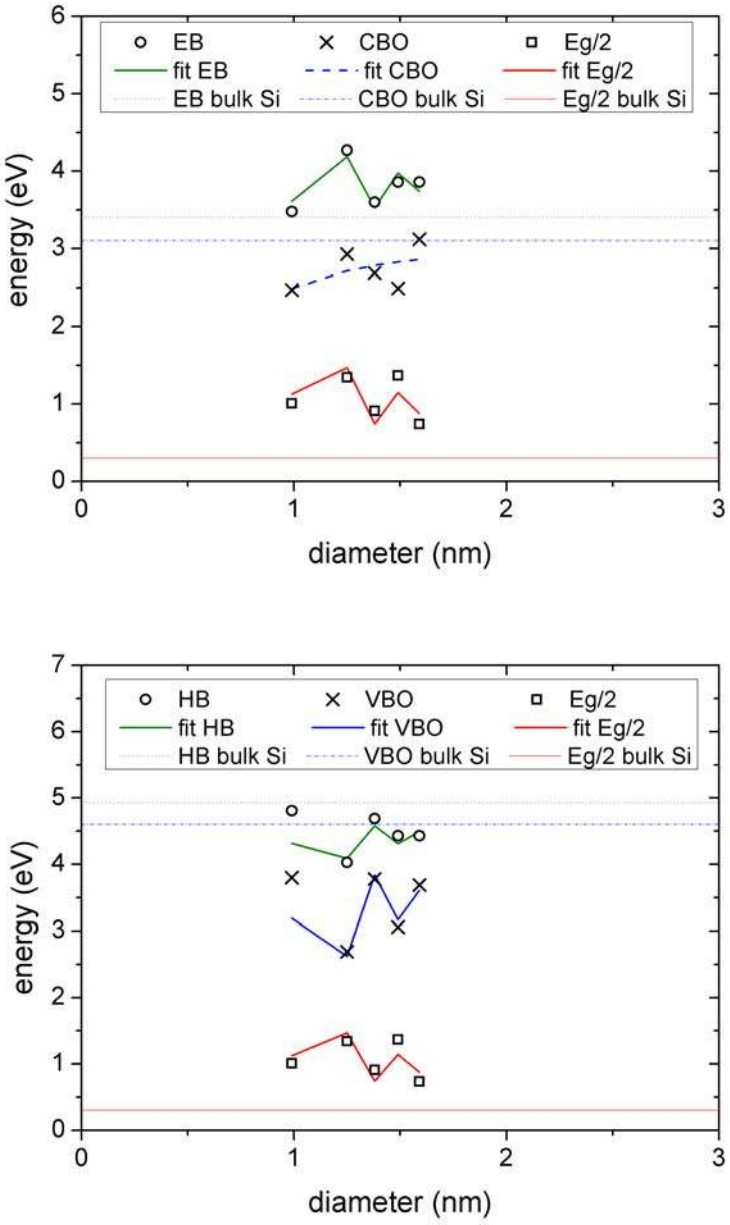

Figure 4.6: (up) Fit of the E_g, CBO, and EB, and (down) Fit of the E_g, VBO, and HB.

maximum Ω value extracted from $\Omega(d)$ fit of Guerra's work (Ω would be in between 1.20 and 1.81 for a Si QD with $d = 1.9\,\text{nm}$). Therefore, using the maximum Ω value allowed for the diameters of Seguini's work, the values extracted from our fit are between 5 % and 10 % smaller than experimental ones.

4.4 Electronic transport

The current-voltage I-V characteristics were computed through TH method with SIMQdot code for all crystalline and amorphous systems. As mentioned in Section 4.2, the electron transport results for the QDs of 10 atoms (they only have interface Si atoms inside the QD) and for a-Si_{35} (it has defects after relaxation) are not reported in the following section, because the other systems have interface and core states mixed in the transport properties and they are defect-free.
The DFT-calculated equilibrium properties provided to SIMQdot for each system were the PDOS (energy shifted in order to have the Fermi energy of the system as the zero of energy scale), the values of the oxide barriers EB and HB extracted as explained in Section 4.3.1, and the value of the Si QD radius (r_{QD}) calculated from Eq. 4.1.

4.4.1 *I-V* characteristics

The discrete nature of the QD states and the quasi-continuous DOS of interface atoms are directly reflected on the current (see Fig. 4.7). A peak in the current appears whenever an energy level of the QD enters the conduction window.
The first peak in the I-V characteristic marks the threshold voltage above which carriers can tunnel inside the dot, related to the fundamental energy gap E_g of the system. In our particular case, this peak occurs at a V_b nearly twice the energy of the corresponding peak in the DOS. This is related to the fact that the Laplace solution U_L of one QD and equal capacitance couplings for both electrodes is $U_L = -qV_b/2$, and, since the Poisson term is small, the potential V inside the QD becomes nearly half the bias voltage V_b [33] (see Section 2.3.3 for more details on the equations).
The regions in which the current decreases with the voltage, known as negative differential resistance (NDR), appear because the potential well of the

QD is modified by the external V_b. Thus, as V_b increases, the charge accumulated in a conductive energy level decreases, since the ratio between the incoming and outcoming transmission coefficient decreases with V_b [37]. NDR is hardly noticeable in the largest QD due to a reduced presence of isolated peaks in the DOS.

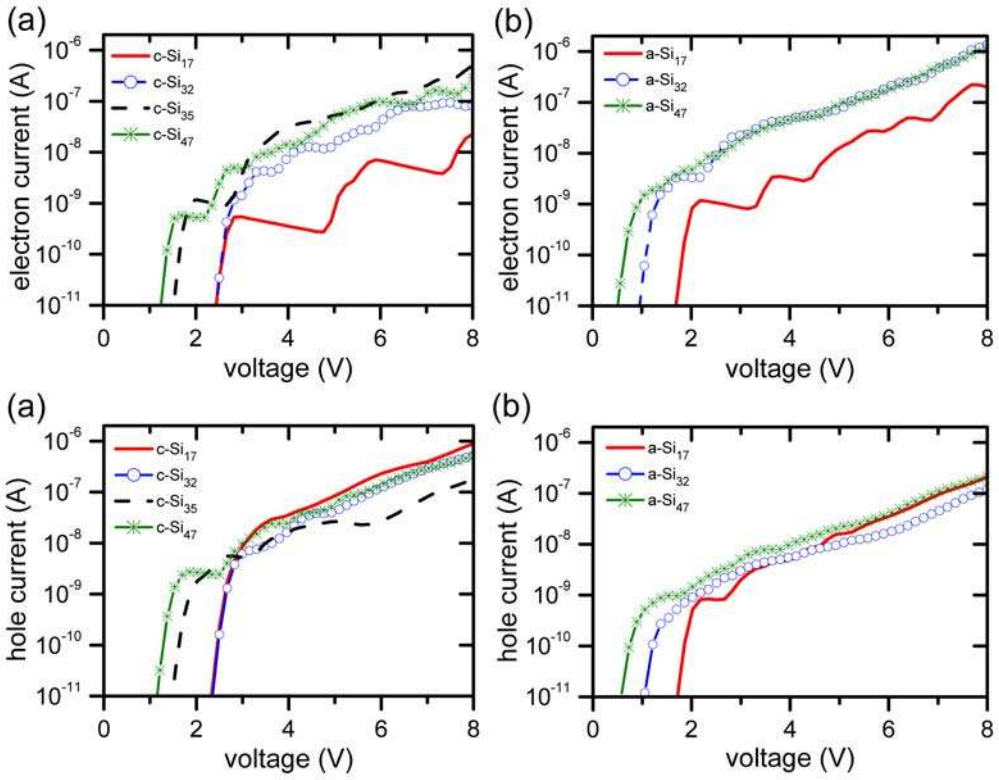

Figure 4.7: (top) Electron I-V characteristic for a) crystalline systems, and b) amorphous systems. (bottom) Hole I-V characteristic for a) crystalline systems, and b) amorphous systems.

4.4.2 Dependence with size and amorphization level

A direct correlation is found between EB (HB) and electron (hole) conductance in the high bias voltage, being larger for those systems with a smaller potential barrier. In particular, electron transport is favored for big systems while hole transport is enhanced in the small QDs.
CBO does not vary substantially in our systems, and therefore electron current is primarily determined by E_g and by the position and number of the

QD states (see Fig. 4.7). Thus, since the smallest QDs (c-Si_{17} and a-Si_{17}) present the highest E_g and the smallest DOS, they produce the lowest electron currents. For the same reason, we observe a clear trend of increasing electron current with the QD size, although the range of diameters presented in this PhD Thesis is quite limited to permit visible differences between the largest QDs, especially in the case of amorphous structures.
Besides, for QDs with similar E_g values, like c-Si_{32} and c-Si_{17}, the largest current is achieved by the one with the smallest CBO, as expected.
On the other hand, hole transport radically differs from electron transport. The extremal decrease of VBO for the smallest systems, c-Si_{17} and a-Si_{17}, rules over their large E_g, and, although the larger V_b threshold with respect to the other systems, the low hole barriers enhance the hole transport in these small systems. However, for the other structures, the influence of VBO and E_g are mixed, being the value of HB the parameter that have a direct correlation with hole current values.
Systems that have different VBO and E_g, like c-Si_{32} and c-Si_{47} or a-Si_{17} and a-Si_{47}, have a similar current for high bias voltages due to their similar HB values. This is clearly visible for the c-Si_{47}, that is the first system to show current among crystalline cases, and has a rather larger VBO than (for example) c-Si_{32}. Therefore, when V_b approaches the threshold value of the other systems, the c-Si_{47} current is supported by several states inside the conduction window, and the final currents become comparable.
In conclusion we can expect, *a priori*, from the tendency of HB to increase with Si QD size up to the theoretical value (see the bottom of Fig. 4.4), a decrease of hole current in large systems. However, we suspect that in real big systems the strong DOS and small E_g may possibly overcome the effect of the low HB in small QD. This point should be furtherly investigated in the future, when the present computational limits for these systems will be overcome.
Referring to the morphology of the material (Fig. 4.8), the tendency of amorphization to reduce E_g and similar CBO between crystalline and amorphous systems produce higher electron currents for amorphous systems. From the other side, the reduced VBO in the crystalline QDs give HB smaller than their amorphous counterparts despite their higher E_g, favoring the hole transport in the crystalline systems.

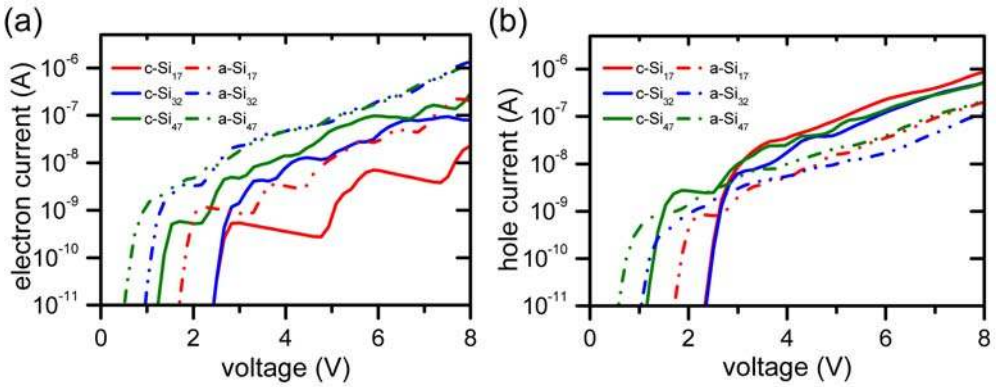

Figure 4.8: Comparison of a) electron and b) hole transport for crystalline and amorphous systems.

4.5 Conclusions

We have investigated, for the first time, the dependence of electron and hole transport on the size and crystallinity of embedded Si QDs using DFT calculations for the DOS, a TH approach for the expression of the current, and a WKB approximation for the expressions of the transmission coefficients. Intrinsic Si QDs were covered in this section, while the extrinsic properties have been described in the following Section 5.

4.5.1 Electronic transport through a single Si QD

The main conclusions for electronic transport in embedded Si QDs extracted from the present study of their DFT ground state properties are:

1. Similarly to the dependence between Si QD band gap and size, there is also a relationship of Si QD size and energy band offsets between Si QD and embedded SiO_2 matrix. We found that, in most of the works found in literature [73,186,190,191], it is not taken into account in the general description of transport through embedded Si QDs, where these band offsets are always taken as the one for bulk Si/SiO_2 interface. This trend has been previously reported by theoretical studies [77,178,192,193] and supported by soft X-ray spectroscopy [194] and photo-ionization and capacitante spectroscopy measurements [189, 195] of small embedded SiQDs.

2. Electronic transport is determined by a balance between transmission

probability (dependent on the silica barrier height or band offset), available states inside the silica barrier (related to the QD DOS), and conduction gap (dependent on the embedded system energy gap E_g). Generally speaking, when the QD diameter increases, the VBO increases (CBO has a weaker dependence) while E_g decreases. Besides, the number of states inside the barrier increases with the QD size. Thus, when the diameter increases, the higher DOS and lower E_g enhances the current, whereas the higher band offset reduces it. Since EB and HB gather the opposite trend of band offset and E_g with the QD size, we propose to use them as a single parameter to characterize the electronic transport.

3. A correlation between electron (hole) conductance and EB (HB) is found, being the large (small) system and the amorphous (crystalline) counterparts better for electron (hole) transport:

   (a) Electron transport is enhanced in big systems due to the larger DOS and because CBO does not vary significantly. Therefore EB follows E_g, being lower for bigger systems. Conversely, hole transport is enhanced in the smallest systems because of the reduced VBO. However, the result of the largest Si QD of this study may reveal a change in the latest trend of HB to decrease with size: we don't have enough data to ensure that, at a certain size, the small E_g and the big amount of available states of bigger systems will not overcome the effect of a large HB.

   (b) Concerning the systems structure, amorphous QDs present higher electron current than crystalline ones for a given QD size due to their smaller E_g. Hole transport, however, is enhanced for crystalline systems due to the much smaller HB, supporting the idea of an efficient electron confinement in crystalline QDs.

In conclusion, our calculations show that the transport properties of small Si/SiO_2 QDs are extremely sensitive to the microstructure of the QD/SiO_2 interface. In practice, this means that the design and fabrication of devices based on small QD with predictable properties requires a fine control of these properties that go far beyond the mere control of the QD diameter.

4.5.2 DFT-TH methodology to study transport in nanostructures

One of the main objective of this study was to set the procedure of using DFT properties inside TH formalism using its implementation in SIMQdot code created by S. Illera. Up to our knowledge, the methodology present in this PhD Thesis is the first attempt to the use of DFT characteristics for the study of electronic transport through embedded Si QDs.
Contrary to DFT-NEGFF procedure, the most complex and time-demanding task in the present methodology lays on the description of the models by DFT: once the structure is relaxed and the electronic ground states properties are computed by DFT, the computation of the I-V characteristic by TH method is straightforward. However, the direct extrapolation of the transport properties for *any* QD size is not direct, due to the specific DFT characteristics for a given atomistic configuration of the QD, different from other analitical descriptions such as the solution of the particle-in-a-box model.

Concerning the influence of the TH parameters inside SIMQdot, we have seen that:

1. For a given thickness of surrounding silica, the election of the electron and hole barriers is the main parameter in the final current value.

2. The other parameters of the transport computation through a single QD, such as dielectric carriers effective masses or QD radius, have less influence.

3. For a given set of parameters for a system formed by a QD surrounded by a dielectric matrix, i.e. QD radius and DOS, and dielectric barriers and effective masses, the variation of the thickness of the surrounding silica has an extreme influence on the absolute value of the current, due to the exponentially dependence in the transmission coefficient.

4. In turn, the capacitive coupling between the electrodes and the QD, modeled by the analytical expression of the capacity between an infinite plane and a sphere representing the QD [35], has a lower variation with respect to the change in the matrix thickness.

As an example, by varying 0.4 nm the thickness of the SiO_2 matrix, the total current through the Si QD decreases two orders of magnitude, while the

capacity coupling between the Si QD and the leads has a reduction of about a 5%.

Chapter 5

Doped silicon quantum dots embedded in a SiO_2 matrix

After analyzing the effects of the morphology of intrinsic Si QDs on the transport properties, the influence of extrinsic properties has also been studied. These extrinsic properties, that can be controlled by technological processes, are particularly interesting. In particular, doped Si QDs have already been achieved [3, 53–56], but several aspects are still unclear: the precise position of the dopant atoms inside the device, whether directly doping the nanostructures is desirable to increase conductivity and effectively separate the carriers or not, etc.
Therefore, in this section we analized the consequences of doping the embedded Si QDs systems studied in the previous section. We started with the morphological distortion induced by the impurity, then, we moved to the formation energy for the different impurity positions, and, finally, we focused on the change in electronic states, and their influence on I-V characteristic. When possible, the results of this work are compared with previous doping studies of free-standing Si QDs [57, 64, 65, 67, 196–198].

5.1 Computational details

We used the same computational parameters than the previous calculations of the undoped systems (Section 4.1), but with a spin polarized basis set (at $T = 300\,K$) as doped Si QDs have an odd number of electrons.
As for undoped Si QDs, the projected density of states (PDOS) used in

transport calculations was the one corresponding to the subsystem formed by the Si atoms of the QD and the first shell of O atoms at the interface between the QD and the SiO_2 matrix, and it was also shifted until E_F was set to zero for all the calculations. However, in the results presented in this chapter, the value for E_F is the one directly extracted from the DFT calculation [199].

5.1.1 On the complexity of the systems

The inclusion of two possible impurity species in different positions, increases the Si QD set of the previous Chapter into a large quantity of possible systems to study: around ten for each previous QD. Moreover, their complexity leads to near two thousand relaxations steps and at least six months of full-time computing in a 32-core machine per system.
We focused only in crystalline systems and, therefore, we present in this PhD Thesis the study of three representative cases relaxed until forces in all the atoms were less than 0.04 eV/Ang, as in the previous section. However, one will note an energy discrepancy in formation energies of Section 5.2.2. This is because of the existance of a relative energy minima in the relaxation process of the systems. At a force point of 0.04 eV/Å, most of the systems are at a local energy minimum, while two of them have already reached the absolute one. That leads to a difference of several eV between the formation energy of those systems (see Fig. 5.4). However, preliminary results show that, by continuing the relaxation until the forces are below 0.01 eV/Å in all the atoms, all the systems will relax to their corresponding absolute minimum, keeping the order on the formation energies. These new calculations are on-going at the time of writing this PhD Thesis. We believe, that these calculations will refine the results present of this PhD Thesis (only changing the value of the formation energy and having a uniform energy range for all the systems), but without significant changes in the electronic and transport properties described in this work.

5.2 Description of the systems

Three different crystalline systems, c-Si_{32}, c-Si_{35}, and c-Si_{47}, were studied with three possible substitutional positions of the impurity atom, B as an acceptor and P as a donor, (see Fig. 5.1): inside the dot, at the interface

(it could be bonded to one, two, or three O atoms), and in the SiO_2 matrix far away from the QD, thereafter named "dot", "int-1", "int-2", "int-3" (depending on the number of O atoms bonded to the impurity) and "silica", respectively. Note that not all the Si QDs sizes can show the same kind of interface atoms.

5.2.1 Morphological features

In previous works, structural features were studied in free-standing hydrogenated Si QDs for the impurity located at the center of the QD [65,67,196]. For B-doped systems, their symmetry is lowered from T_d, tetrahedral configuration with similar length for all the bonds, to C_{3v}, where one bond length is larger than the other three [65,67] (see the variation in symmetry of B-dot systems with QD size in Fig. 5.2). As structural distortion is nearly independent of size in B-doped samples [196], this feature is found in all the systems. On the other hand, structural distortion is strongly dependent on Si QD size in P-doped samples, decreasing for large QDs [196].

In the present embedded Si QDs, the broken symmetry found in B-doped free-standing Si QDs is clearly visible in the smallest systems, i.e. c-Si_{32}, when B impurity is inside the dot and at the interface, and also when P atom is inside the dot. However, the deformation of the system decreases with increasing QD size, recovering the T_d symmetry for all the systems except for B-int-2 and B-int-3.
There is a general trend to decrease the Si-X bond length, being X the impurity atom, as Si QD size decreases, both in free-standing and in all embedded cases (see the variation in impurity bond lengths in doped systems with respect to the substituted Si bond length in undoped systems in Fig. 5.3. In free-standing Si QDs, specially for small sizes, the Si-X bond length is usually longer (smaller) than the Si-X bond length in doped bulk Si, for those impurities with similar or larger (shorter) covalent radius than Si, such as P (B) [67]. However, for embedded Si QDs, the Si-X bond lengths are always larger than in doped bulk Si, although there is a clear tendency with dot size to recover the bonds of doped bulk Si, 2.05Å for Si-B and 2.33Å for Si-P. On the other hand, the Si QD also influences on the impurity atom when it is in the silica, specially in P doping (there is a compression of the O-P bond instead of the enlargement found in doped bulk silica).
Similarly than in free-standing systems, while P impurity tends to slightly

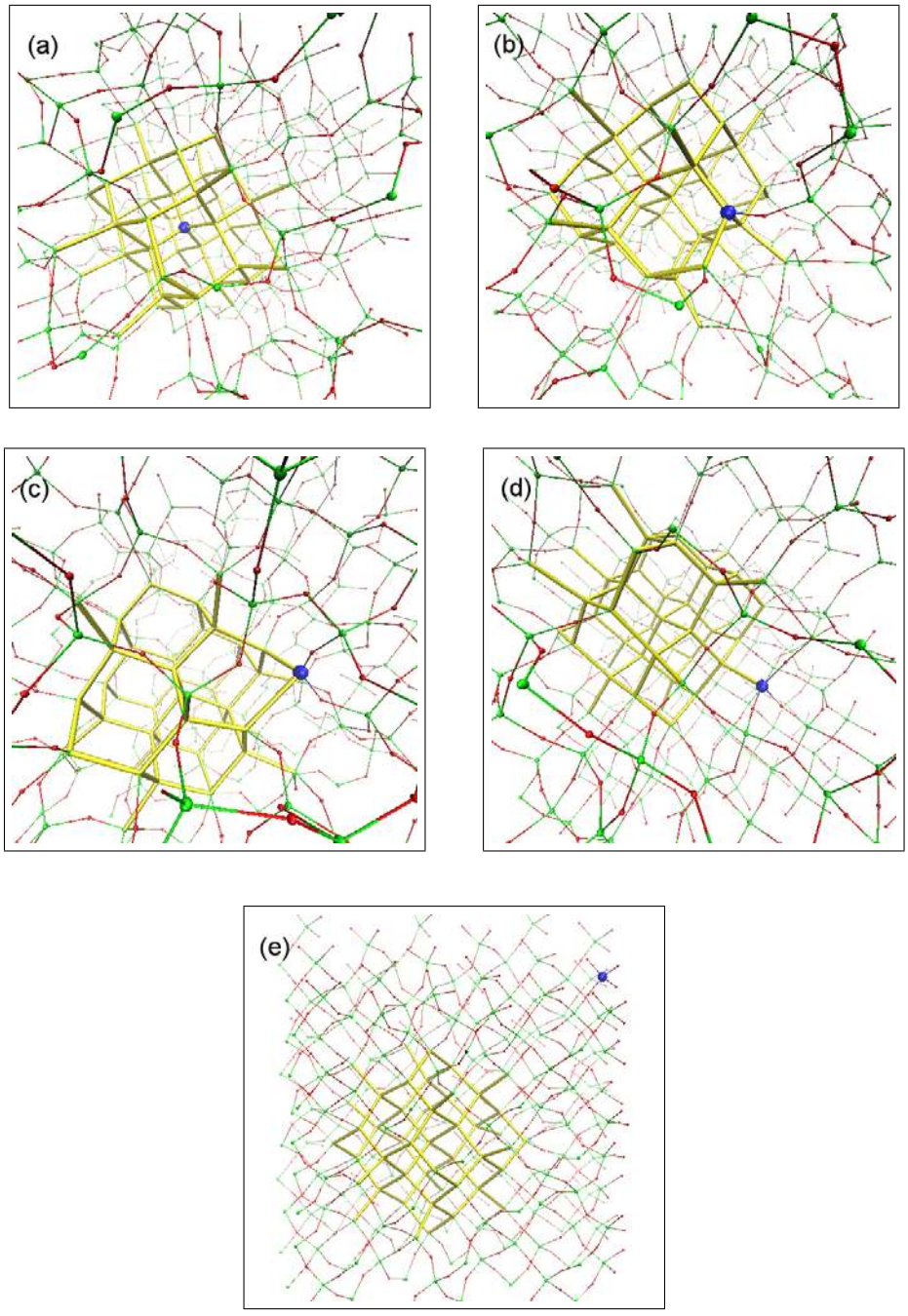

Figure 5.1: Atomic model for the different impurity position (in order): (a) inside the dot ("dot"), at the interface between the dot and the first shell of O atoms bonded to (b) one ("int-1"), (c) two ("int-2"), or (d) three ("int-3") O atoms, and (e) in the SiO_2 matrix surrounding the Si QD ("silica"). Red spheres are O atoms, green spheres are Si atoms, blue sphere is B atom, and the yellow thick sticks represent the Si atoms of the QD

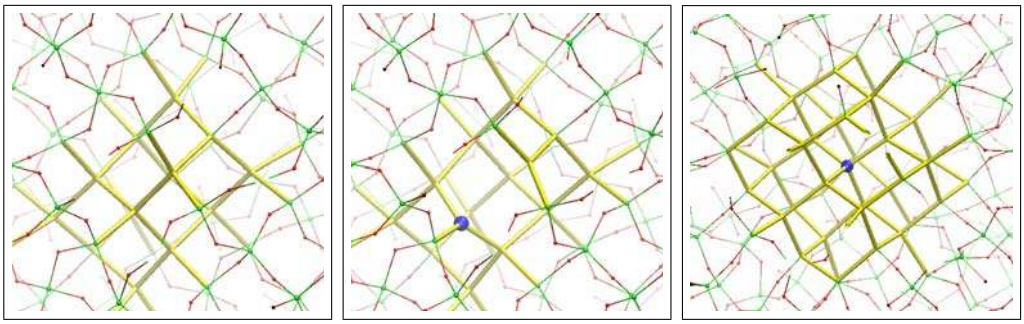

Figure 5.2: Change in symmetry for B-doped systems: from (left) undoped with T_d symmetry to (center) c-Si_{32} with C_{3v} symmetry and (right) c-Si_{47} with a T_d symmetry again. Red spheres are O atoms, green spheres are Si atoms, blue sphere is B atom, and the yellow thick sticks represent the Si atoms of the QD

enlarge the bond with Si atom with respect to undoped systems, B atom tends to compress it. Moreover, for a given impurity position and Si QD size, the B-doped systems have more deformation than P-doped systems, in terms of variation of bond lengths and also of compression of cell volume, in accordance with free-standing QDs, where Si-B bonds are around 2 Å while Si-P bonds are around 2.3-2.4 Å [197].

5.2.2 Formation energy

The formation energy Ω_f in Fig. 5.4 was calculated following Ossicini *et. al.* [58]

$$\Omega_f = E_{doped} - E_{undoped} + E_{Si} - E_{dopant}, \tag{5.1}$$

where $E_{undoped}$ and E_{doped} are the total energy of the undoped and doped systems, respectively, and E_{dopant} and E_{Si} are the total energy per atom in a bulk configuration for a dopant atom, B or P in each case, and Si, respectively. Specificaly, the bulk systems for the dopant atoms are the ones commonly used for formation energy calculations: for B atom we used the B_{50} system [200], an alpha-tetragonal phase with IT number 134, space group P42/nnm, a=b=8.75 Å, c=5.06 Å, and angles of 90°; and for P atom we used the black P system, an orthorombic phase [201], with IT number 64, space group Cmca, a=3.314 Å, b=10.478 Å, c=4.376 Å, and angles of 90°.

In the case of free-standing hydrogenated Si QDs, sites near the QD surface appear to be energetically more favorable because the relaxation around the

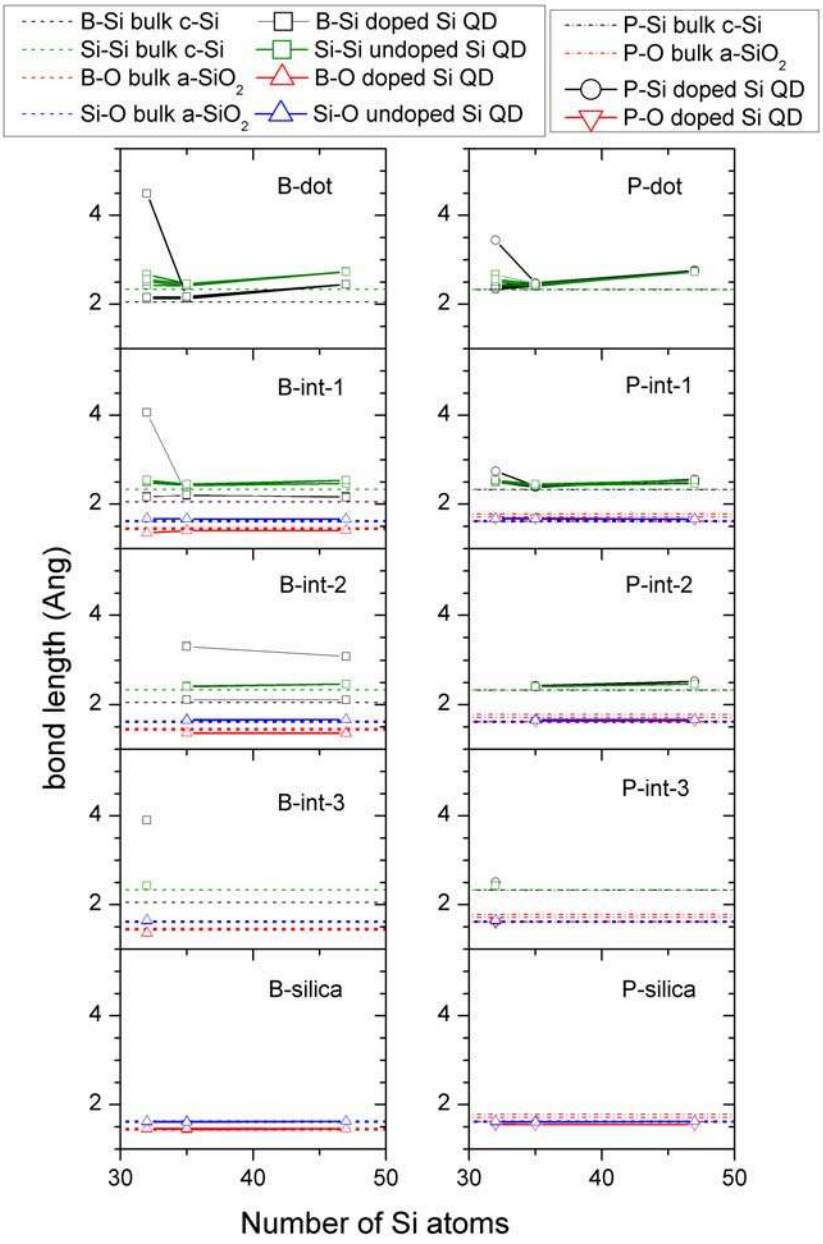

Figure 5.3: Comparison between the Si-X bond lengths, X being B, P, or Si, of the doped systems with respect to undoped ones (symbols). Bulk calculations for doped and undoped crystalline Si (c-Si) and amorphous SiO_2 (a-SiO_2) are shown for comparison (dashed lines).

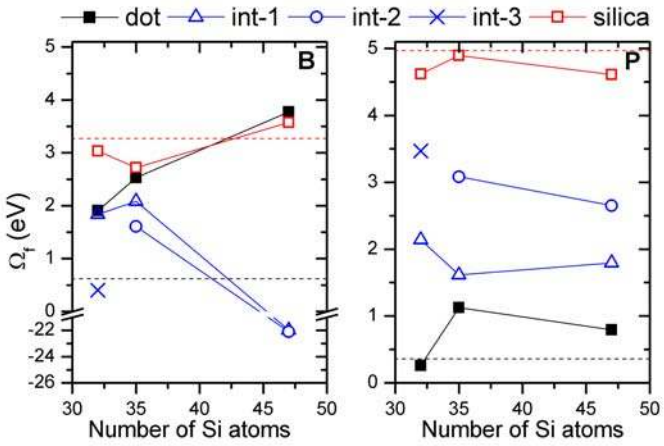

Figure 5.4: Influence of QD size on the formation energy Ω_f for different position of the impurity atom: inside the dot (black squares), at the interface (bonded to 1 O atom, blue triangle, bonded to 2 O atoms, blue circle, bonded to 3 O atoms, blue cross), and in silica (red square). The value for Ω_f of the impurity in bulk silicon (dotted black line) and bulk silica (dotted red line) is shown for comparison.
Note the difference in energy range of B-int systems of c-Si_{47} with respect to the other systems. This happens because the systems are in two different energy minima. Further calculations which will lead to the same energy range for all the systems are on-going and preliminary results confirmed the same ordering of the total energy present here (see Section 5.1.1).

impurity is easier in this situation [57, 58, 64, 65, 198]. This is used as an argument to explain some experiments where doping the nanostructures is more difficult than doping the corresponding bulk material [64]. Moreover, this configuration seems to be the preferred one in free-standing Si QD experimental studies [202, 203]. In the case of embedded Si QDs, see Fig. 5.4, doping inside the QD is also more difficult than doping bulk Si, while doping in the surrounding matrix is easier than bulk silica. However, while, for B-doping, the enegertically most favorable impurity position is also at the interface of embedded Si QDs, for P-doping systems, the preferred position is at the center of the QD, in accordance with other theoretical studies of embedded B-doped [204] and P-doped systems [205].
The evidences of B-O bond signal in x-ray photoelectron spectroscopy (XPS) spectra [56] and the suggestion of B-doped Si QDs with an intrinsic core and heavily B-doped shells in PL experiments [206] confirm the reliability of our calculations, i.e. B-doping the interface of embedded Si QDs.
It is worth to stress that P-doping is somehow controverted for the scientific community. In particular, there are some theoretical [57, 196, 198] and experimental studies [3, 10] that claim that it would not be possible to P-dope

the inside of a Si QD because Si QDs tend to expel impurity atoms towards the surface during growth (mechanism called self-purification) and because they have not found P atoms inside Si QDs [207]. Such huge differences in P-doped experimental results may be explained by big different techniques of creating the P-doped Si QDs and by difference concentration of doping. On one hand, Hao *et. al.* [3] show that for a very high P concentration there may be nucleation of P atoms at the interface, but, on the other hand, Cho *et. al.* [208] found that for a certain P concentration the P-O bond signal in XPS spectra is suppressed only finding P-Si bond signal. In fact, Gutsch et al. [209] specify the importance of the doping technique and they suggest that the most suitable to achieve P-doping inside Si QDs would be through high temperature solid-phase crystallization. Moreover, with this technique they are able to selectively dope either the QD precipitation layer or the dielectric matrix separation layer, being able to obtain all the impurity position combinations present in this study. In fact, there are clear evidences that, for Si QDs below 2 nm, the P atoms are likely to be doping the center of the embedded Si QD [60].

Thus, the difference with free-standing QDs is suggested to be related to the presence of a SiO_2 layer: (1) the energy necessary to form P-Si bonds in the place of Si-Si bonds is smaller than the energy necessary to form P-O bonds instead of Si-O bonds [205] (see the large energy difference between P-doping bulk a-SiO_2 and bulk Si in Fig. 5.4), (2) P atoms have been observed to segregate to Si-rich regions in recent experiments with embedded Si QDs [60], and (3) B-P codoped colloidal Si nanocrystals are composed by an outer B-rich shell and an inner P-rich shell due to the high difference between the segregation coefficient of B and P [210, 211].

For both kind of impurities, the location in the silica matrix is less favorable. Secondary ion mass spectroscopy (SIMS) experiments reveal that B or P diffusion from Si QD layers to adjacent SiO_2 layers can be neglected [3, 55].

5.3 Electrical structure

The inclusion of dopant atoms leads to a reduction of the embedded Si QD energy gap due to the appearance of discrete states inside the undoped-system energy gap. The energy position of these states and the atoms accountable

for them are different depending on the position and atomic specie of the impurity atom (Fig. 5.5, Fig. 5.6, and Fig. 5.7).
Table 5.1 summarizes the main electrical features of the doped Si QDs studied in this PhD Thesis. The energy gaps for the undoped systems are 2.74 eV for c-Si_{32}, 1.79 eV for c-Si_{35}, and 1.48 eV for c-Si_{47}.
Spin polarized calculations give separated information for electrons with up and down spins. The inclusion of the impurity leads to an odd number of electrons, making that, at T = 0 K, the polarization charge (difference between the charge of electrons with spin up and spin down Q_{up}-Q_{down}) is equal to one. However, for calculations at T = 300 K, this situation may change in some cases. In a general trend, as can be seen in Table 5.1, as the quantum confinement decreases for larger QDs, the difference between up and down states tends to go to zero, as has been already reported for free-standing Si QDs [67].

c-Si_{32}	B-dot	B-int-1	B-int-2	B-int-3	B-silica	P-dot	P-int-1	P-int-2	P-int-3	P-silica
CBM-L (eV)	1.16	0.86	—	0.65	0.20	0.54	0.19	—	0.17	-0.10
Eg (eV)	0.64	0.78	—	0.70	2.66	0.60	0.29	—	0.25	0.10
H-BVM (eV)	0.96	1.12	—	1.42	-0.10	1.63	2.28	—	2.34	2.76
Q_{up}-Q_{down}	1.00	1.00	—	1.00	0.38	1.00	1.00	—	1.00	0.76
ΔE_F (eV)	-0.10	+0.13	—	+0.39	-1.47	+0.54	+1.05	—	+1.08	+1.43
c-Si_{35}	B-dot	B-int-1	B-int-2	B-int-3	B-silica	P-dot	P-int-1	P-int-2	P-int-3	P-silica
CBM-L (eV)	-0.18	1.48	0.49	—	0.22	0.45	0.12	0.02	—	-0.19
Eg (eV)	1.94	0.13	0.50	—	1.74	0.00	0.00	0.00	—	0.00
H-BVM (eV)	0.03	0.18	0.81	—	-0.17	1.34	1.67	1.78	—	1.98
Q_{up}-Q_{down}	-0.01	0.84	0.98	—	-0.00	-0.02	0.00	-0.00	—	0.01
ΔE_F (eV)	-0.84	-0.65	+0.16	—	-1.05	+0.44	+0.77	+0.88	—	+1.09
c-Si_{47}	B-dot	B-int-1	B-int-2	B-int-3	B-silica	P-dot	P-int-1	P-int-2	P-int-3	P-silica
CBM-L (eV)	-0.19	0.95	0.17	—	+0.09	0.45	-0.04	0.01	—	-0.18
Eg (eV)	1.64	0.20	0.47	—	1.43	0.08	0.00	0.00	—	0.00
H-BVM (eV)	0.03	0.34	0.84	—	-0.03	0.95	1.53	1.48	—	1.67
Q_{up}-Q_{down}	-0.00	0.96	1.00	—	0.00	0.67	0.00	0.00	—	0.00
ΔE_F	-0.67	-0.31	+0.34	—	-0.73	+0.25	+0.78	+0.74	—	+0.92

Table 5.1: Energy difference between LUMO state (L) of the doped system and conduction band minimum (CBM) of the undoped system, HOMO-LUMO energy gap (Eg) of the doped system, difference between HOMO state (H) of the doped systems and valence band maximum (VBM) of the undoped systems (negative values correspond to states below VBM or above CBM of the undoped system, respectively), polarization charge (Q_{up}-Q_{down}), and displacement of the position of the Fermi energy with respect to undoped system ΔE_F.

As in the previous section, our "dot" systems can be compared with free-standing doped Si QDs [57,67,196]. From an electrical point of view, several

similarities are found: an increase of QC leads to deeper impurity levels and to energy differences between spin up and spin down energy levels. However, for free-standing Si QDs the impurity levels falling inside the gap are strongly localized at the impurity atom for all the sizes [197], while in embedded Si QDs the localization depend on the size: for the smallest Si QD these states are localized at the impurity atoms, either B or P, and for the other sizes, these states are partially localized in the P atom and the Si surrounding it in P-doped systems, and in the interface Si atoms of B-doped systems, but not in the impurity (see the PDOS profile for the impurity atom in Fig. 5.5, Fig. 5.6, and Fig. 5.7).

In a general view, the main electrical features for all the impurity positions can be summarized as:

1. The energy difference between levels with different spin is smaller as the size increases, approaching the limit case of doping bulk Si. The polarization charge, i.e. $Q_{up}-Q_{down}$, is one electron for all c-Si_{32} systems (except for B-silica). However, the tendency with QD size is to have polarization charge equal to zero (except for P-dot and B-int of c-Si_{47} system).

2. For P-doped systems, as the number of O bonds to P impurity increases (i.e. from "dot" to "silica" going through "int-1", "int-2", and "int-3"), E_F goes toward the CB, as one would expect for a n-doped material.

3. In B-doped systems, the E_F goes toward the VB, as one expect from a p-doped material, for all the systems except for "int-2" and "int-3", which create deep energy levels inside the band gap, preventing the E_F to move from the undoped position, or even going up in energy. Thus, the ordering of higher ΔE_F is "silica", "dot", and "int-1".

4. E_g decreases with doped Si QD size, until the limit of, eventually, $E_g = 0$ for those systems that at $\mathrm{T} = 0\,\mathrm{K}$ have a gap smaller than the temperature factor $k_B T$, being $\mathrm{T} = 300\,\mathrm{K}$ in the doping calculations. For a given size and impurity position, the E_g for P-doped systems is smaller than that of B-doped systems, in agreement with experiments [53] and being this difference a good quality in a p-n junction for solar cell applications [62].

5. B-dot shows a special tendency with size: H-BVM disminishes to almost zero for big systems, while L level goes inside CB, leading to an E_g higher than undoped system for big QDs.

A correlation between the change in Mulliken population of substituted atom (see the Appendix A for a complete set of tables with all the Mulliken populations of the systems) and shift of the Fermi energy can be done, having a higher ΔE_F when the difference in Mulliken charge between impurity atom and substituted Si atom is larger. In undoped embedded Si QDs the Mulliken charge of a Si atom depends on its position inside the system, changing from 4.2 inside the QD to 3.0 when it is at the surrounded silica. However, the Mulliken charge for the impurity atom is mostly independent from position and QD size, being around 3.2-3.3 for B atom and 4.9-5.1 for P atom. Thus, for P-doped systems, the difference in Mulliken charge increases as more O atoms are bonded to P atom, giving a Fermi energy deeper inside the CB. On the other hand, for B-doped systems, the Mulliken population of the impurity is similar to the one of Si atom in "int-2" or "int-3". The shift in E_F is then related to the change in Mulliken population from nearly no change ("int-2" and "int-1") to gain charge ("silica").

5.4 Electrical transport

The *I-V* characteristics were computed for all the systems using the PDOS previously computed with SIESTA code and TH formalism as implemented in SIMQdot code. For the sake of clarity, we only show in Fig. 5.8 the electron current for P-doped systems and the hole current for B-doped ones.

As the Fermi energy goes deeper in valence (conduction) band VB (CB), hole (electron) barriers EB (HB) are smaller, and the hole (electron) current is enhanced with respect to undoped systems. A clear relation between the shift of the E_F toward the CB (VB) and the increase of the electron (hole) conductance with respect to the undoped case is found. As seen in the transport study of undoped Si QDs, the current starts at a lower V_b for those systems with a smaller E_g, but the main influence on the final current is still the value for EB and HB, which can be quite different from the undoped case, depending on the shift of the E_F.

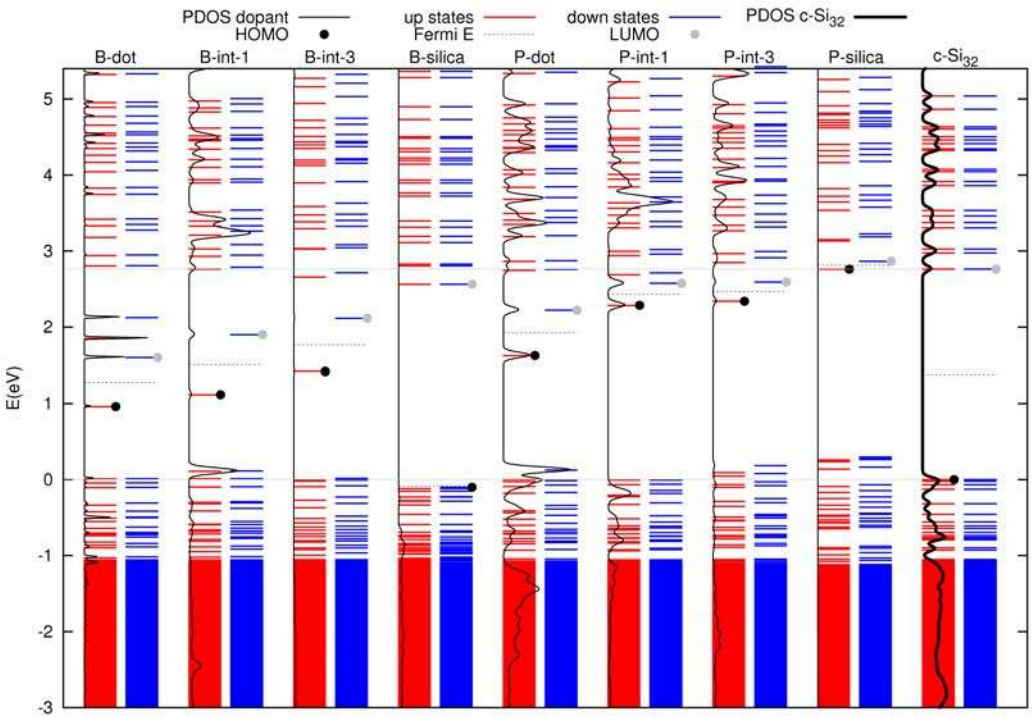

Figure 5.5: Kohn Sham eigenvalues for the c-Si_{32} doped systems. The undoped c-Si_{32} Kohn-Sham eigenvalues are shown for comparison. The energies were shifted until the VBM of the undoped systems is set to 0 eV.

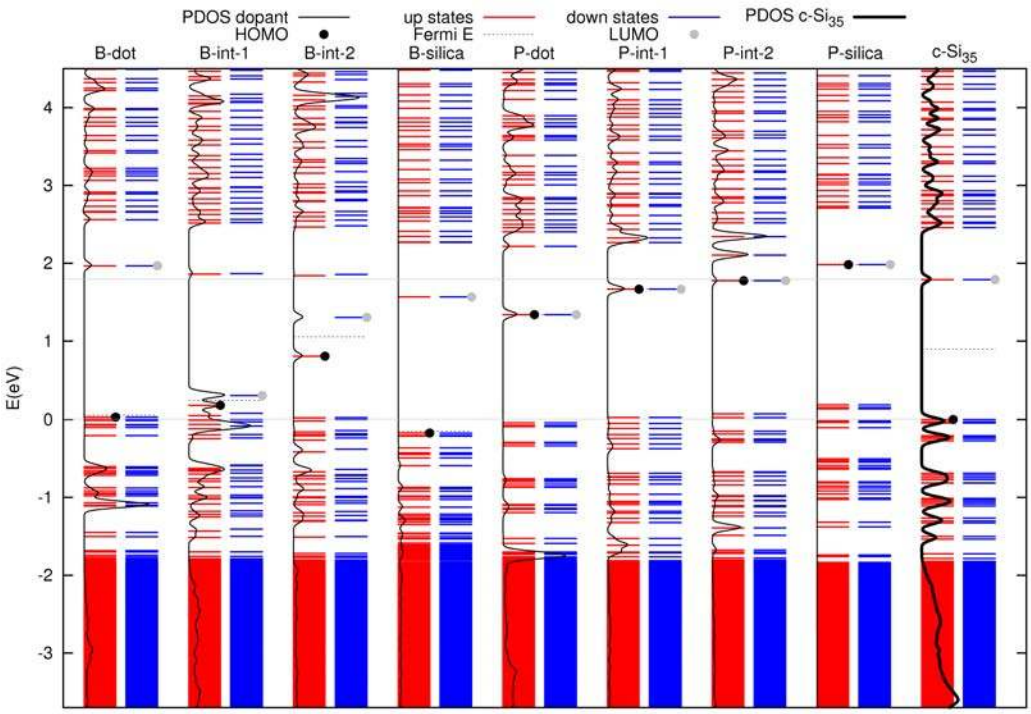

Figure 5.6: Kohn Sham eigenvalues for the c-Si_{35} doped systems. The undoped c-Si_{35} Kohn-Sham eigenvalues are shown for comparison. The energies were shifted until the VBM of the undoped systems is set to 0 eV.

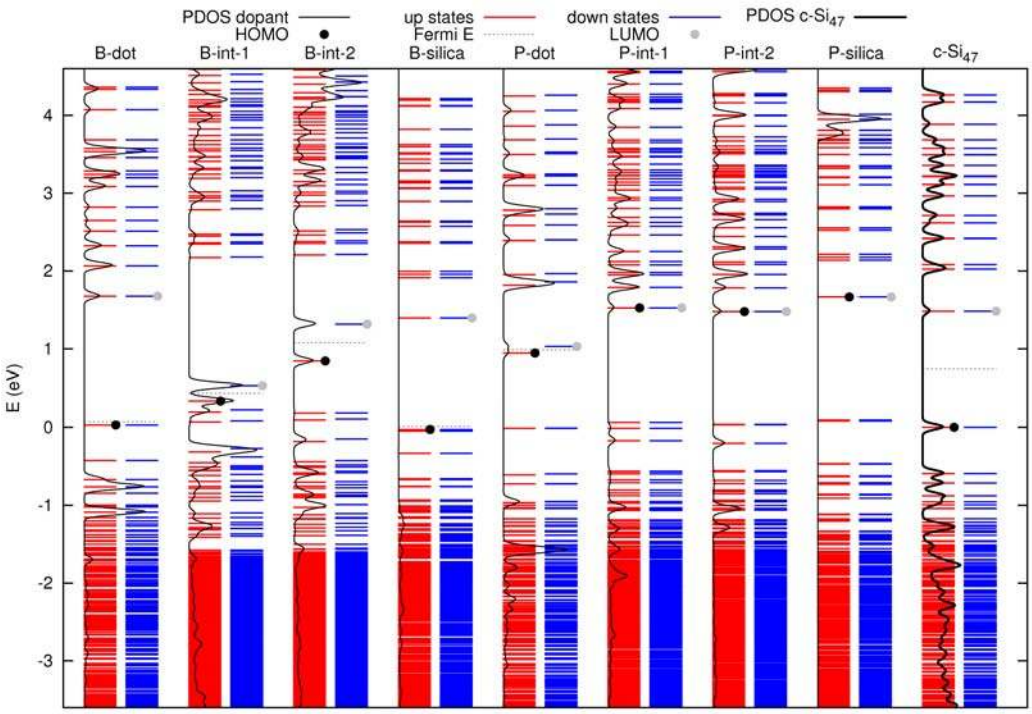

Figure 5.7: Kohn Sham eigenvalues for the c-Si_{47} doped systems. The undoped c-Si_{47} Kohn-Sham eigenvalues are shown for comparison. The energies were shifted until the VBM of the undoped systems is set to 0 eV.

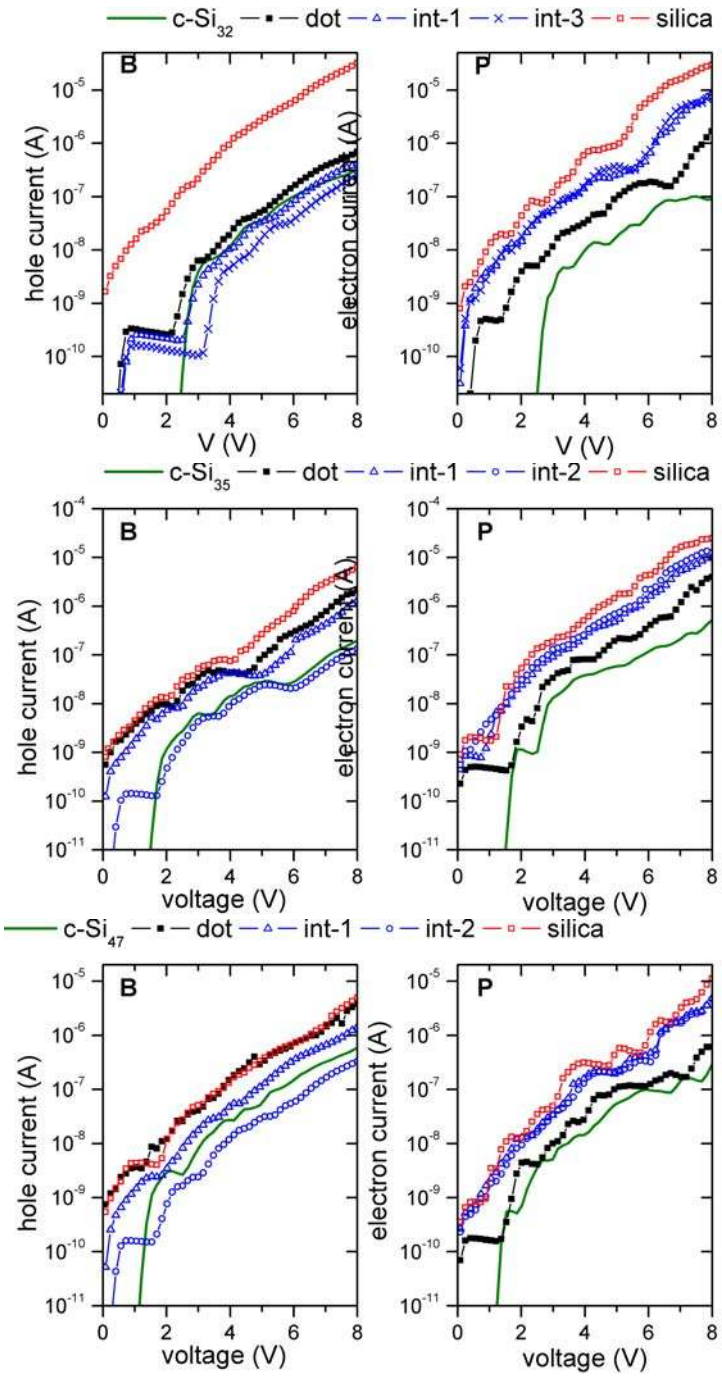

Figure 5.8: *I-V* characteristic for the different systems with respect to the undoped case.

We estimated the change in the conductivity (Table 5.2) by fitting with a linear law the high bias voltage range of the *I-V* characteristics, where the current is clearly monotonically increasing. For P-doping the change in conductivity, σ(doped)/σ(undoped), is of one or two orders of magnitude, while for B-doping the change is of the order of the unity or one order of magnitude. Experimentally, it seems that the increase of conductivity with respect to undoped systems is related to the concentration of dopant atoms: in B-doped (P-doped) systems there is more improvement of the transport for high (low) density of dopant atoms [54, 55]. Moreover, there is a general trend to measure more conductivity for P-doped systems than B-doped ones [62].
On the other hand, there is a clear tendency to decrease the change in the conductivity with Si QD size for a given position of the impurity.
Finally, as expected from electrical features of Section 5.3, there is an enhancement of the conductance for all the impurity positions of P-doped systems, having more conductance when more O atoms are bonded to the impurity; while in B-doped cases, there is an enhancement of the conductance for B-silica, B-dot, and B-int-1 (in that order) but not for B-int-2 and B-int-3.

$\frac{\sigma(doped)}{\sigma(undoped)}$	B-dot	B-int-1	B-int-2	B-int-3	B-silica	P-dot	P-int-1	P-int-2	P-int-3	P-silica
c-Si_{32}	2.43	1.63	—	1.02	119.82	39.04	229.94	—	210.17	668.28
c-Si_{35}	11.06	6.25	0.69	—	30.72	10.77	26.70	35.03	—	64.07
c-Si_{47}	6.98	2.41	0.67	—	10.36	3.27	24.96	24.61	—	57.75

Table 5.2: Change in the conductivity σ of the doped system with respect to the undoped system, σ(doped)/σ(undoped). For the case of doping with B atom is the hole conductivity and for the case of doping with P atom is the electron conductivity.

5.5 Other doping atoms

B and P atoms are two of the most commonly used impurities in silicon technology [62]. However, other elements of the III- and V- group can be used [67, 212–214].
We performed preliminary tests for N atom as p-type doping and Al atom as n-type doping only in the c-Si_{35} system.
As could be predicted, the formation energy tendency is similar for impurity atoms of the same group. However, surprisingly, the transport properties for impurities of the same group in the most energetic favorable position,

"int-2" for p-type and "dot" for n-type, have contrary behavior: if P-doping increases electron conductance in P-dot, Al decreases it in Al-dot, while B decreases hole conductance in B-int-2 and N increases it in N-int-2.
This new features open the possibility of interesting future studies from a technological point of view of nanodevice design. However, up to our knowledge, we have not found experimental studies to be able to compare the above-mentioned results.

5.6 Conclusion

The main conclusions of the study of doping in embedded Si QDs with respect to the location of the impurity and size of the QD are:

1. Compared with previous theoretical studies of free-standing Si QDs, B atom is still more stable at the interface of the Si QD, while P atom has a lower formation E in the center of the QD when it is embedded in a SiO_2 matrix. On the other hand, similarly to free-standing doped QDs, when QD size increases impurity levels are also shallower and the splitting of the levels decreases down to zero in most cases.

2. We found a relation between the increase of electron (hole) conductance and shift of the Fermi ΔE_F energy toward conduction (valence) band for almost P- (B-) doped systems. The magnitude of ΔE_F seems to be related with the difference in Mulliken population of the impurity atom with respect to the substituted Si atom.

3. There is a clear n-type behavior, i.e. enhancement of electron current, for P-doped QDs in all the impurity locations, being more conductive than the undoped systems as more O atoms are bonded to P impurity, due to shift of E_F toward the CB, which gives lower EB values than undoped Si QDs.

4. There is a clear p-type behavior, i.e. enhancement of hole current, for B-silica, B-dot, and B-int-1 systems, in that order, due to the shift of E_F toward the VB, which gives lower HB values than undoped Si QDs. However, B-int-2 and B-int-3 have deep states in the band gap that decreases the conductance with respect to the undoped case because the HB is higher than undoped Si QDs.

5. The enhancement of the current by doping is higher for smaller Si QDs.

With this study we have shown the applicability of the DFT-TH methodology on a case where the atomistic description is of special importance. The morphological and electrical modifications due to the inclusion of an impurity atom are easily described by DFT. In an overall conclusion, the DFT-TH methodology is desirable to the study the dependence on electron transport of features which are well described with DFT, such as doping, defects, specific atomic configurations, faceting, etc, and are difficult to modellize by analytical methods.

Chapter 6

Summary and Conclusions

6.1 Conclusions

This PhD Thesis is focused on the theoretical study of the electronic transport through silicon quantum dots (Si QDs) embedded in dielectric matrices. In particular, we have covered the tunnel transport through a single Si QD embedded in a SiO_2 matrix and the influence of Si QD size, amorphization level of the surrounding matrix, and doping atom position on the electronic transport properties.
The proposed methodology (the use of *ab initio* properties in transfer Hamiltonian formalism) to study transport in nanostructures shows its potentiallity for those situations where an atomistic description is the most suitable technique to model the feature of interest (a specific interface or faceting, the inclusion of certain atoms, any kind of defect, etc).

6.1.1 On the framework and methods

As we were interested in an *ab initio* description of the QDs, the size of the systems is limited by the current computational resources: embedded systems of around 1-1.7 nm of Si QD diameter are formed by several hundreds of atoms. This makes the direct comparison with experiments still a challenge.

We searched for a description of the electronic transport compatible with Density Functional Theory (DFT) characteristics, founding that, for our kind of systems, Transfer Hamiltonian (TH) method is more suitable than the

commonly used Non-Equilibrium Green Functions Formalism (NEGFF). The main reason is that for DFT-TH framework only one DFT calculation is needed in order to obtain a *I-V* curve, compared to the need of one DFT computation per *I-V* step, in the DFT-NEGFF framework. Moreover, the difficulty to describe explicitly, i.e. atom a atom, the junction between Al electrodes and SiO_2 matrix in DFT-NEGFF instead of treating the electrodes as a reservoir of electrons through a distribution function in the TH method without describing them in the DFT calculation, makes DFT-TH the most suitable technique for the study of embedded Si QDs. However, the above reasons do not modify the potentiality of the DFT-NEGFF framework for systems with less number of atoms, such as bulk, molecules or nano wires, as have been widely reported in the literature.

The proposed DFT-TH procedure to compute an *I-V* characteristic for an embedded Si QD can be summarized as:

1. Relaxation of the structure with DFT.

2. Computation by DFT of the projected density of states (PDOS) of the subsystem formed by the Si atoms of the QD and the O atoms in the first shell surrounding it.

3. Extraction of the values for the electron (hole) barrier, EB (HB), from the DFT calculation.

4. Computation of the *I-V* characteristic by TFH with SIMQdot code, by using the PDOS and barrier values from the previous DFT calculation.

After doing the necessary tests to SIMQdot, the code used to compute electronic transport, the main influence in the final current value, for a given DOS and distance between QD and electrode, is the description of the potential well (i.e. the electron and hole barriers). Other computational parameters such as effective masses and QD radius are less relevant. This predominance is due to the exponential dependence of the transmission coefficient for tunneling transport with barrier height and because the change of the barrier value with the applied bias voltage.

6.1.2 On the QD size

In the case of embedded QDs of few nanometers, the strong non-planar interface between Si and SiO_2 require a different treatment with respect to common planar Si/SiO_2 devices. In this PhD Thesis, we have shown that, for small QD sizes, the particle-in-a-box model cannot describe accurately DOS and band offset, because of the large contribution of interface states. In this regime an *ab initio* approach is necessary to take into account the atomistic detail of the interface between the Si QD and the first shell of O atoms surrounding it.

A constant correction to the computed DFT band offset values for all the Si QDs was proposed in order to overcome the understimation of the band gap of bulk SiO_2 provided by DFT by matching the experimental values of planar Si/SiO_2 band offsets. Our proposed approximation is substained on previous theoretical results which show, (1) the decoupling in embedded Si QD in SiO_2 matrix between SiO_2 matrix electronic states and the electronic states of the subsystem formed by the Si QD atoms of the QD and the first shell O atoms surrounding it, and (2) corrections on DFT gap for Si QDs can be negligible.

A correlation between EB (HB) and electron (hole) current was found, obtaining larger current values for smaller energy barriers. Specifically, a contrary dependence on Si QD size and amorphization level is found for electron and hole current. On one hand, electron (hole) current is higher for large (small) Si QDs, and, on the other hand, it is enhanced for amorphous (crystalline) systems.

6.1.3 On the effects of doping

Finally, the DFT-TH technique was used to study the influence of impurity atoms, B for p-doping and P for n-doping, in embedded Si QDs. It is remarkable that this study is one of the first attempts to model with DFT the inclusion of impurity atoms in embedded Si QDs, after the wide knowledge of *ab initio* works on free-standing Si QDs of the last years.

The principal features that we found were:

1. More structural distorsion for B-doping than P-doping.

2. The impurity positions with lower formation energy are inside the dot for P-doping (P-dot) and at the interface for B-doping (B-int).

3. More polarization charge and splitting of the spin levels for decreasing Si QD size, i.e. increasing quantum confinement.

4. Decrease of doped system energy gap with QD size.

5. Relation between shift of the Fermi energy and change in the Mulliken population of the substituted Si atom.

6. Relation between shift of the Fermi energy and improvement of conductivity in doped systems (due to the change in energy barriers).

7. Improvement of the conductivity for the most energetically favorable position of P-doping (P-dot) but not for the position of B-doping (B-int).

8. Change in the conductivity between doped and undoped is higher for P-doping than B-doping for a given Si QD size and impurity position, and decreases with QD size for a given specie and impurity position.

6.2 Future work

After the experience of modelling defect-free Si QDs, intrinsic and doped, and the study of electronic transport through a single Si QD, we opened several fields. Among them, we found particularly worth to study in future works:

1. Larger Si QD embedded in silica matrix. Although this represents a computational challenge, would be interesting to see if our results in the nanometer range can be extrapolated to larger QDs. There are two interesting aspects that would be checked: (1) if the same tendency of band offsets and energy barriers between Si QD and SiO_2 matrix to approach the value of planar Si/SiO_2 heterojunction is maintained (also for larger QDs the direct comparison with experiments would be possible), and (2) which mechanism will be more significant for hole transport (large hole barrier, which will lead to smaller hole current as QD size increases, or small band gap and large number of states, which will lead to higher hole current as QD size increases).

2. Quasiparticle and excitonic correction to the here-reported systems in order to check the validity of the same energy shift in the SiO_2-related states for all the diameter range. We know that it would be a huge, computationally demanding, task. Up to our knowledge, it has been only done, starting with DFT eigenvalues, for the smallest QD of 10 Si atoms [75], and, with TB eigenvalues, for higher QDs [182].

3. The natural extension of this work would be to perform a transport calculation of an array of QDs. This can be simply done within the adopted formalism by taking into account the capacitive coupling and the transmission coefficients between the QDs. However, we should have in mind that SIMQdot has implicitly the approximation of a network of non interacting QDs, i.e. low density systems. On the other hand, it is known that as the QDs become nearer, the flat bands began to create subbands due to the interactions between QDs [215]. T herefore, the use of DFT results in an array of QDs within TH is not as straightforward as it could seem in principle, but at the same time is excitingly challenging.

4. The use of other kind of matrices: SiC and Si_xN_y. Preliminary DFT results gave different troubles for each matrix that had not allowed us to include them in this PhD Thesis. It is also noticeable that in the literature there are only a few DFT studies of this kind of matrices.
   Si QDs embedded in SiC matrix give structural problems in a bare DFT description, in terms of the creation of the QD as is explained in this PhD Thesis. The resulting system has a huge initial stress that gives unphyisical results as it reaches the relaxed structure (such as a huge structural deformation of the Si QD and the mixing of valence and conduction states of the DOS). Therefore, new studies should be done in order to find a proper description of these kind of systems.
   On the other hand, Si_xN_y matrix has lots of defects. Preliminary studies allowed us to localize these defect states and to differentiate them from QD states, which are also localized states. Thus, we could generate a random distribution of defects, with a linear dependence between the energy of the defect and its effective radius but with a uniform distribution with respect to its position inside the dielectric matrix. The preliminary *I-V* characteristics show a different behavior between QD states and defects states. The latest ones are responsible of increasing

the current values in the low bias voltage regime, while the the high voltage regime is mainly dominated only for QD states.

Appendix A

Mulliken population of doped Si QDs embedded in a SiO_2 matrix

Additional information of doped systems.

c-Si_{32}	Q_{up}-Q_{down}	Q_{up} (Δ Q_{up})	Q_{down} (Δ Q_{down})	Q_{up}+Q_{down} (Δ Q_{up}+Q_{down})
B	0.065	1.629 (-0.395)	1.564 (-0.460)	**3.193 (-0.855)**
Si (-B)	0.007	1.506 (-0.041)	1.499 (-0.048)	3.005 (-0.089)
Si (-B)	-0.001	1.974 (-0.040)	1.975 (-0.039)	3.949 (-0.079)
Si (-B)	0.833	2.506 (0.424)	1.673 (-0.409)	4.179 (0.015)
Si (-B)	-0.002	1.991 (-0.043)	1.993 (-0.041)	3.984 (-0.084)
c-Si_{35}				
B	0.000	1.653 (-0.427)	1.653 (-0.427)	**3.306 (-0.854)**
Si (-B)	0.000	2.052 (-0.044)	2.052 (-0.044)	4.104 (-0.088)
Si (-B)	0.000	2.058 (-0.042)	2.058 (-0.042)	4.116 (-0.084)
Si (-B)	0.000	2.060 (-0.035)	2.060 (-0.035)	4.120 (-0.070)
Si (-B)	-0.001	2.060 (-0.033)	2.061 (-0.032)	4.121 (-0.065)
c-Si_{47}				
B	0.000	1.588 (-0.414)	1.588 (-0.414)	**3.176 (-0.828)**
Si (-B)	0.000	1.977 (-0.042)	1.977 (-0.042)	3.954 (-0.084)
Si (-B)	0.000	1.977 (-0.042)	1.977 (-0.042)	3.954 (-0.084)
Si (-B)	0.000	1.977 (-0.042)	1.977 (-0.042)	3.954 (-0.084)
Si (-B)	0.000	1.977 (-0.042)	1.977 (-0.042)	3.954 (-0.084)

Table A.1: Mulliken population for the position B-dot in each size. B atom and Si atoms bonded to it are reflexed.

c-Si_{32}	Q_{up}-Q_{down}	Q_{up} (Δ Q_{up})	Q_{down} (Δ Q_{down})	Q_{up}+Q_{down} (Δ Q_{up}+Q_{down})
B	0.019	1.565 (-0.202)	1.546 (-0.221)	**3.111 (-0.423)**
O (-B)	0.003	3.076 (-0.208)	3.073 (-0.211)	6.149 (-0.419)
Si (-B)	0.002	2.026 (-0.058)	2.024 (-0.060)	4.050 (-0.118)
Si (-B)	0.000	2.036 (-0.060)	2.036 (-0.060)	4.072 (-0.120)
Si (-B)	0.847	2.500 (0.400)	1.653 (-0.447)	4.153 (-0.047)
c-Si_{35}				
B	0.099	1.694 (-0.143)	1.595 (-0.242)	**3.289 (-0.385)**
O (-B)	0.034	3.111 (-0.163)	3.077 (-0.197)	6.188 (-0.360)
Si (-B)	0.097	1.859 (-0.009)	1.762 (-0.106)	3.621 (-0.115)
Si (-B)	-0.004	2.024 (-0.076)	2.028 (-0.072)	4.052 (-0.148)
Si (-B)	0.097	1.845 (-0.001)	1.748 (-0.098)	3.593 (-0.099)
c-Si_{47}				
B	0.166	1.744 (-0.089)	1.578 (-0.255)	**3.322 (-0.344)**
O (-B)	0.074	3.129 (-0.143)	3.055 (-0.217)	6.184 (-0.360)
Si (-B)	0.155	1.688 (0.033)	1.533 (-0.122)	3.221 (-0.089)
Si (-B)	0.037	2.019 (-0.045)	1.982 (-0.082)	4.001 (-0.127)
Si (-B)	0.018	2.021 (-0.043)	2.003 (-0.061)	4.024 (-0.104)

Table A.2: Mulliken population for the position B-int-1 in each size. B atom, and Si and O atoms bonded to B are reflexed.

c-Si_{35}	Q_{up}-Q_{down}	Q_{up} (Δ Q_{up})	Q_{down} (Δ Q_{down})	Q_{up}+Q_{down} (Δ Q_{up}+Q_{down})
B	0.049	1.626 (-0.011)	1.577 (-0.060)	**3.203 (-0.071)**
O (-B)	0.009	3.090 (-0.190)	3.081 (-0.199)	6.171 (-0.389)
O (-B)	0.011	3.095 (-0.183)	3.084 (-0.194)	6.179 (-0.377)
Si (-B)	0.580	2.110 (0.256)	1.530 (-0.324)	3.640 (-0.068)
Si (-B)	0.040	1.812 (-0.056)	1.772 (-0.096)	3.584 (-0.152)
c-Si_{47}				
B	0.061	1.648 (-0.007)	1.587 (-0.068)	**3.235 (-0.075)**
O (-B)	0.011	3.104 (-0.188)	3.093 (-0.199)	6.197 (-0.387)
O (-B)	0.009	3.079 (-0.213)	3.070 (-0.222)	6.149 (-0.435)
Si (-B)	0.557	2.076 (0.243)	1.519 (-0.314)	3.595 (-0.071)
Si (-B)	0.068	1.799 (-0.034)	1.731 (-0.102)	3.530 (-0.136)

Table A.3: Mulliken population for the position B-int-2 in each size. B atom, and Si and O atoms bonded to B are reflexed.

c-Si_{32}	Q_{up}-Q_{down}	Q_{up} (Δ Q_{up})	Q_{down} (Δ Q_{down})	Q_{up}+Q_{down} (Δ Q_{up}+Q_{down})
B	0.007	1.650 (0.103)	1.643 (0.096)	**3.293 (+0.199)**
O (-B)	0.001	3.100 (-0.187)	3.099 (-0.188)	6.199 (-0.375)
O (-B)	0.001	3.094 (-0.192)	3.093 (-0.193)	6.187 (-0.385)
O (-B)	0.002	3.086 (-0.185)	3.084 (-0.187)	6.170 (-0.372)
Si (-B)	0.797	2.363 (0.339)	1.566 (-0.458)	3.929 (-0.119)

Table A.4: Mulliken population for the position B-int-3 in each size. B atom, and Si and O atoms bonded to B are reflexed.

c-Si_{32}	Q_{up}-Q_{down}	Q_{up} (Δ Q_{up})	Q_{down} (Δ Q_{down})	Q_{up}+Q_{down} (Δ Q_{up}+Q_{down})
B	-0.015	1.673 (0.204)	1.688 (0.219)	**3.361 (+0.423)**
O (-B)	0.098	3.167 (-0.096)	3.069 (-0.194)	6.236 (-0.290)
O (-B)	0.111	3.148 (-0.106)	3.037 (-0.217)	6.185 (-0.323)
O (-B)	0.006	3.135 (-0.132)	3.129 (-0.138)	6.264 (-0.270)
O (-B)	0.126	3.180 (-0.086)	3.054 (-0.212)	6.234 (-0.298)
c-Si_{35}				
B	0.000	1.694 (0.195)	1.694 (0.195)	**3.388 (+0.390)**
O (-B)	0.000	3.114 (-0.141)	3.114 (-0.141)	6.228 (-0.282)
O (-B)	0.000	3.115 (-0.132)	3.115 (-0.132)	6.230 (-0.264)
O (-B)	0.000	3.143 (-0.110)	3.143 (-0.110)	6.286 (-0.220)
O (-B)	0.000	3.146 (-0.118)	3.146 (-0.118)	6.292 (-0.236)
c-Si_{47}				
B	0.000	1.664 (0.225)	1.664 (0.225)	**3.328 (+0.450)**
O (-B)	0.000	3.101 (-0.168)	3.101 (-0.168)	6.202 (-0.336)
O (-B)	0.000	3.101 (-0.168)	3.101 (-0.168)	6.202 (-0.336)
O (-B)	0.000	3.101 (-0.168)	3.101 (-0.168)	6.202 (-0.336)
O (-B)	0.000	3.101 (-0.168)	3.101 (-0.168)	6.202 (-0.336)

Table A.5: Mulliken population for the position B-silica in each size. B atom and O atoms bonded to B are reflexed.

c-Si_{32}	Q_{up}-Q_{down}	Q_{up} (Δ Q_{up})	Q_{down} (Δ Q_{down})	Q_{up}+Q_{down} (Δ Q_{up}+Q_{down})
P	0.102	2.619 (0.595)	2.517 (0.493)	**5.136 (+1.088)**
Si (-P)	0.002	1.527 (-0.020)	1.525 (-0.022)	3.052 (-0.042)
Si (-P)	0.011	1.971 (-0.043)	1.960 (-0.054)	3.931 (-0.097)
Si (-P)	0.711	2.448 (0.366)	1.737 (-0.345)	4.185 (0.021)
Si (-P)	0.020	2.002 (-0.032)	1.982 (-0.052)	3.984 (-0.084)
c-Si_{35}				
P	0.000	2.563 (0.483)	2.563 (0.483)	**5.126 (+0.966)**
Si (-P)	0.000	2.063 (-0.033)	2.063 (-0.033)	4.126 (-0.066)
Si (-P)	0.000	2.067 (-0.033)	2.067 (-0.033)	4.134 (-0.066)
Si (-P)	0.000	2.071 (-0.024)	2.071 (-0.024)	4.142 (-0.048)
Si (-P)	0.000	2.076 (-0.017)	2.076 (-0.017)	4.152 (-0.034)
c-Si_{47}				
P	0.035	2.523 (0.521)	2.488 (0.486)	**5.011 (+1.007)**
Si (-P)	0.097	2.049 (0.030)	1.952 (-0.067)	4.001 (-0.037)
Si (-P)	0.097	2.049 (0.030)	1.952 (-0.067)	4.001 (-0.037)
Si (-P)	0.097	2.049 (0.030)	1.952 (-0.067)	4.001 (-0.037)
Si (-P)	0.097	2.049 (0.030)	1.952 (-0.067)	4.001 (-0.037)

Table A.6: Mulliken population for the position P-dot in each size. P atom and Si atoms bonded to P are reflexed.

c-Si_{32}	Q_{up}-Q_{down}	Q_{up} (Δ Q_{up})	Q_{down} (Δ Q_{down})	Q_{up}+Q_{down} (Δ Q_{up}+Q_{down})
P	0.150	2.481 (0.714)	2.331 (0.564)	**4.812 (+1.278)**
O (-P)	-0.003	3.195 (-0.089)	3.198 (-0.086)	6.393 (-0.175)
Si (-P)	0.146	2.115 (0.031)	1.969 (-0.115)	4.084 (-0.084)
Si (-P)	0.339	2.240 (0.144)	1.901 (-0.195)	4.141 (-0.051)
Si (-P)	0.154	2.128 (0.028)	1.974 (-0.126)	4.102 (-0.098)
c-Si_{35}				
P	0.000	2.493 (0.656)	2.493 (0.656)	**4.986 (+1.312)**
O (-P)	0.000	3.192 (-0.082)	3.192 (-0.082)	6.384 (-0.164)
Si (-P)	0.000	1.816 (-0.052)	1.816 (-0.052)	3.632 (-0.104)
Si (-P)	0.000	2.021 (-0.079)	2.021 (-0.079)	4.042 (-0.158)
Si (-P)	0.000	1.807 (-0.039)	1.807 (-0.039)	3.614 (-0.078)
c-Si_{47}				
P	0.000	2.480 (0.647)	2.480 (0.647)	**4.960 (+1.294)**
O (-P)	0.000	3.179 (-0.093)	3.179 (-0.093)	6.358 (-0.186)
Si (-P)	0.000	1.610 (-0.045)	1.610 (-0.045)	3.220 (-0.090)
Si (-P)	0.000	2.017 (-0.047)	2.017 (-0.047)	4.034 (-0.094)
Si (-P)	0.000	2.017 (-0.047)	2.017 (-0.047)	4.034 (-0.094)

Table A.7: Mulliken population for the position P-int-1 in each size. P atom, and Si and O atoms bonded to P are reflexed.

c-Si_{35}	Q_{up}-Q_{down}	Q_{up} (Δ Q_{up})	Q_{down} (Δ Q_{down})	Q_{up}+Q_{down} (Δ Q_{up}+Q_{down})
P	0.000	2.429 (0.792)	2.429 (0.792)	**4.858 (+1.584)**
O (-P)	0.000	3.168 (-0.112)	3.168 (-0.112)	6.336 (-0.224)
O (-P)	0.000	3.164 (-0.114)	3.164 (-0.114)	6.328 (-0.228)
Si (-P)	0.000	1.792 (-0.062)	1.792 (-0.062)	3.584 (-0.124)
Si (-P)	0.000	1.796 (-0.072)	1.796 (-0.072)	3.592 (-0.144)
c-Si_{47}				
P	0.000	2.415 (0.760)	2.415 (0.760)	**4.830 (+1.520)**
O (-P)	0.000	3.181 (-0.111)	3.181 (-0.111)	6.362 (-0.222)
O (-P)	0.000	3.181 (-0.111)	3.181 (-0.111)	6.362 (-0.222)
Si (-P)	0.000	1.784 (-0.049)	1.784 (-0.049)	3.568 (-0.098)
Si (-P)	0.000	1.784 (-0.049)	1.784 (-0.049)	3.568 (-0.098)

Table A.8: Mulliken population for the position P-int-2 in each size. P atom, and Si and O atoms bonded to P are reflexed.

c-Si_{32}	Q_{up}-Q_{down}	Q_{up} (Δ Q_{up})	Q_{down} (Δ Q_{down})	Q_{up}+Q_{down} (Δ Q_{up}+Q_{down})
P	0.023	2.448 (0.901)	2.425 (0.878)	**4.873 (1.779)**
O (-P)	0.001	3.151 (-0.136)	3.150 (-0.137)	6.301 (-0.273)
O (-P)	0.006	3.154 (-0.132)	3.148 (-0.138)	6.302 (-0.270)
O (-P)	-0.001	3.138 (-0.133)	3.139 (-0.132)	6.277 (-0.265)
Si (-P)	0.149	2.021 (-0.003)	1.872 (-0.152)	3.893 (-0.155)
Si^{24} (-Si-P)	0.409	2.308 (0.226)	1.899 (-0.183)	4.207 (0.043)

Table A.9: Mulliken population for the position P-int-3 in each size. P atom, Si and O atoms bonded to P and other interesting atoms are reflexed.

c-Si_{32}	Q_{up}-Q_{down}	Q_{up} (Δ Q_{up})	Q_{down} (Δ Q_{down})	Q_{up}+Q_{down} (Δ Q_{up}+Q_{down})
P	0.000	2.517 (1.048)	2.517 (1.048)	**5.034 (+2.096)**
O (-P)	0.000	3.098 (-0.165)	3.098 (-0.165)	6.196 (-0.330)
O (-P)	0.000	3.087 (-0.167)	3.087 (-0.167)	6.174 (-0.334)
O (-P)	0.000	3.109 (-0.158)	3.109 (-0.158)	6.218 (-0.316)
O (-P)	0.000	3.103 (-0.163)	3.103 (-0.163)	6.206 (-0.326)
$Si^{24(a)}$	0.121	2.148 (0.066)	2.027 (-0.055)	4.175 (0.011)
$Si^{11(a)}$	0.109	2.144 (0.060)	2.035 (-0.049)	4.179 (0.011)
c-Si_{35}				
P	0.000	2.541 (1.042)	2.541 (1.042)	**5.082 (+2.084)**
O (-P)	0.000	3.090 (-0.165)	3.090 (-0.165)	6.180 (-0.330)
O (-P)	0.000	3.082 (-0.165)	3.082 (-0.165)	6.164 (-0.330)
O (-P)	0.000	3.096 (-0.157)	3.096 (-0.157)	6.192 (-0.314)
O (-P)	0.000	3.094 (-0.170)	3.094 (-0.170)	6.188 (-0.340)
c-Si_{47}				
P	0.000	2.502 (1.063)	2.502 (1.063)	**5.004 (+2.126)**
O (-P)	0.000	3.100 (-0.169)	3.100 (-0.169)	6.200 (-0.338)
O (-P)	0.000	3.100 (-0.169)	3.100 (-0.169)	6.200 (-0.338)
O (-P)	0.000	3.100 (-0.169)	3.100 (-0.169)	6.200 (-0.338)
O (-P)	0.000	3.100 (-0.169)	3.100 (-0.169)	6.200 (-0.338)

Table A.10: Mulliken population for the position P-silica in each size. P atom, Si and O atoms bonded to P and other interesting atoms are reflexed. $^{(a)}$ Si atoms inside the Si QD that are aligned to P impurity with bonds larger than the mean Si-Si bond inside the Si QD, are responsible of the HOMO and LUMO of this system.

Appendix B

Scientific Curriculum

NÚRIA GARCÍA CASTELLÓ
Born in April 15th of 1986 in Barcelona, Spain.

Current position: PhD student at the Department of Electronics of the Universitat de Barcelona. Pursuing for the PhD Degree with the Dissertation "*Atomistic study of structural and electronic transport properties of silicon quantum dots for optoelectronic applications*". Advisors: Dr. J. Daniel Prades García and Dr. Albert Cirera Hernández.

B.1 Academic Degrees

1. **MASTER** in NANOSCIENCE and NANOTECHNOLOGY.
   Master Thesis "First-principles study of the dependence of silicon electronic transport properties on the crystallographic growth".
   Average qualification 9.70/10.00
   Universitat de Barcelona (Barcelona, 2010)

2. **DEGREE** in PHYSICS.
   Average qualification 2.57/4.00
   Universitat de Barcelona (Barcelona, 2009)

3. BACHELOR GRADUATED with honors.
   IES Costa i Llobera (Barcelona, 2004)

B.2 Publications

1. Reza R. Zamani, Maria Ibáñez, Martina Luysberg, Nuria Garcia-Castello, Lothar Houben, Joan Daniel Prades, Vincenzo Grillo, Rafal E. Dunin-Borkowski, Joan Ramon Morante, Andreu Cabot, and Jordi Arbiol. "*Polarity-Driven Branching in Cu-Based Quaternary Chalcogenide Nanostructures*". ACS Nano, Just Accepted Manuscript. DOI: 10.1021/nn405747h (February 28, 2014)

2. Wenhua Li, Maria Ibáñez, Reza Zamani, Nuria García-Castelló, Stephane Gorsse, Doris Cadavid, Joan Daniel Prades, Jordi Arbiol, and Andreu Cabot. "*$Cu_2HgSnSe_4$ Nanoparticles: Synthesis and Thermoelectric Properties*". Cryst. Eng. Comm., 2013, *15* (44), pp. 8966-8971. DOI: 10.1039/C3CE41583J

3. Nuria Garcia-Castello, Sergio Illera, Roberto Guerra, Joan Daniel Prades, Stefano Ossicini, and Albert Cirera. "*Silicon quantum dots embedded in a SiO_2 matrix: From structural study to carrier transport properties*". Phys. Rev. B, 2013, *88* (7), pp. 075322 1-11

4. Mauro Epifani, Nuria Garcia-Castello, Joan Daniel Prades, Albert Cirera, Teresa Andreu, Jordi Arbiol, Pietro Siciliano, and Joan R. Morante. "*Suppression of the NO_2 interference by chromium addition in WO_3-based ammonia sensors. Investigation of the structural properties and of the related sensing pathways*". Sensors and Actuators B, 2013, *187* (0), pp. 308-312. DOI: 10.1016/j.snb.2012.11.072

5. Nuria Garcia-Castello, Joan Daniel Prades, Roberto Orlando, and Albert Cirera. "*Stability Model of Silicon Nanowire Polymorphs and First-Principle Conductivity of Bulk Silicon*", J.Phys. Chem. C, 2012, *116* (41), pp. 22078-22085. DOI: 10.1021/jp307449y

6. Sergio Illera, Nuria Garcia-Castello, Joan Daniel Prades, and Albert Cirera. "*A transfer Hamiltonian approach for an arbitrary quantum dot array in the self-consistent field regime*", J. Appl. Phys., 2012, *112* (9), pp 093701. DOI: 10.1063/1.4763359

7. Maria Ibáñez, Doris Cadavid, Reza Zamani, Nuria Garcia-Castello, Victor Izquierdo-Roca, Wenhua Li, Andrew Fairbrother, Joan Daniel Prades, Alexey Shavel, Jordi Arbiol, Alejandro Pérez-Rodríguez, Joan

Ramon Morante, and Andreu Cabot. "*Composition Control and Thermoelectric Properties of Quaternary Chalcogenide Nanocrystals: The Case of Stannite $Cu_2CdSnSe_4$*", Chem. Mater., 2012, *24* (3), pp 562–570. DOI: 10.1021/cm2031812

B.3 Contributions in Conferences

- Conference: *14th International Meeting on Chemical Sensors (IMCS 2012)*
  Location: Nüremberg (Germany) Year: 2012
  Type of contribution: **Collaboration in oral presentation**
  Authors: M. Epifani, T. Andreu, J. Arbiol, N. Garcia-Castello, J. D. Prades, A. Cirera, P.Siciliano, and J. R. Morante.
  Title: *Suppression of NO_2 interference by Chromium Addition in WO_3-Based Ammonia Sensors. Investigation of the Structural Properties and of the Related Sensing Pathways*

- Conference: *European Materials Research Society (E-MRS). Spring Meeting*
  Location: Strasbourg (France) Year: 2012
  Type of contribution: **Collaboration in oral presentation**
  Authors: M. Ibáñez, D. Cadavid, R. Zamani, N. Garcia-Castello, J.D. Prades, J. Arbiol, J.R. Morante, and A. Cabot.
  Title: *Copper-based diamond-like semiconductor nanostructures for thermoelectric applications*

- Conference: *IV Jornada del Instituto de Nanociencia y Nanotecnología de la UB (IN2UB)*
  Location: Barcelona, (Spain) Year: 2011
  Type of contribution: **Collaboration in oral and poster presentation**
  Authors: S. Illera, N. Garcia-Castello, J.D. Prades, and A. Cirera.
  Title: *Non-coherent transport in serial/parallel quantum dots in self-consistent field regime*

- Conference: *9th European Conference on Thermoelectrics*
  Location: Thessaloniki (Greece) Year 2011
  Type of contribution: **Collaboration in oral presentation**

Authors:: M. Ibáñez, D. Cadavid, R. Zamani, N. Garcia-Castello, J.D. Prades, J. Arbiol, J.R. Morante, and A. Cabot
Title: *Thermoelectric properties of nanostructured I2 II IV VI4 Adamantines*

- Conference: *European Materials Research Society (E-MRS). Spring Meeting*
  Location: Nice (France) Year: 2011
  Type of contribution: **Oral presentation**
  Authors: N. Garcia-Castello, S. Illera, J.D. Prades, and A. Cirera
  Title: *First-principles study of the dependence of electronic transport properties on the growth direction of Si nanowires*

- Conference: *European Materials Research Society (E-MRS). Spring Meeting*
  Location: Nice (France) Year: 2011
  Type of contribution: **Collaboration in oral presentation**
  Authors: S. Illera, N. Garcia-Castello, J.D. Prades, and A. Cirera
  Title: *Non-coherent transport in serial/parallel quantum dots in self-consistent field regime*

- Conference: *III Jornada del Instituto de Nanociencia y Nanotecnología de la UB (IN2UB)*
  Location: Barcelona (Spain) Year: 2010
  Type of contribution: **Poster presentation**
  Authors: N. Garcia-Castello, J.D. Prades, and A. Cirera
  Title: *First-principles study of the dependence of silicon electronic transport on the crystallographic growth*

B.4 Participation in Projects

Research projects

- Title of the Project: "*Silicon Nanodots for Solar Cell Tandem (NASCEnT)*"
  Project number: FP7-NMP-245977
  Funded by: European Project
  Period: July 2009 - Agost 2013

B.5 Experience with Scientific Equipments and Techniques

- **Ab initio DFT** codes: SIESTA, CRYSTAL, CASTEP, ESPRESSO.
- **Supercomputing** facilities: MareNostrum Supercomputer (Barcelona Supercomputing Center-Centro Nacional de Supercomputación), Centre de Supercomputació de Catalunya (CESCA).

B.6 Specialization courses

- Yambo Hands-on Tutorial on Electronic and Optical Excitations: from Basics to Advanced Applications
  Organized by: CECAM. EPFL, Lausanne (Switzerland)
  Dates: 08/04/2013-12/04/2013
- Curs en llenguatge de programació
  Organized by: Departament d'Electrònica i Institut de Ciències de l'Educació (ICE). Universidad de Barcelona, Barcelona (Spain)
  Dates: 23/07/2012-27/07/2012
- Fundamentals of Nanoelectronics: Quantum Models
  Organized by: Nanohub, Purdue University (Estados Unidos). Online Course
  Dates: 19/03/2012-05/05/2012
- Fundamentals of Nanoelectronics: Basic Concepts
  Organized by: Nanohub, Purdue University (Estados Unidos). Online Course
  Dates: 23/01/2012-09/03/2012
- V Jornada de Usuarios de la Red Española de Supercomputación (RES)
  Organized by: Barcelona Supercomputing Center-Red Española de Supercomputación (BSC-RES). Universidad de Valencia, Valencia (Spain)
  Dates: 26/10/2011
- Curso de usuarios de sistemas de cálculo de altas prestaciones de l'XRQTC
  Organized by: Xarxa de Referència de Química Teòrica i Computa-

cional (XRQTC). Universidad de Barcelona, Barcelona (Spain)
Dates: 14/07/2010-15/07/2010

- Administración de sistemas de ficheros para entornos de cálculo de altas prestaciones y entornos críticos
  Organized by: Xarxa de Referència de Química Teòrica i Computacional (XRQTC). Universidad de Barcelona, Barcelona (Spain)
  Dates: 9/07/2010

- Efficient density-functional calculations with atomic orbitals: A hands-on tutorial on the SIESTA code
  Organized by: Universidad de Cantabria, Santander (Spain)
  Dates: 07/06/2010-10/06/2010

- TranSiesta School 2009
  Organized by: CESCA, Barcelona (Spain)
  Dates: 14/12/2009-16/12/2009

- Curso de Entorno de trabajo y herramientas de la química computacional en el CESCA
  Organized by: CESCA, Barcelona (Spain)
  Dates: 23/11/2009-24/11/2009

- Summerschool MSSC2009 – Ab initio Modeling in Solid State Chemistry
  Organized by: University of Torino and NIS Center of Excellence. University of Torino, Torino (Italy)
  Dates: 06/09/2009-11/09/2009

- Course Introduction to Solid State Chemistry. 3rd Summer School in Theoretical and Computacional Chemistry of Catalonia
  Organized by: Xarxa de Referència en Química Teòrica i Computacional. Universidad de Barcelona, Barcelona (España)
  Dates: 06/07/2009-10/07/2009

Apèndix C

Resum en català

Estudi atomístic de propietats estructurals i de transport electrònic de nanopartícules de silici per a aplicacions optoelectròniques

C.1 Introducció

És indiscutible que el silici ha esdevingut el material més àmpliament utilitzat en electrònica durant les darreres dècades [1, 2]. Les qualitats del silici són ben conegudes: des de la seva abundància i el baix cost econòmic fins a la seva capacitat de crear heteroestructures amb òxids d'una forma senzilla, de forma que ha esdevingut el material essencial en circuits electrònics integrats, en la tecnologia CMOS o en altres tipus de transistors (la capacitat de disminuir la mida dels dispositius és la base del succés de la tecnologia actual). Un pas mes enllà, però, és la idea d'integrar l'electrònica i la fotònica en una mateixa tecnologia basada en silici [3]. Per tal superar els dos principals obstacles d'una possible *fotònica de Si bulk* (band gap indirecte i l'emissió en el rang dels infrarojos), es van haver de buscar noves estratègies. La transició indirecte entre el mínim de la banda de conducció i el màxim de la banda de valència en Si bulk és desfavorable. Aquesta transició és només possible amb l'assistència de fonons, degut a la llei de conservació del moment. La probabilitat d'interacció entre electrons i fotons, però, és molt reduïda.
Al principi de 1990, l'observació d'emissió en el rang del visible per nanocristalls de Si i per Si porós va obrir el camp d'estudi d'aquesta Tesi Doctoral, la nanociència del Si, en la forma de nanoestructures com ara nanofils, na-

nopartícules o punts quàntics [7].
Degut al confinement quàntic de les càrregues elèctriques dins del QD [8], el valor de l'energia de gap del material augmenta a mesura que la mida del QD disminueix, donant valors més gran que el Si bulk i fent que els Si QDs siguin uns bons candidats per a dispositius amb valors de l'energia de gap modificables. A més a més, seguint el principi d'incertesa de Heisenberg, degut a la localització dels estats electrònics dins de les nanoestructures, la distribució de moments deixa d'estar restringida, i per tant, el Si en la nanoescala esdevé un material de gap directe.
Diverses aplicacions s'han desenvolupat en els darrers anys que utilitzen aquestes noves propietats: des de dispositius d'emissió de llum [9] fins a cel·les solars de tipus tandem [10] o altres tipus de dispositius opto-electrònics [11].

Aquesta tesi doctoral s'ha desenvolupat en el marc del Projecte Europeu NASCEnT (silicon NAnodots for Solar CEll Tandem). El seu principal objectiu era crear una cel·la solar de tipus tandem formada per punts quàntics de silici (Si QDs en les seves sigles en anglès). Els Si QDs són candidats per crear la tercera generació de cel·les solars, amb les que es podrà superar el límit de Shockley-Queisser [12, 13], i.e. la màxima eficiència teòrica dels dispositius optoelectrònics, de les actuals cel·les solars individuals.

A més a més dels problemes tecnològics, com ara juncions, contactes, etc., la principal font que limita l'eficiència en una cel·la solar és que no tot l'espectre d'energia solar és absorbit i convertit en electricitat. Els principals mecanismes de pèrdua d'energia en cel·les solars individuals estan relacionats amb els fotons que tenen o una energia més petita o més gran que el valor del gap d'energia del material que compon la cel·la solar. Això és degut a què els primers no són absorbits pel material, mentre que els segons perden la diferència entre la seva energia i el valor de l'energia del gap en forma de calor. L'últim problema pot ser millorat a partir d'una cel·la solar de tipus tandem, on materials amb valors diferents de l'energia de gap són utilitzats, de forma que es poden reduir les pèrdues per termalització ja que hi ha més d'un valor d'energia de gap disponible per a absorbir fotons. El límit d'eficiència teòrica incrementa d'un 29% per una cel·la pn individual a un 42.5% per a una cel·la de tipus tandem. La configuració òptima per a la segona és un material amb una energia de gap entre 1.7-1.8 eV per a la cel·la de dalt a sobre d'una cel·la de Si monocristal·lí [14].
La tercera generació de cel·les solars està concentrant els esforços en trobar

solucions per les pèrdues d'energia abans esmentades amb materials que siguin abundants, no tòxics i que permetin una producció en massa. D'aquesta manera, el dispositiu proposat en el Projecte Europeu NASCEnT fou una cel·la solar tandem amb una cel·la de Si monocristal·lí com a base i una capa a sobre amb una distribució de Si QDs dins d'una matriu dielèctrica. Els principals avantatges dels Si QDs respecte altres candidats per a realitzar cel·les solars de tipus tandem, com ara III-V multijunció (són tòxics i costosos) o cel·les de la junció a-Si/μ-Si (restringides a només dues juncions i presenten degradació), són: la possibilitat de dos o més juncions, la no-toxicitat i abundància del Si i les matrius dielèctriques de Si (SiO_2, SiC, Si_xN_y), i la compatibilitat amb la tecnologia del Si tan àmpliament establerta.

C.1.1 Transport en nanoelectrònica

Des del 1985 fins a l'actualitat, la mida dels dispositius electrònics ha disminuït diversos ordres de magnitud, des de l'escala dels micrometres fins als nanometres. Així mateix, el tipus de transport predominant també ha canviat. Mentre el transport de difusió és el predominant en dispositius grans (camins aleatoris deguts a xocs entre electrons), en canals petits només apareix el transport balístic [15]. Per tant, els mètodes comuntment utilitzats per estudiar el transport electrònic en materials bulk, com ara l'equació de Boltzmann [16], poden no ser útils per nanodispositius. Per estudiar aquests darrers, es poden utilitzar diferents mètodes: Quantum Master Equations (en la nomenclatura en anglès) [18], formalisme del Hamiltonià de transferència (Transfer Hamiltonian, TH, en anglès) [19, 20] o el formalisme de funcions de Green de no-equilirbi (Non-Equilibrium Green Functions Formalism, NEGFF, en anglès) [15, 17, 21]. El primer i segon mètode es poden utilitzar per sistemes amb un acoplament dèbil entre els elèctrodes i la regió d'estudi, mentre que l'última és normalment utilitzada per sistemes fortament acoblats [21].

NEGFF o TH?

El NEGFF ha sigut utilitzat per estudiar diverses propietats de transport dels materials, com ara la conductància electrònica [22, 23] o les propietats termoelèctriques [21]. Normalment, s'utilitza el model Tight Binding (en la nomenclatura en anglès) [15], però la teoria del funcional de la densitat (Density Functional Theory, DFT, en anglès) és necessària per descriure d'u-

na forma acurada el transport electrònic quan les propietats atòmiques del material són importants [21]. A la Ref. [22] es descriu un extensiu mètode per simular dispositiu fotovoltaics quàntics mitjançant NEGFF. La potencialitat d'aquesta tècnica va ser una motivació per escollir treballar amb NEGFF a l'inici d'aquesta Tesi Doctoral.

Com que l'objectiu d'aquesta Tesi Doctoral és l'estudi del transport electrònic a través de QDs de Si dins de matrius dielèctriques des d'una aproximació *ab initio*, el marc de treball seleccionat va ser DFT-NEGFF. Per validar la conveniència d'aquests mètodes, un primer cas rellevant d'estudi, el Si bulk en diferents direccions cristal·logràfiques va ser satisfactòriament tractat mitjançant el mètode DFT-NEGFF. Així mateix, la tècnica ha sigut prèviament utilitzada per l'estudi de nanofils de Si [137]. Però, a l'hora d'abordar la modelització d'un QD de Si dins d'una matriu de SiO_2 conectada a dos elèctrodes semi-infinits d'alumini, vam trobar importants problemes de convergència, especialment relacionats amb l'acoblament entre la matriu de silica i els elèctrodes d'alumini. A més a més, aquest tipus de sistemes poden crèixer fàcilment fins a 700 àtoms, fent que el temps de càlcul pugui arribar a ser inassumible.
Per tal de superar aquesta dificultat, vam buscar una aproximació diferent: el formalisme del TH juntament amb acoblaments capacitius entre el QD i els elèctrodes permeten estudiar el corrent elèctric a través d'un nanodispositiu sense haver de descriure explícitament els àtoms dels elèctrodes, i focalitzant l'atenció només en les característiques DFT de la regió del dispositiu (Si QD + matriu dielèctrica).
El mètode del Hamiltonià de Transferència ha sigut utilitzat prèviament per modelitzar el corrent túnel de diferents tipus de configuracions, com ara l'espectroscopia d'escàner túnel (scanning tunnel spectroscopy en anglès) [19] o túnel ressonant en una doble barrera semiconductora [20, 31, 32].
És natural, doncs, proposar aquesta tècnica per estudiar el transport a través de QDs, ja que el potencial confinant d'aquestes nanoestructures es pot descriure com la darrera configuració. A més a més, Passoni et al. [19] va comparar els dos formalismes i va mostrar com el mètode del TH és més adient que NEGFF per aquest tipus de sistemes, donada la seva simplicitat.

Codis utilitzats per simular el transport electrònic en nanoestructures

El tractament *ab initio* dels sistemes s'ha fet mitjançant el conegut codi DFT SIESTA [101, 102], tant per la relaxació de les estructures com per el càlcul de les densitats d'estats utilitzades en els codis per modelar el transport electrònic.
Per una banda, el codi utilitzat per estudiar els sistemes sota el marc teòric DFT-NEGFF ha sigut TranSIESTA [26], una extensió de l'anterior codi.
Per l'altra banda, el programa utilitzat per computar el transport electrònic mitjançant TH, SIMQdot, va ser creat per Sergio Illera i codificat amb MATLAB©.
Les bases del codi es poden trobar en els següents articles: la definició dels mecanismes de transport entre QDs en sèrie i en paral·lel, amb amplituds de transferència constants i un nivell d'energia per QD [33], una comparació entre la metodologia proposada amb NEGFF i l'extensió del model a una matriu de múltiples punts quàntics [34], una explicació detallada del codi amb la capacitat d'utilitzar l'aproximació de WKB per descriure la transmissió túnel entre QDs i la capacitat d'utilitzar més d'un estat per QD, en particular la solució de l'equació d'Schrödinger per a una partícula dins d'un potencial esfèric dins l'aproximació de massa efectica (effective mass aproximation, EMA, en anglès) [35], i, finalment, com simular una cel·la solar, on el transport electrònic està lligat amb transicions òptiques degudes a la llum incident [36].

C.1.2 Treballs previs sobre punts quàntics de Si intrínsecs, el seu transport electrònic i el seu dopatge

Els QDs de Si dins d'una matriu de SiO_2 han sigut àmpliament estudiats teòricament en els darrers anys [47, 74–78, 185, 215].

En quant a l'estudi del seu transport electrònic, els treballs s'han centrat bàsicament en un sol o dos punts quàntics a través de NEGFF [37–40], amb només un nivell d'energia per QD i amplituds de transferència constants. El tractament de matrius de QD és encara un repte. Fins allà on arriba el nostre coneixement, les úniques computacions de transport electrònic en una matriu de QDs han sigut realitzades per: (1) Carreras et al. [41], que utilitza un model semi-empíric per el corrent túnel, (2) Han et al. [42] i (3)

Aeberhard et al. [43], que utilitzen un nivell d'energia per QD i NEGFF, i (4) Taranko et al. [44] que utilitza un nivell d'energia per QD i el mètode de l'equació de moviment (equation motion method en anglès).
Dins d'aquest context, la metodologia estudiada en aquesta Tesi Doctoral permet l'estudi del transport electrònic a través de múltiples QDs, amb coeficients de transmissió que modelitzen el transport túnel i amb una densitat d'estats del QD obtinguda a partir de primers principis.

Per una altra banda, el dopatge de semiconductors és essencial en dispositius optoelectrònics, sigui per modificar la conductivitat del material o com a forma de millorar els mecanismes de separació de les parelles electró-forat. S'han obtingut recentment QDs de Si p- i n-dopats dins d'una matriu de SiO_2 [3, 10, 53–56, 61, 62], mostrant que les impureses estan elèctricament activades i aconsegueixen millorar la conductivitat respecte les mostres no dopades. Fins allà on arriba el nostre coneixement, els estudis teòrics que s'han realitzat sobre dopatge de Si QDs s'han centrat en punts quàntics aïllats [57, 58, 63–68] (free-standing en anglès). Per tant, l'estudi realitzat en aquesta tesi obre les portes a la modelització *ab initio* de QDs de Si dopats embeguts dins de matrius dielèctriques.

C.2 Objectius d'aquesta Tesi Doctoral

Aquesta tesi va inicialitzar una col·laboració entre el nostre grup d'investigació i el grup liderat pel Prof. Ossicini de la Universitat de Modena i Reggio Emilia, que han estat estudiant i modelitzant punts quàntics de silici durant els darrers cinc anys [47, 74–79]. En aquest context, aquesta Tesi Doctoral vol aportar de la capacitat d'estudiar les propietats de transport d'aquest models a partir de l'ús conjunt de dues tècniques: DFT pel modelatge de la densitat d'estats del dispositiu i TH per la descripció del transport electrònic. En la present Tesi Doctoral ens hem centrat en l'estudi del transport electrònic a través d'un sol QD de Si dins d'una matriu de SiO_2. En particular, s'ha estudiat la influència de la mida del QD, el grau d'amorfització del sistema i el tipus i la posició de impureses sobre la corba característica corrent-voltatge *I-V*. És important remarcar que hom prodria extendre el procediment aquí descrit per estudiar el transport en una matriu de QDs, altres matrius dielèctriques, incloure la interacció amb la llum o amb fonons, dissenyar transistors, memristors, o termoeléctrics, etc. Aquesta tesi, doncs, dóna les les

primeres passes d'un procediment que sembla no tenir límits!

C.3 Estructura de la Dissertació

Aquesta Tesi Doctoral s'ha estructurat de la següent manera:

- A la Secció 2 s'expliquen breument les bases teòriques dels mètodes i codis utilitzats en aquest estudi.
- A continuació es presenten els resultats de la metodologia en tres seccions diferents. Primerament, la metodologia DFT-NEGFF va ser testejada a la Secció 3. En aquesta secció, es presenta un estudi termodinàmic de l'estabilitat de dos tipus de polimorfs de Si segons la mida de nanofils de Si, seguit de l'estudi de les propietats de transport electrònic d'aquests dos polimorfs de Si en bulk i descrits en les direccions cristal·logràfiques de creixement dels nanofils de Si. Aquest estudi ens va servir per veure que, malgrat DFT-NEGFF és interessant per sistemes que impliquen pocs àtoms, com ara materials bulk, superfícies, nanofils, o molècules, no és adequat a nivell computacional pels sistemes en que estàvem interessats en aquesta Tesi Doctoral, i.e. Si QDs dins d'una matriu de SiO_2.
- Seguidament, es presenta l'estudi del transport a través d'un QD de Si dins d'una matriu de SiO_2. En primer lloc, a la Secció 4, es presenta la metodologia DFT-TH proposada i es realitza un estudi profund dels paràmetres utilitzats en el codi SIMQdot. Finalment, s'explica la influència de la mida del QD i del grau de cristal·lització del sistem sobre el transport d'electrons i de forats.
- En segon lloc, a la Secció 5, es presenten les propietats extrínseques del Si QDs estudiats en la secció anterior. El dopatge tipus p s'ha realitzat introduint un àtom de B, mentre que el dopatge tipus n, a través d'un àtom de P. S'han estudiat diverses possibilitats en les posicions de la impuresa. En primer lloc es presenta l'energia de formació per tal de conéixer la situació de mínima energia, per tal de poder comparar amb experiments. Seguidament, les propietats estructurals i electròniques són estudiades amb DFT. I, per últim, es presenta el corrent d'electrons pels sistemes dopats tipus n i el corrent de forats pels sistemes dopats tipus p.

- Finalment, la Secció 6 recull les conclusions del treball amb una secció especial amb possibles idees per futurs estudis que podrien sorgir d'aquesta Tesi Doctoral.

C.4 Resultats i conclusions

C.4.1 Sobre la metodologia proposada

Com estàvem interessats en la descripció *ab initio* dels Si QDs, la mida dels sistemes estudiats queda limitada per les capacitats actuals de computació: QDs d'entre 1 i 1.7 nm de diàmetre dins d'una matriu de SiO_2 ja formen sistemes de centenars d'àtoms. Això fa que la comparació directa amb els experiments encara avui sigui una dificultat.

La principal raó per la qual TH és més adient que NEGFF pels nostres sistemes és que en el marc teòric de DFT-TH tan sols és necessari un càlcul DFT per tal d'obtenir la corba característica *I-V*. En comparació, la metodologia DFT-NEGFF requereix un càlcul DFT per a cadascun dels valors de voltatge de la corba *I-V*. En canvi, només cal un càlcul DFT en DFT-TH per descriure tot el sistema, al que no cal incloure els elèctrodes (a diferència de NEGFF on són explícitament descrits atomísticament).

El procediment proposat dins del marc teòric DFT-TH per computar una corba característica *I-V* per a un Si QD dins d'una matriu de SiO_2 és:

1. Relaxació de l'estructura amb DFT mitjançant el codi SIESTA.

2. Computació mitjançant DFT de la densitat d'estats projectada (PDOS en les seves sigles en anglès) en el subsistema format pels àtoms de Si del QD i la primera capa d'àtoms d'O que l'envolta.

3. Del càlcul DFT anterior, extracció del valor de les barreres de potencial del dielèctric, barrera per als electrons (forats), EB (HB) en les seves sigles en anglès.

4. Computació de la característica *I-V* mitjançant TH amb el codi SIMQ-dot, utilitzant la PDOS i els valors de les barreres extrets del càlcul DFT anterior.

C.4.2 Sobre la mida dels QDs

En el cas de QDs de Si de pocs nanometres dins de matrius dielèctriques, la interfície fortament no-planar entre el Si i el SiO_2 requereix un tractament diferent de la communtment utilitzada en l'heterojunció planar Si/SiO_2. En aquesta Tesi Doctoral hem observat que, per Si QDs de mida petita, el model de partícula-dins-d'una-caixa no descriu les densitats d'estats i les barrers de potencial d'una forma acurada. Això és degut a què aquest model no recull l'efecte de la interfície, propietat que sembla ser essencial en la mida nanomètrica.

Per tal de corregir la coneguda subestimació del valor de l'energia de gap del SiO_2 calculat amb DFT, hem aplicat una correcció constant en totes les barreres de potencial calculades en aquesta Tesi Doctoral, però no en els valors de l'energia de gap dels Si QDs. La correcció s'ha aplicat de forma que els valors de les barreres calculades amb DFT concordessin amb els valors experimentals per l'heterojunció planar Si/SiO_2. L'aproximació proposada es basa en resultat teòrics previs on es mostra que, (1) hi ha un decoplament entre els estats que pertanyen a la matriu de SiO_2 i els estats del subsistema format pel QD de Si i la primera capa d'àtoms d'O, i (2) les correccions del valor de l'energia de gap dels Si QD calculats amb DFT són negligibles.

Respecte el transport electrònic en QDs de Si, s'ha trobat una correlació entre EB (HB) i el corrent d'electrons (forats), obtenint un corrent més elevat per aquells sistemes amb unes barreres de potencial més petites. En particular, s'ha observat que els corrents d'electrons i forats tenen un comportament contrari respecte la mida dels punts quàntics i el nivell d'amorfització dels sistems. Per una banda, el corrent d'electrons (forats) és més gran per a Si QDs de mida més gran (petita), i, per l'altra banda, el corrent d'electrons (forats) és més important per a sistemes amorfs (cristal·lins).

C.4.3 Sobre l'efecte del dopatge

Finalment, la tècnica DFT-TH s'ha utilitzat per estudiar la influència d'impureses, B per dopatge tipus p i P per dopatge tipus n, en QDs de Si dins d'una matriu de SiO_2. Els principals efectes que s'han trobat són:

- Hi ha més distorsió morfològica quan es dopa amb B que amb P.

- Les configuracions de més baixa energia de formació són dins del QD quan dopem amb P (P-dot), i a la interfície entre el QD i la primera capa d'oxígens quan dopem amb B (B-int).

- A mesura que s'incrementa el confinament quàntic, i.e. per radis petits, hi ha més diferència de càrrega entre nivells amb spin-up i spin-down.

- El valor de l'energia del gap per als sistemes dopats disminueix a mesura que augmenta la mida del QD.

- Les relacions entre el desplaçament del nivell de Fermi del sistema dopat respecte l'intrínsec i la diferència en la càrrega Mulliken de la impuresa i l'àtom de Si substituït en el sistema no dopat: major desplaçament com més gran és la diferència de càrrega.

- Relació entre el desplaçament del nivell de Fermi i l'augment de la conductivitat en els sistemes dopats (degut al canvi en el valor de la barrera de potencial): més conductivitat com més gran és el desplaçament del nivell de Fermi, i per tant, més petita es fa la barrera de potencial.

- Hi ha un millora en la conductivitat per la posició energètica més favorable pel dopatge amb P (P-dot) però no per la posició pel dopatge amb B (B-int).

- El canvi de conductivitat dels sistemes dopats respecte els intrínsecs és més gran per a sistema dopats amb P que amb B; per a una mida de Si QD i una posició de la impuresa donats. Aquest canvi de conductivitat disminueix amb la mida del Si QD per a una espècie d'impuresa i una posició donades.

Bibliografia

[1] M. Segal. *Material history: Learning from silicon.* Nature, **483**, S43 (2012).

[2] H. J. Leamy and J. H. Wernick. *Semiconductor silicon: the extraordinary made ordinary.* MRS Bulletin, **22**, 47 (1997).

[3] X. Hao, E.-C. Cho, G. Scardera, Y. Shen, E. Bellet-Amalric, D. Bellet, G. Conibeer and M. Green. *Phosphorus-doped silicon quantum dots for all-silicon quantum dot tandem solar cells.* Sol. Energ. Mat. Sol. C, **93**, 1524 (2009).

[4] H. Takagi, H. Ogawa, Y. Yamazaki, A. Ishizaki and T. Nakagiri. *Quantum size effects on photoluminescence in ultrafine Si particles.* Appl. Phys. Lett., **56**, 2379 (1990).

[5] L. T. Canham. *Silicon quantum wire array fabrication by electrochemical and chemical dissolution of wafers.* Appl. Phys. Lett., **57**, 1046 (1990).

[6] P. D. J. Calcott, K. J. Nash, L. T. Canham, M. J. Kane and D. Brumhead. *Identification of radiative transitions in highly porous silicon.* J. Phys.: Condens. Matter, **5**, L91 (1993).

[7] O. Bisi, S. Ossicini and L. Pavesi. *Porous silicon: a quantum sponge structure for silicon based optoelectronics.* Surface Science Reports, **38**, 1 (2000).

[8] J. P. Proot, C. Delerue and G. Allan. *Electronic structure and optical properties of silicon crystallites: Application to porous silicon.* Appl. Phys. Lett., **61**, 1948 (1992).

[9] Y. Berencen, J. M. Ramirez, O. Jambois, C. Dominguez, J. A. Rodriguez and B. Garrido. *Correlation between charge transport and electroluminescence properties of Si-rich oxide/nitride/oxide-based light emitting capacitors.* J. Appl. Phys., **112**, 033114 (2012).

[10] G. Conibeer, I. Perez-Wurfl, X. Hao, D. Di and D. Lin. *Si solid-state quantum dot-based materials for tandem solar cells.* Nanoscale Res. Lett., **7**, 193 (2012).

[11] L. Pavesi, L. D. Negro, C. Mazzoleni, G. Franzo and F. Priolo. *Optical gain in silicon nanocrystals.* Nature, **408**, 440 (2000).

[12] W. Shockley and H. J. Queisser. *Detailed Balance Limit of Efficiency of p-n Junction Solar Cells.* J. Appl. Phys., **32**, 510 (1961).

[13] C. H. Henry. *Limiting efficiencies of ideal single and multiple energy gap terrestrial solar cells.* J. Appl. Phys., **51**, 4494 (1980).

[14] S. Park, E. Cho, D. Song, G. Conibeer and M. A. Green. *n-Type silicon quantum dots and p-type crystalline silicon heteroface solar cells.* Sol. Energ. Mat. Sol. C, **93**, 684 (2009). 17th International Photovoltaic Science and Engineering Conference.

[15] S. Datta. *Electronic Transport in Mesoscopic Systems.* Cambridge Studies in Semiconductor Physics and Microelectronic Engineering. Cambridge University Press (1997).

[16] T. T. Vo, A. J. Williamson, V. Lordi and G. Galli. *Atomistic Design of Thermoelectric Properties of Silicon Nanowires.* Nano Letters, **8**, 1111 (2008).

[17] H. Haug and A. Jauho. *Quantum Kinetics in Transport and Optics of Semiconductors.* Solid-State Sciences. Springer (2007).

[18] C. Timm. *Tunneling through molecules and quantum dots: Master-equation approaches.* Phys. Rev. B, **77**, 195416 (2008).

[19] M. Passoni and C. E. Bottani. *Transfer Hamiltonian analytical theory of scanning tunneling spectroscopy.* Phys. Rev. B, **76**, 115404 (2007).

[20] M. C. Payne. *Transfer Hamiltonian description of resonant tunnelling.* J. Phys. C: Solid State, **19**, 1145 (1986).

[21] B. K. Nikolić, K. K. Saha, T. Markussen and K. S. Thygesen. *First-principles quantum transport modeling of thermoelectricity in single-molecule nanojunctions with graphene nanoribbon electrodes*. J. Comput. Electron., 1–15 (2012).

[22] U. Aeberhard. *Theory and simulation of quantum photovoltaic devices based on the non-equilibrium Green's function formalism*. J. Comput. Electron., **10**, 394 (2011).

[23] M. Wang and C. M. Li. *Negative differential resistance in oxidized zigzag graphene nanoribbons*. Phys. Chem. Chem. Phys., **13**, 1413 (2011).

[24] D. A. Areshkin and B. K. Nikolić. *Electron density and transport in top-gated graphene nanoribbon devices: First-principles Green function algorithms for systems containing a large number of atoms*. Phys. Rev. B, **81**, 155450 (2010).

[25] J. Taylor, H. Guo and J. Wang. *Ab initio modeling of quantum transport properties of molecular electronic devices*. Phys. Rev. B, **63**, 245407 (2001).

[26] M. Brandbyge, J.-L. Mozos, P. Ordejón, J. Taylor and K. Stokbro. *Density-functional method for nonequilibrium electron transport*. Phys. Rev. B, **65**, 165401 (2002).

[27] K. Stokbro. *First-principles modeling of electron transport*. J. Phys.: Condens. Matter, **20**, 064216 (2008).

[28] K. K. Saha, W. Lu, J. Bernholc and V. Meunier. *First-principles methodology for quantum transport in multiterminal junctions*. J. Chem. Phys., **131**, 164105 (2009).

[29] K. K. Saha, B. K. Nikolić, V. Meunier, W. Lu and J. Bernholc. *Quantum-Interference-Controlled Three-Terminal Molecular Transistors Based on a Single Ring-Shaped Molecule Connected to Graphene Nanoribbon Electrodes*. Phys. Rev. Lett., **105**, 236803 (2010).

[30] T. Frederiksen, M. Brandbyge, N. Lorente and A.-P. Jauho. *Inelastic Scattering and Local Heating in Atomic Gold Wires*. Phys. Rev. Lett., **93**, 256601 (2004).

[31] L. L. Chang, L. Esaki and R. Tsu. *Resonant tunneling in semiconductor double barriers.* Appl. Phys. Lett., **24**, 593 (1974).

[32] B. Ricco and M. Y. Azbel. *Physics of resonant tunneling. The one-dimensional double-barrier case.* Phys. Rev. B, **29**, 1970 (1984).

[33] S. Illera, J. D. Prades, A. Cirera and A. Cornet. *Transport in quantum dot stacks using the transfer Hamiltonian method in self-consistent field regime.* Europhys. Lett., **98**, 17003 (2012).

[34] S. Illera, N. Garcia-Castello, J. D. Prades and A. Cirera. *A transfer Hamiltonian approach for an arbitrary quantum dot array in the self-consistent field regime.* J. Appl. Phys., **112**, 093701 (2012).

[35] S. Illera, J. D. Prades, A. Cirera and A. Cornet. *A Transfer Hamiltonian model for devices based in quantum dot arrays* (2012). ArXiv:1207.5513.

[36] S. Illera, J. D. Prades and A. Cirera. *A compact theoretical model for opto-electronic devices based on quantum dot arrays* (2013). ArXiv:1305.3612.

[37] S. D. Wang, Z. Z. Sun, N. Cue, H. Q. Xu and X. R. Wang. *Negative differential capacitance of quantum dots.* Phys. Rev. B, **65**, 125307 (2002).

[38] Z. Z. Sun, R. Q. Zhang, W. Fan and X. R. Wang. *Resonance and antiresonance effects in electronic transport through several-quantum-dot combinations.* J. Appl. Phys., **105**, 043706 (2009).

[39] A. L. Yeyati, A. Martin-Rodero and F. Flores. *Electron correlation resonances in the transport through a single quantum level.* Phys. Rev. Lett., **71**, 2991 (1993).

[40] Y. Meir, N. S. Wingreen and P. A. Lee. *Transport through a strongly interacting electron system: Theory of periodic conductance oscillations.* Phys. Rev. Lett., **66**, 3048 (1991).

[41] J. Carreras, O. Jambois, S. Lombardo and B. Garrido. *Quantum dot networks in dielectric media: from compact modeling of transport to the origin of field effect luminescence.* Nanotechnology, **20**, 155201 (2009).

[42] Y. Han, W. Gong, H. Wu and G. Wei. *Decoupling and antiresonance in electronic transport through a quantum dot chain embodied in an Aharonov–Bohm interferometer.* Physica B: Condensed Matter, **404**, 2001 (2009).

[43] U. Aeberhard. *Effective microscopic theory of quantum dot superlattice solar cells.* Opt. Quant. Electron., **44**, 133 (2012).

[44] E. Taranko, M. Wiertel and R. Taranko. *Transient electron transport properties of multiple quantum dots systems.* J. Appl. Phys., **111**, 023711 (2012).

[45] P. Löper, R. Müller, D. Hiller, T. Barthel, E. Malguth, S. Janz, J. C. Goldschmidt, M. Hermle and M. Zacharias. *Quasi-Fermi-level splitting in ideal silicon nanocrystal superlattices.* Phys. Rev. B, **84**, 195317 (2011).

[46] J. Bardeen. *Tunnelling from a Many-Particle Point of View.* Phys. Rev. Lett., **6**, 57 (1961).

[47] R. Guerra, E. Degoli and S. Ossicini. *Size, oxidation, and strain in small Si/SiO_2 nanocrystals.* Phys. Rev. B, **80**, 155332 (2009).

[48] D. J. DiMaria, D. W. Dong, C. Falcony, T. N. Theis, J. R. Kirtley, J. C. Tsang, D. R. Young, F. L. Pesavento and S. D. Brorson. *Charge transport and trapping phenomena in off-stoichiometric silicon dioxide films.* J. Appl. Phys., **54**, 5801 (1983).

[49] I. Balberg. *Electrical transport mechanisms in three dimensional ensembles of silicon quantum dots.* J. Appl. Phys., **110**, 061301 (2011).

[50] L. Rota, F. Rossi, S. M. Goodnick, P. Lugli, E. Molinari and W. Porod. *Reduced carrier cooling and thermalization in semiconductor quantum wires.* Phys. Rev. B, **47**, 1632 (1993).

[51] L. E. Henrickson, A. J. Glick, G. W. Bryant and D. F. Barbe. *Nonequilibrium-Green's-function theory of transport in interacting quantum dots.* Phys. Rev. B, **50**, 4482 (1994).

[52] D. J. Scalapino and S. M. Marcus. *Theory of Inelastic Electron-Molecule Interactions in Tunnel Junctions.* Phys. Rev. Lett., **18**, 459 (1967).

[53] D. Di, H. Xu, I. Perez-Wurfl, M. A. Green and G. Conibeer. *Improved nanocrystal formation, quantum confinement and carrier transport properties of doped Si quantum dot superlattices for third generation photovoltaics.* Prog. Photovolt. Res. Appl., **21**, 569 (2013).

[54] S. Huang and G. Conibeer. *Sputter-grown Si quantum dot nanostructures for tandem solar cells.* J. Phys. D: Appl. Phys., **46**, 024003 (2013).

[55] X. Hao, E.-C. Cho, C. Flynn, Y. Shen, S. Park, G. Conibeer and M. Green. *Synthesis and characterization of boron-doped Si quantum dots for all-Si quantum dot tandem solar cells.* Sol. Energ. Mat. Sol. C, **93**, 273 (2009).

[56] M. Xie, D. Li, L. Chen, F. Wang, X. Zhu and D. Yang. *The location and doping effect of boron in Si nanocrystals embedded silicon oxide film.* Appl. Phys. Lett., **102**, 123108 (2013).

[57] J. Ma, S.-H. Wei, N. R. Neale and A. J. Nozik. *Effect of surface passivation on dopant distribution in Si quantum dots: The case of B and P doping.* Appl. Phys. Lett., **98**, 173103 (2011).

[58] S. Ossicini, F. Iori, E. Degoli, E. Luppi, R. Magri, R. Poli, G. Cantele, F. Trani and D. Ninno. *Understanding Doping In Silicon Nanostructures.* IEEE J. Sel. Topics Quantum Electron., **12**, 1585 (2006).

[59] J. R. Chelikowsky, M. M. G. Alemany, T.-L. Chan and G. M. Dalpian. *Computational studies of doped nanostructures.* Rep. Prog. Phys., **74**, 046501 (2011).

[60] M. Perego, C. Bonafos and M. Fanciulli. *Phosphorus doping of ultrasmall silicon nanocrystals.* Nanotechnology, **21**, 025602 (2010).

[61] X. J. Hao, E.-C. Cho, C. Flynn, Y. S. Shen, G. Conibeer and M. A. Green. *Effects of boron doping on the structural and optical properties of silicon nanocrystals in a silicon dioxide matrix.* Nanotechnology, **19**, 424019 (2008).

[62] G. Conibeer, M. A. Green, D. König, I. Perez-Wurfl, S. Huang, X. Hao, D. Di, L. Shi, S. Shrestha, B. Puthen-Veetil, Y. So, B. Zhang and Z. Wan. *Silicon quantum dot based solar cells: addressing the issues*

of doping, voltage and current transport. Prog. Photovolt. Res. Appl., **19**, 813 (2011).

[63] D. V. Melnikov and J. R. Chelikowsky. *Quantum Confinement in Phosphorus-Doped Silicon Nanocrystals.* Phys. Rev. Lett., **92**, 046802 (2004).

[64] M. G. Mavros, D. A. Micha and D. S. Kilin. *Optical Properties of Doped Silicon Quantum Dots with Crystalline and Amorphous Structures.* J. Phys. Chem. C, **115**, 19529 (2011).

[65] J.-H. Eom, T.-L. Chan and J. R. Chelikowsky. *Vacancies and B doping in Si nanocrystals.* Solid State Commun., **150**, 130 (2010).

[66] Z. Zhou, M. L. Steigerwald, R. A. Friesner, L. Brus and M. S. Hybertsen. *Structural and chemical trends in doped silicon nanocrystals: First-principles calculations.* Phys. Rev. B, **71**, 245308 (2005).

[67] L. E. Ramos, E. Degoli, G. Cantele, S. Ossicini, D. Ninno, J. Furthmüller and F. Bechstedt. *Structural features and electronic properties of group-III-, group-IV-, and group-V-doped Si nanocrystallites.* J. Phys.: Condens. Matter, **19**, 466211 (2007).

[68] X. Chen, X. Pi and D. Yang. *Critical Role of Dopant Location for P-Doped Si Nanocrystals.* J. Phys. Chem. C, **115**, 661 (2011).

[69] V. A. Belyakov, V. A. Burdov, L. R. and M. A. *Silicon Nanocrystals: Fundamental Theory and Implications for Stimulated Emission.* Advances in Optical Technologies, **2008**, 279502 (2008).

[70] S. Gardelis, P. Manousiadis and A. G. Nassiopoulou. *Lateral electrical transport, optical properties and photocurrent measurements in two-dimensional arrays of silicon nanocrystals embedded in SiO_2.* Nanoscale Res. Lett., **6**, 227 (2011).

[71] C. Meier, A. Gondorf, S. Lüttjohann, A. Lorke and H. Wiggers. *Silicon nanoparticles: Absorption, emission, and the nature of the electronic bandgap.* J. Appl. Phys., **101**, 103112 (2007).

[72] Z. Lin, H. Li, A. Franceschetti and M. T. Lusk. *Efficient Exciton Transport between Strongly Quantum-Confined Silicon Quantum Dots.* ACS Nano, **6**, 4029 (2012).

[73] G. Conibeer, M. Green, E.-C. Cho, D. König, Y.-H. Cho, T. Fangsuwannarak, G. Scardera, E. Pink, Y. Huang, T. Puzzer, S. Huang, D. Song, C. Flynn, S. Park, X. Hao and D. Mansfield. *Silicon quantum dot nanostructures for tandem photovoltaic cells.* Thin Solid Films, **516**, 6748 (2008). Proceedings on Advanced Materials and Concepts for Photovoltaics (EMRS) 2007 Conference, Strasbourg, France.

[74] M. Luppi and S. Ossicini. *Ab initio study on oxidized silicon clusters and silicon nanocrystals embedded in* SiO_2*: Beyond the quantum confinement effect.* Phys. Rev. B, **71**, 035340 (2005).

[75] R. Guerra, I. Marri, R. Magri, L. Martin-Samos, O. Pulci, E. Degoli and S. Ossicini. *Silicon nanocrystallites in a* SiO_2 *matrix: Role of disorder and size.* Phys. Rev. B, **79**, 155320 (2009).

[76] R. Guerra and S. Ossicini. *High luminescence in small* Si/SiO_2 *nanocrystals: A theoretical study.* Phys. Rev. B, **81**, 245307 (2010).

[77] R. Guerra, E. Degoli, M. Marsili, O. Pulci and S. Ossicini. *Local-fields and disorder effects in free-standing and embedded Si nanocrystallites.* Phys. Status Solidi B, **247**, 2113 (2010).

[78] R. Guerra, M. Marsili, O. Pulci and S. Ossicini. *Local-field effects in silicon nanoclusters.* Phys. Rev. B, **84**, 075342 (2011).

[79] M. Govoni, I. Marri and S. Ossicini. *Auger recombination in Si and GaAs semiconductors: Ab initio results.* Phys. Rev. B, **84**, 075215 (2011).

[80] N. Garcia-Castello, J. D. Prades, R. Orlando and A. Cirera. *Stability Model of Silicon Nanowire Polymorphs and First-Principle Conductivity of Bulk Silicon.* J. Phys. Chem. C, **116**, 22078 (2012).

[81] N. Garcia-Castello, S. Illera, R. Guerra, J. D. Prades, S. Ossicini and A. Cirera. *Silicon quantum dots embedded in a* SiO_2 *matrix: From structural study to carrier transport properties.* Phys. Rev. B, **88**, 075322 (2013).

[82] N. Garcia-Castello, S. Illera, R. Guerra, J. D. Prades, S. Ossicini and A. Cirera. *Doping embedded silicon quantum dots: structural and electronic transport study.* In preparation to submit to Phys. Rev. B.

[83] J. P. Perdew and A. Zunger. *Self-interaction correction to density-functional approximations for many-electron systems.* Phys. Rev. B, **23**, 5048 (1981).

[84] D. Hartree. *The wave mechanics of an atom with a non-Coulomb central field. Part I. Theory adn methods.* Proc. Cambridge Phil. Soc., **24**, 89 (1928).

[85] V. Fock. Z. Phys., **61**, 126 (1930).

[86] J. Harris. *Adiabatic-connection approach to Kohn-Sham theory.* Phys. Rev. A, **29**, 1648 (1984).

[87] P. Hohenberg and W. Kohn. *Inhomogeneous Electron Gas.* Phys. Rev., **136**, B864 (1964).

[88] W. Kohn and L. J. Sham. *Self-Consistent Equations Including Exchange and Correlation Effects.* Phys. Rev., **140**, A1133 (1965).

[89] L. Thomas. *The calculation of atomic fields.* Proc. Cambridge Philos., **23**, 542 (1927).

[90] E. Fermi. Z. Phys., **48**, 73 (1928).

[91] J. P. Perdew, A. Ruzsinsky, J. Tao, V. N. Staroverov, G. E. Scuseria and G. I. Csonka. *Prescription for the design and selection of density functional approximations: More constraint satisfaction with fewer fits.* J. Chem. Phys., **123**, 062201 (2005).

[92] D. M. Ceperley and B. J. Alder. *Ground State of the Electron Gas by a Stochastic Method.* Phys. Rev. Lett., **45**, 566 (1980).

[93] J. P. Perdew and Y. Wang. *Accurate and simple analytic representation of the electron-gas correlation energy.* Phys. Rev. B, **45**, 13244 (1992).

[94] D. Ceperley. *Ground state of the fermion one-component plasma: A Monte Carlo study in two and three dimensions.* Phys. Rev. B, **18**, 3126 (1978).

[95] M. Gell-Mann and K. A. Brueckner. *Correlation Energy of an Electron Gas at High Density.* Phys. Rev., **106**, 364 (1957).

[96] W. J. Carr. *Energy, Specific Heat, and Magnetic Properties of the Low-Density Electron Gas*. Phys. Rev., **122**, 1437 (1961).

[97] J. P. Perdew, K. Burke and M. Ernzerhof. *Generalized Gradient Approximation Made Simple*. Phys. Rev. Lett., **77**, 3865 (1996).

[98] J. P. Perdew, A. Ruzsinszky, G. I. Csonka, O. A. Vydrov, G. E. Scuseria, L. A. Constantin, X. Zhou and K. Burke. *Restoring the Density-Gradient Expansion for Exchange in Solids and Surfaces*. Phys. Rev. Lett., **100**, 136406 (2008).

[99] R. Peverati and D. G. Truhlar. *An improved and broadly accurate local approximation to the exchange-correlation density functional: The MN12-L functional for electronic structure calculations in chemistry and physics*. Phys. Chem. Chem. Phys., **14**, 13171 (2012).

[100] A. D. Becke. *Density-functional thermochemistry. III. The role of exact exchange*. J. Chem. Phys., **98**, 5648 (1993).

[101] J. M. Soler, E. Artacho, J. D. Gale, A. García, J. Junquera, P. Ordejón and D. Sánchez-Portal. *The SIESTA method for ab initio order- N materials simulation*. J. Phys.: Condens. Matter, **14**, 2745 (2002).

[102] P. Ordejón, E. Artacho and J. M. Soler. *Self-consistent order-N density-functional calculations for very large systems*. Phys. Rev. B, **53**, R10441 (1996).

[103] C. Herring. *A New Method for Calculating Wave Functions in Crystals*. Phys. Rev., **57**, 1169 (1940).

[104] M. J. Frisch, G. W. Trucks, H. B. Schlegel, G. E. Scuseria, M. A. Robb, J. R. Cheeseman, G. Scalmani, V. Barone, B. Mennucci, G. A. Petersson, H. Nakatsuji, M. Caricato, X. Li, H. P. Hratchian, A. F. Izmaylov, J. Bloino, G. Zheng, J. L. Sonnenberg, M. Hada, M. Ehara, K. Toyota, R. Fukuda, J. Hasegawa, M. Ishida, T. Nakajima, Y. Honda, O. Kitao, H. Nakai, T. Vreven, J. A. Montgomery, Jr., J. E. Peralta, F. Ogliaro, M. Bearpark, J. J. Heyd, E. Brothers, K. N. Kudin, V. N. Staroverov, R. Kobayashi, J. Normand, K. Raghavachari, A. Rendell, J. C. Burant, S. S. Iyengar, J. Tomasi, M. Cossi, N. Rega, J. M. Millam, M. Klene, J. E. Knox, J. B. Cross, V. Bakken, C. Adamo, J. Jaramillo,

R. Gomperts, R. E. Stratmann, O. Yazyev, A. J. Austin, R. Cammi, C. Pomelli, J. W. Ochterski, R. L. Martin, K. Morokuma, V. G. Zakrzewski, G. A. Voth, P. Salvador, J. J. Dannenberg, S. Dapprich, A. D. Daniels, O. Farkas, J. B. Foresman, J. V. Ortiz, J. Cioslowski and D. J. Fox. *Gaussian 09 Revision D.01*. Gaussian Inc. Wallingford CT 2009.

[105] R. Dovesi, V. R. Saunders, C. Roetti, R. Orlando, C. M. Zicovich-Wilson, F. Pascale, B. Civalleri, K. Doll, N. M. Harrison, I. J. Bush, P-D'Arco, M. Llunell, M. Causànd Y. Noel. *CRYSTAL14 User's Manual*. University of Torino: Torino, 2014.

[106] R. van Leeuwen, N. Dahlen, G. Stefanucci, C.-O. Almbladh and U. von Barth. *Introduction to the Keldysh Formalism*. M. Marques, C. Ullrich, F. Nogueira, A. Rubio, K. Burke and E. U. Gross (editors), *Time-Dependent Density Functional Theory*, volume 706 of *Lecture Notes in Physics*, 33–59. Springer Berlin Heidelberg (2006).

[107] M. Büttiker, Y. Imry, R. Landauer and S. Pinhas. *Generalized many-channel conductance formula with application to small rings*. Phys. Rev. B, **31**, 6207 (1985).

[108] A. R. Williams, P. J. Feibelman and N. D. Lang. *Green's-function methods for electronic-structure calculations*. Phys. Rev. B, **26**, 5433 (1982).

[109] M. P. L. Sancho, J. M. L. Sancho and J. Rubio. *Quick iterative scheme for the calculation of transfer matrices: application to Mo (100)*. Journal of Physics F: Metal Physics, **14**, 1205 (1984).

[110] J. J. Sakurai. *Modern Quantum Mechanics (Revised Edition)*. Addison Wesley, 1 edition (1993).

[111] C. Wasshuber. *Computational Single-Electronics*. Computational Microelectronics. Springer (2001).

[112] R. Tsu and L. Esaki. *Tunneling in a finite superlattice*. Appl. Phys. Lett., **22**, 562 (1973).

[113] W.-C. Lee and C. Hu. *Modeling CMOS tunneling currents through ultrathin gate oxide due to conduction- and valence-band electron and hole tunneling*. IEEE Trans. Electron Devices, **48**, 1366 (2001).

[114] Y. Cui, Z. Zhong, D. Wang, W. U. Wang and C. M. Lieber. *High Performance Silicon Nanowire Field Effect Transistors*. Nano Letters, **3**, 149 (2003).

[115] G. Zheng, W. Lu, S. Jin and C. Lieber. *Synthesis and Fabrication of High-Performance n-Type Silicon Nanowire Transistors*. Adv. Mater., **16**, 1890 (2004).

[116] Y. Cui and C. M. Lieber. *Functional Nanoscale Electronic Devices Assembled Using Silicon Nanowire Building Blocks*. Science, **291**, 851 (2001).

[117] Y. Huang, X. Duan, Y. Cui, L. J. Lauhon, K.-H. Kim and C. M. Lieber. *Logic Gates and Computation from Assembled Nanowire Building Blocks*. Science, **294**, 1313 (2001).

[118] Y. Cui, Q. Wei, H. Park and C. M. Lieber. *Nanowire Nanosensors for Highly Sensitive and Selective Detection of Biological and Chemical Species*. Science, **293**, 1289 (2001).

[119] J.-I. Hahm and C. M. Lieber. *Direct Ultrasensitive Electrical Detection of DNA and DNA Sequence Variations Using Nanowire Nanosensors*. Nano Letters, **4**, 51 (2004).

[120] V. Schmidt, J. V. Wittemann and U. Gösele. *Growth, Thermodynamics, and Electrical Properties of Silicon Nanowires†*. Chem. Rev., **110**, 361 (2010).

[121] A. Fontcuberta i Morral, J. Arbiol, J. D. Prades, A. Cirera and J. R. Morante. *Synthesis of Silicon Nanowires with Wurtzite Crystalline Structure by Using Standard Chemical Vapor Deposition*. Adv. Mater., **19**, 1347 (2007).

[122] J. Arbiol, A. Fontcuberta i Morral, S. Estrade, F. Peiro, B. Kalache, P. R. i Cabarrocas and J. R. Morante. *Influence of the (111) twinning on the formation of diamond cubic/diamond hexagonal heterostructures in Cu-catalyzed Si nanowires*. J. Appl. Phys., **104**, 064312 (2008).

[123] J. Arbiol, B. Kalache, P. Roca i Cabarrocas, J. R. Morante and A. Fontcuberta i Morral. *Influence of Cu as a catalyst on the properties of silicon nanowires synthesized by the vapour–solid–solid mechanism*. Nanotechnology, **18**, 305606 (2007).

[124] F. J. Lopez, E. R. Hemesath and L. J. Lauhon. *Ordered Stacking Fault Arrays in Silicon Nanowires*. Nano Letters, **9**, 2774 (2009).

[125] M. Hendriks, S. Radelaar, A. Beers and J. Bloem. *Additional X-ray and electron diffraction peaks of polycrystalline silicon films*. Thin Solid Films, **113**, 59 (1984).

[126] C. Persson and E. Janzén. *Electronic band structure in hexagonal close-packed Si polytypes*. J. Phys.: Condens. Matter, **10**, 10549 (1998).

[127] D.-B. Zhang, M. Hua and T. Dumitrica. *Stability of polycrystalline and wurtzite Si nanowires via symmetry-adapted tight-binding objective molecular dynamics*. J. Chem. Phys., **128**, 084104 (2008).

[128] R. Kagimura, R. W. Nunes and H. Chacham. *Structures of Si and Ge Nanowires in the Subnanometer Range*. Phys. Rev. Lett., **95**, 115502 (2005).

[129] T.-L. Chan, C. V. Ciobanu, F.-C. Chuang, N. Lu, C.-Z. Wang and K.-M. Ho. *Magic Structures of H-Passivated* $\langle 110 \rangle$ *Silicon Nanowires*. Nano Letters, **6**, 277 (2006).

[130] P. Pirouz, R. Chaim, U. Dahmen and K. Westmacott. *The martensitic transformation in silicon—I experimental observations*. Acta Metallurgica et Materialia, **38**, 313 (1990).

[131] H. Cerva. *High-resolution electron microscopy of diamond hexagonal silicon in low pressure chemical vapor deposited polycrystalline silicon*. J. Mater. Res., **6**, 2324 (1991).

[132] Y. F. Zhang, L. S. Liao, W. H. Chan, S. T. Lee, R. Sammynaiken and T. K. Sham. *Electronic structure of silicon nanowires: A photoemission and x-ray absorption study*. Phys. Rev. B, **61**, 8298 (2000).

[133] R. Rurali and N. Lorente. *Metallic and Semimetallic Silicon* $\langle 100 \rangle$ *Nanowires*. Phys. Rev. Lett., **94**, 026805 (2005).

[134] T. Markussen, R. Rurali, M. Brandbyge and A.-P. Jauho. *Electronic transport through Si nanowires: Role of bulk and surface disorder*. Phys. Rev. B, **74**, 245313 (2006).

[135] M.-V. Fernández-Serra, C. Adessi and X. Blase. *Conductance, Surface Traps, and Passivation in Doped Silicon Nanowires.* Nano Letters, **6**, 2674 (2006).

[136] A. Svizhenko, P. W. Leu and K. Cho. *Effect of growth orientation and surface roughness on electron transport in silicon nanowires.* Phys. Rev. B, **75**, 125417 (2007).

[137] M.-F. Ng, L. Shen, L. Zhou, S.-W. Yang and V. B. C. Tan. *Geometry Dependent I-V Characteristics of Silicon Nanowires.* Nano Letters, **8**, 3662 (2008).

[138] S. Kyogoku, J.-I. Iwata and A. Oshiyama. *Relation between nanomorphology and energy bands of Si nanowires.* Phys. Rev. B, **87**, 165418 (2013).

[139] K. Kobayashi. *Surface-state conduction of medium-sized nanowires.* Phys. Rev. B, **69**, 115338 (2004).

[140] Y. Zheng, C. Rivas, R. Lake, K. Alam, T. Boykin and G. Klimeck. *Electronic properties of silicon nanowires.* IEEE Trans. Electron Devices, **52**, 1097 (2005).

[141] I. Ponomareva, M. Menon, E. Richter and A. N. Andriotis. *Structural stability, electronic properties, and quantum conductivity of small-diameter silicon nanowires.* Phys. Rev. B, **74**, 125311 (2006).

[142] M. P. Persson, A. Lherbier, Y.-M. Niquet, F. Triozon and S. Roche. *Orientational Dependence of Charge Transport in Disordered Silicon Nanowires.* Nano Letters, **8**, 4146 (2008).

[143] V. S. Sundaram and A. Mizel. *Surface effects on nanowire transport: a numerical investigation using the Boltzmann equation.* J. Phys.: Condens. Matter, **16**, 4697 (2004).

[144] F. Cargnoni and C. Gatti. *Direct-space analysis of the Si-Si bonding pattern in the π-bonded chain reconstructed Si(111)(2x1) surface.* Theor. Chem. Acc., **105**, 309 (2001).

[145] J. P. Perdew, J. A. Chevary, S. H. Vosko, K. A. Jackson, M. R. Pederson, D. J. Singh and C. Fiolhais. *Atoms, molecules, solids, and*

surfaces: Applications of the generalized gradient approximation for exchange and correlation. Phys. Rev. B, **46**, 6671 (1992).

[146] A. D. Becke. *Density-functional thermochemistry. I. The effect of the exchange-only gradient correction*. J. Chem. Phys., **96**, 2155 (1992).

[147] E. I. Proynov, E. Ruiz, A. Vela and D. R. Salahub. *Determining and extending the domain of exchange and correlation functionals*. Int. J. Quantum Chem, **56**, 61 (1995).

[148] B. Hammer, K. W. Jacobsen and J. K. Nørskov. *Role of nonlocal exchange correlation in activated adsorption*. Phys. Rev. Lett., **70**, 3971 (1993).

[149] D. R. Hamann. *Generalized Gradient Theory for Silica Phase Transitions*. Phys. Rev. Lett., **76**, 660 (1996).

[150] J. D. Prades, J. Arbiol, A. Cirera, J. R. Morante and A. F. i Morral. *Concerning the 506 cm^{-1} band in the Raman spectrum of silicon nanowires*. Appl. Phys. Lett., **91**, 123107 (2007).

[151] A. S. Barnard and L. A. Curtiss. *A Model for the Phase Stability of Arbitrary Nanoparticles as a Function of Size and Shape*. Rev. Adv. Mater. Sci., **10**, 105 (2005).

[152] A. S. Barnard and P. Zapol. *A model for the phase stability of arbitrary nanoparticles as a function of size and shape*. J. Chem. Phys., **121**, 4276 (2004).

[153] F. H.-R. et al. *Metal Oxide Nanostructures and Their Applications*, chapter 1. Fabrication of Nanodevices Based on Individual SnO_2 Nanowires and Their Electrical Characterization. Americal Scientific Publishers (2009).

[154] J. D. Holmes, K. P. Johnston, R. C. Doty and B. A. Korgel. *Control of Thickness and Orientation of Solution-Grown Silicon Nanowires*. Science, **287**, 1471 (2000).

[155] D. D. D. Ma, C. S. Lee, F. C. K. Au, S. Y. Tong and S. T. Lee. *Small-Diameter Silicon Nanowire Surfaces*. Science, **299**, 1874 (2003).

[156] Y. Wu, Y. Cui, L. Huynh, C. J. Barrelet, D. C. Bell and C. M. Lieber. *Controlled Growth and Structures of Molecular-Scale Silicon Nanowires.* Nano Letters, **4**, 433 (2004).

[157] V. Schmidt, S. Senz and U. Gösele. *Diameter-Dependent Growth Direction of Epitaxial Silicon Nanowires.* Nano Letters, **5**, 931 (2005).

[158] A. M. Morales and C. M. Lieber. *A Laser Ablation Method for the Synthesis of Crystalline Semiconductor Nanowires.* Science, **279**, 208 (1998).

[159] M. Topsakal, V. M. K. Bagci and S. Ciraci. *Current-voltage (I-V) characteristics of armchair graphene nanoribbons under uniaxial strain.* Phys. Rev. B, **81**, 205437 (2010).

[160] M. Murayama and T. Nakayama. *Chemical trend of band offsets at wurtzite/zinc-blende heterocrystalline semiconductor interfaces.* Phys. Rev. B, **49**, 4710 (1994).

[161] J. Gordon and R. Serway. *Principles of Physics.* Number v. 2 in Study Guide, Student Solutions Manual to Accompany Principles of Physics, Second Edition, Serway. Saunders College Pub. (1998).

[162] J. Bauer, F. Fleischer, O. Breitenstein, L. Schubert, P. Werner, U. Gosele and M. Zacharias. *Electrical properties of nominally undoped silicon nanowires grown by molecular-beam epitaxy.* Appl. Phys. Lett., **90**, 012105 (2007).

[163] J. Arbiol, S. Estradé, J. D. Prades, A. Cirera, F. Furtmayr, C. Stark, A. Laufer, M. Stutzmann, M. Eickhoff, M. H. Gass, A. L. Bleloch, F. Peiró and J. R. Morante. *Triple-twin domains in Mg doped GaN wurtzite nanowires: structural and electronic properties of this zinc-blende-like stacking.* Nanotechnology, **20**, 145704 (2009).

[164] P. R. Bandaru and P. Pichanusakorn. *An outline of the synthesis and properties of silicon nanowires.* Semicond. Sci. Tech., **25**, 024003 (2010).

[165] F. A. Reboredo, L. Pizzagalli and G. Galli. *Computational Engineering of the Stability and Optical Gaps of SiC Quantum Dots.* Nano Letters, **4**, 801 (2004).

[166] M. Vörös, P. Deák, T. Frauenheim and A. Gali. *The absorption spectrum of hydrogenated silicon carbide nanocrystals from ab initio calculations.* Appl. Phys. Lett., **96**, 051909 (2010).

[167] H.-C. Weissker, J. Furthmüller and F. Bechstedt. *Optical properties of Ge and Si nanocrystallites from ab initio calculations. I. Embedded nanocrystallites.* Phys. Rev. B, **65**, 155327 (2002).

[168] R. Guerra, M. Ippolito, S. Meloni and S. Ossicini. *The influence of silicon nanoclusters on the optical properties of a-SiNx samples: A theoretical study.* Appl. Phys. Lett., **100**, 181905 (2012).

[169] P. D. Nguyen, D. M. Kepaptsoglou, Q. M. Ramasse and A. Olsen. *Direct observation of quantum confinement of Si nanocrystals in Si-rich nitrides.* Phys. Rev. B, **85**, 085315 (2012).

[170] J. Fan, X. Wu and P. K. Chu. *Low-dimensional SiC nanostructures: Fabrication, luminescence, and electrical properties.* Progress in Materials Science, **51**, 983 (2006).

[171] N.-M. Park, T.-S. Kim and S.-J. Park. *Band gap engineering of amorphous silicon quantum dots for light-emitting diodes.* Appl. Phys. Lett., **78**, 2575 (2001).

[172] B. Zaknoon, G. Bahir, C. Saguy, R. Edrei, A. Hoffman, R. A. Rao, R. Muralidhar and K.-M. Chang. *Study of Single Silicon Quantum Dots Band Gap and Single-Electron Charging Energies by Room Temperature Scanning Tunneling Microscopy.* Nano Letters, **8**, 1689 (2008).

[173] N. Troullier and J. L. Martins. *Efficient pseudopotentials for plane-wave calculations. II. Operators for fast iterative diagonalization.* Phys. Rev. B, **43**, 8861 (1991).

[174] J. Halbritter, G. Repphun, S. Vinzelberg, G. Staikov and W. Lorenz. *Tunneling mechanisms in electrochemical STM - a distance and voltage tunneling spectroscopy.* Electrochimica Acta, **40**, 1385 (1995). 6th International Fischer Symposium on Nanotechniques in Electeochemistry.

[175] N. Daldosso, M. Luppi, S. Ossicini, E. Degoli, R. Magri, G. Dalba, P. Fornasini, R. Grisenti, F. Rocca, L. Pavesi, S. Boninelli, F. Priolo,

C. Spinella and F. Iacona. *Role of the interface region on the optoelectronic properties of silicon nanocrystals embedded in SiO_2.* Phys. Rev. B, **68**, 085327 (2003).

[176] L. Martin-Samos, Y. Limoge, J.-P. Crocombette, G. Roma, N. Richard, E. Anglada and E. Artacho. *Neutral self-defects in a silica model: A first-principles study.* Phys. Rev. B, **71**, 014116 (2005).

[177] K. Kůsová, L. Ondič, E. Klimešová, K. Herynková, I. Pelant, S. Daniš, J. Valenta, M. Gallart, M. Ziegler, B. Hönerlage and P. Gilliot. *Luminescence of free-standing versus matrix-embedded oxide-passivated silicon nanocrystals: The role of matrix-induced strain.* Appl. Phys. Lett., **101**, 143101 (2012).

[178] T. Li, F. Gygi and G. Galli. *Tailored Nanoheterojunctions for Optimized Light Emission.* Phys. Rev. Lett., **107**, 206805 (2011).

[179] R. Del Sole, L. Reining and R. W. Godby. *$GW\,\Gamma$ approximation for electron self-energies in semiconductors and insulators.* Phys. Rev. B, **49**, 8024 (1994).

[180] E. K. Chang, M. Rohlfing and S. G. Louie. *Excitons and Optical Properties of α-Quartz.* Phys. Rev. Lett., **85**, 2613 (2000).

[181] R. W. Godby, M. Schlüter and L. J. Sham. *Self-energy operators and exchange-correlation potentials in semiconductors.* Phys. Rev. B, **37**, 10159 (1988).

[182] C. Delerue, M. Lannoo and G. Allan. *Excitonic and Quasiparticle Gaps in Si Nanocrystals.* Phys. Rev. Lett., **84**, 2457 (2000).

[183] F. Fuchs, J. Furthmüller, F. Bechstedt, M. Shishkin and G. Kresse. *Quasiparticle band structure based on a generalized Kohn-Sham scheme.* Phys. Rev. B, **76**, 115109 (2007).

[184] S. Miyazaki, H. Nishimura, M. Fukuda, L. Ley and J. Ristein. *Structure and electronic states of ultrathin SiO2 thermally grown on Si(100) and Si(111) surfaces.* Applied Surface Science, **113–114**, 585 (1997). Proceedings of the Eighth International Conference on Solid Films and Surfaces.

[185] K. Seino, F. Bechstedt and P. Kroll. *Influence of SiO_2 matrix on electronic and optical properties of Si nanocrystals.* Nanotechnology, **20**, 135702 (2009).

[186] G. Conibeer, M. Green, R. Corkish, Y. Cho, E.-C. Cho, C.-W. Jiang, T. Fangsuwannarak, E. Pink, Y. Huang, T. Puzzer, T. Trupke, B. Richards, A. Shalav and K. lung Lin. *Silicon nanostructures for third generation photovoltaic solar cells.* Thin Solid Films, **511–512**, 654 (2006).

[187] R. Guerra, F. Cigarini and S. Ossicini. *Optical absorption and emission of silicon nanocrystals: From single to collective response.* J. Appl. Phys., **113**, 143505 (2013).

[188] Z. Zhou, L. Brus and R. Friesner. *Electronic Structure and Luminescence of 1.1- and 1.4-nm Silicon Nanocrystals: Oxide Shell versus Hydrogen Passivation.* Nano Letters, **3**, 163 (2003).

[189] G. Seguini, C. Castro, S. Schamm-Chardon, G. BenAssayag, P. Pellegrino and M. Perego. *Scaling size of the interplay between quantum confinement and surface related effects in nanostructured silicon.* Appl. Phys. Lett., **103**, 023103 (2013).

[190] C. Flynn, D. König, I. Perez-Wurfl, M. A. Green and G. Conibeer. *Correlation between fixed charge and capacitance peaks in silicon nanocrystal metal–insulator–semiconductor devices.* Semicond. Sci. Tech., **25**, 045011 (2010).

[191] C.-W. Jiang and M. A. Green. *Silicon quantum dot superlattices: Modeling of energy bands, densities of states, and mobilities for silicon tandem solar cell applications.* J. Appl. Phys., **99**, 114902 (2006).

[192] K. Seino, F. Bechstedt and P. Kroll. *Band alignment at a nonplanar Si/SiO_2 interface.* Phys. Rev. B, **82**, 085320 (2010).

[193] M. V. Wolkin, J. Jorne, P. M. Fauchet, G. Allan and C. Delerue. *Electronic States and Luminescence in Porous Silicon Quantum Dots: The Role of Oxygen.* Phys. Rev. Lett., **82**, 197 (1999).

[194] A. Zimina, S. Eisebitt, W. Eberhardt, J. Heitmann and M. Zacharias. *Electronic structure and chemical environment of silicon nanoclusters*

embedded in a silicon dioxide matrix. Appl. Phys. Lett., **88**, 163103 (2006).

[195] G. Seguini, S. Schamm-Chardon, P. Pellegrino and M. Perego. *The energy band alignment of Si nanocrystals in SiO2*. Appl. Phys. Lett., **99**, 082107 (2011).

[196] J. Zeng and H. Yu. *A First-principle Study of B- and P-doped Silicon Quantum Dots*. J. Nanomaterials, **2012**, 1:1 (2012).

[197] S. Ossicini, E. Degoli, F. Iori, E. Luppi, R. Magri, G. Cantele, F. Trani and D. Ninno. *Simultaneously B- and P-doped silicon nanoclusters: Formation energies and electronic properties*. Appl. Phys. Lett., **87**, 173120 (2005).

[198] X. Pi. *Doping Silicon Nanocrystals with Boron and Phosphorus*. J. Nanomaterials, **2012**, 3:3 (2012).

[199] O. Sinai and L. Kronik. *Simulated doping of Si from first principles using pseudoatoms*. Phys. Rev. B, **87**, 235305 (2013).

[200] X. Luo, S. B. Zhang and S.-H. Wei. *Understanding Ultrahigh Doping: The Case of Boron in Silicon*. Phys. Rev. Lett., **90**, 026103 (2003).

[201] L. G. Wang and A. Zunger. *Phosphorus and sulphur doping of diamond*. Phys. Rev. B, **66**, 161202 (2002).

[202] X. D. Pi, R. Gresback, R. W. Liptak, S. A. Campbell and U. Kortshagen. *Doping efficiency, dopant location, and oxidation of Si nanocrystals*. Appl. Phys. Lett., **92**, 123102 (2008).

[203] A. R. Stegner, R. N. Pereira, R. Lechner, K. Klein, H. Wiggers, M. Stutzmann and M. S. Brandt. *Doping efficiency in freestanding silicon nanocrystals from the gas phase: Phosphorus incorporation and defect-induced compensation*. Phys. Rev. B, **80**, 165326 (2009).

[204] A. Carvalho, S. Oberg, M. Barroso, M. J. Rayson and P. R. Briddon. *Doping of Si nanoparticles: the effect of oxidation* (2012). ArXiv:1207.0770.

[205] A. Carvalho, S. Öberg, M. Barroso, M. J. Rayson and P. Briddon. *P-doping of Si nanoparticles: The effect of oxidation.* Phys. Status Solidi A, **209**, 1847 (2012).

[206] H. Sugimoto, M. Fujii, M. Fukuda, K. Imakita and S. Hayashi. *Acceptor-related low-energy photoluminescence from boron-doped Si nanocrystals.* J. Appl. Phys., **110**, 063528 (2011).

[207] B. J. Simonds, I. Perez-Würfl, Y.-H. So, A. S. Wan, S. McMurray and P. C. Taylor. *Phosphorous doping of superlattice silicon quantum dots in silicon dioxide.* Phys. Status Solidi C, **9**, 1908 (2012).

[208] E.-C. Cho, S. Park, X. Hao, D. Song, G. Conibeer, S.-C. Park and M. A. Green. *Silicon quantum dot/crystalline silicon solar cells.* Nanotechnology, **19**, 245201 (2008).

[209] S. Gutsch, A. M. Hartel, D. Hiller, N. Zakharov, P. Werner and M. Zacharias. *Doping efficiency of phosphorus doped silicon nanocrystals embedded in a SiO_2 matrix.* Appl. Phys. Lett., **100**, 233115 (2012).

[210] M. Fukuda, M. Fujii, H. Sugimoto, K. Imakita and S. Hayashi. *Surfactant-free solution-dispersible Si nanocrystals surface modification by impurity control.* Opt. Lett., **36**, 4026 (2011).

[211] H. Sugimoto, M. Fujii, K. Imakita, S. Hayashi and K. Akamatsu. *All-Inorganic Near-Infrared Luminescent Colloidal Silicon Nanocrystals: High Dispersibility in Polar Liquid by Phosphorus and Boron Codoping.* J. Phys. Chem. C, **116**, 17969 (2012).

[212] N. Uchida, T. Okami, H. Tagami, N. Fukata, M. Mitome, Y. Bando and K. Murakami. *Synthesis of silicon nanocrystals in aluminum-doped SiO_2 film by laser ablation method.* Physica E: Low-dimensional Systems and Nanostructures, **38**, 31 (2007). Proceedings of the E-MRS 2006 Symposium C: Silicon Nanocrystals for Electronic and Sensing Applications.

[213] D. Tetelbaum, O. Gorshkov, V. Burdov, S. Trushin, A. Mikhaylov, D. Gaponova, S. Morozov and A. Kovalev. *The influence of P+, B+, and N+ ion implantation on the luminescence properties of the SiO_2: nc-Si system.* Physics of the Solid State, **46**, 17 (2004).

[214] A. Mikhaylov, D. Tetelbaum, V. Burdov, O. Gorshkov, A. Belov, D. Kambarov, V. Belyakov, V. Vasiliev, A. Kovalev and D. Gaponova. *Effect of ion doping with donor and acceptor impurities on intensity and lifetime of photoluminescence from SiO_2 films with silicon quantum dots*. Journal of Nanoscience and Nanotechnology, **8**, 780 (2008).

[215] K. Seino, F. Bechstedt and P. Kroll. *Tunneling of electrons between Si nanocrystals embedded in a SiO_2 matrix*. Phys. Rev. B, **86**, 075312 (2012).